

2020-01-21

Investigation of the Redox Performances of Manganite-based Perovskites for Isothermal CO₂ Conversion Applications

Shrestha, Pradeep

Shrestha, P. (2020). Investigation of the Redox Performances of Manganite-based Perovskites for Isothermal CO₂ Conversion Applications (Master's thesis, University of Calgary, Calgary, Canada). Retrieved from <https://prism.ucalgary.ca>.

<http://hdl.handle.net/1880/111544>

Downloaded from PRISM Repository, University of Calgary

UNIVERSITY OF CALGARY

Investigation of the Redox Performances of Manganite-based Perovskites for Isothermal
CO₂ Conversion Applications

by

Pradeep Shrestha

A THESIS

SUBMITTED TO THE FACULTY OF GRADUATE STUDIES
IN PARTIAL FULFILMENT OF THE REQUIREMENTS FOR THE
DEGREE OF MASTER OF SCIENCE

GRADUATE PROGRAM IN CHEMICAL ENGINEERING

CALGARY, ALBERTA

JANUARY, 2020

© Pradeep Shrestha 2020

Abstract

The growing energy demand and heavy dependence on fossil fuels only aggravates the situation caused by global warming and climate change. Converting key Greenhouse Gases (GHGs) such as CO₂ into valuable fuels and chemicals can tackle both the problem of climate change and global energy demand. Thermochemical splitting of CO₂ into CO utilizing the redox cycles of manganite-based perovskites have been previously investigated. However, most of these studies have reduced the manganite-based perovskites using only thermal energy at elevated temperatures of 1400 °C and then re-oxidized it at 1050 °C. This study focuses on carrying out thermochemical splitting of CO₂ into CO using the redox cycles of manganite-based perovskites in a Thermogravimetric Analyzer (TGA) at isothermal conditions. Moreover, CH₄ was used as a reducing agent to reduce the perovskites at lower temperatures (≤ 900 °C). In particular, the effect of A and B –site substitution on the redox performances of the manganite-based perovskites were studied. Initially amongst the samples CaMnO₃, La_{0.5}Ca_{0.5}MnO₃, La_{0.5}Sr_{0.5}MnO₃ and Y_{0.5}Sr_{0.5}MnO₃ with varying A –site composition, La_{0.5}Sr_{0.5}MnO₃ was identified of having the best performance in terms of both activity and stability. Further investigation of the La_{1-x}Sr_xMnO₃ perovskite family with x = 0.5, 0.25 and 0.10, revealed that La_{0.5}Sr_{0.5}MnO₃ is the optimal composition. Moreover, the activation energy for reduction was found to decrease with increasing Sr content. Substituting the B –site of the La_{1-x}Sr_xMnO₃ perovskite with Al and Fe did not improve the performance of the material. Besides, 10 redox cycling tests for the perovskite samples showed stable O₂ and CO production. The size variance and the metal-oxygen bond strength provide the best explanations for the trends observed in this study.

Acknowledgements

First of all, I would like to express my sincere gratitude to my supervisor, Dr. Nader Mahinpey for his continuous support, guidance and encouragement throughout my term as an MSc student at the University of Calgary.

I would also like to thank my supervisory committee members and examiners Dr. Hua Song and Dr. Md Kibria, for their time and effort for providing invaluable comments and feedback on this thesis. I would like to acknowledge the financial support from NSERC-IRC Program, Canadian Natural Resources Limited (CNRL) and Devon Canada Corporation. I greatly appreciate the support from the partners CNRL, Devon, PTAC and CanmetENERGY.

I am grateful to all the staffs in the Department of Chemical and Petroleum Engineering as well as in Schulich School of Engineering at the University of Calgary for their support.

I genuinely thank all the members of the Energy and Environment Research Group (EERG) for creating a friendly and positive environment every day. In particular, I would like to acknowledge Dr. Mahesh Nair for his important guidance and support in regards to both the experimental and analytical part of the thesis. I am thankful to Dr. Davood Karami, Dr. Mansour Tijani, Camilla Fernandes de Oliveira and Ningyu Yu (Bruce) for their continuous support throughout my graduate term.

Lastly, I wholeheartedly thank my parents, Shyam Kumari Shrestha and Purushottam Shrestha, and my sister, Srijana Shrestha Pradhan for their unwavering love, support, patience and motivation.

Dedication

*This thesis is dedicated to my parents, Shyam Kumari Shrestha and Purushottam
Shrestha, for their unconditional love.*

Table of Contents

Abstract.....	ii
Acknowledgements.....	iii
Dedication.....	iv
Table of Contents.....	v
List of Tables.....	vii
List of Figures.....	viii
List of Symbols, Abbreviation and Nomenclature.....	xii
CHAPTER ONE: INTRODUCTION.....	1
1.1. Problem Statement and Objectives.....	1
1.2. Methodology.....	6
1.3. Thesis Overview.....	7
1.4. Statement of Contributions.....	8
CHAPTER TWO: LITERATURE REVIEW.....	9
2.1. Global Warming and Climate Change.....	9
2.2. Energy Demand.....	13
2.3. CO ₂ Conversion.....	15
2.3.1. Background, Challenges and Opportunities.....	15
2.3.2. Different Pathways for CO ₂ Conversion.....	17
2.4. Perovskites.....	21
2.4.1. History and Background.....	21
2.4.2. Properties.....	22
2.4.3. Applications.....	25
2.4.4. Manganite-Based Perovskites.....	26
CHAPTER THREE: EXPERIMENTS AND DISCUSSION.....	29
3.1. Experiments.....	29
3.1.1. Synthesis.....	29
3.1.2. Characterization.....	31
3.2. Results and Discussion.....	36
3.2.1. A-site Substitution and Effect of temperature.....	36
3.2.2. Optimal A-site Composition.....	44

3.2.3. B-site Substitution	62
3.2.4. Comparison between thermal reduction and reduction using methane	75
3.2.5. Long-term Stability Tests	86
CHAPTER FOUR: FACTORS AFFECTING REDUCTION EXTENT AND OXYGEN NON-STOICHIOMETRY	90
4.1. Goldschmidt Tolerance Factor	91
4.2. Size Variance.....	99
4.3. Electronegativity Difference Between Oxygen and A and B -site Cations	105
4.4. Metal-Oxygen Bond Strength	109
CHAPTER FIVE: CONCLUSION AND RECOMMENDATIONS	118
5.1. Conclusion.....	118
5.2. Recommendations	122
REFERENCES	123
APPENDICES	133

List of Tables

Table 1. Textural properties of fresh LSM, fresh LSM7525 and fresh LSM9010.	47
Table 2. O ₂ evolution during the reduction phase of the first redox cycle under different reduction conditions.....	76
Table 3. Activation energy of LSM9010 during thermal and CH ₄ reduction.....	85

List of Figures

Figure 1. Change in global surface temperature relative to 1951-1980 average temperatures [10].	10
Figure 2. Change in sea level from 1870 to 2013 [11].	10
Figure 3. CO ₂ level in the atmosphere from 400,000 years ago to the present time [8]...	11
Figure 4. Global primary sources of energy in 2016. Based on IEA data from the IEA (2018) World Energy Balances, www.iea.org/statistics . All rights reserved; as modified by Pradeep Shrestha.	13
Figure 5. Ideal cubic perovskite structure of SrTiO ₃ [55].	21
Figure 6. Tilting of the FeO ₆ octahedra in the case of GdFeO ₃ perovskite [55].	23
Figure 7. Redox cycle of perovskite ABO ₃ [68].	26
Figure 8. Step-by-step procedure for synthesizing perovskite structured metal oxides using Pechini method [74].	29
Figure 9. Reaction Schematic of Pechini Method [75].	30
Figure 10. Rigaku Multiflex System Used for XRD Analysis of the Perovskites Samples Synthesized	31
Figure 11. Micromeritics ASAP 2020 Surface Area and Porosity Analyzer.	33
Figure 12. NETZSCH (TG 209 F1 Libra) TGA Used to Evaluate the CO ₂ Conversion Performance.	35
Figure 13. XRD pattern for the various samples synthesized.	36
Figure 14. Three redox cycle performances of CM, LCM and LSM at 700 °C	38
Figure 15. Three cycle redox performance of CM, LCM, LSM and YSM at 800 °C	38
Figure 16. Three cycle redox performance of CM, LCM, LSM and YSM at 900 °C	39
Figure 17. Reduction extent as a function of temperature for CM, LCM and LSM	40
Figure 18. O ₂ and CO production during the first redox cycle at 900 °C for CM, LCM, LSM and YSM.	41
Figure 19. Reduction extent as a function of size variance.	42
Figure 20. XRD profiles of YSM and LSM before and after three redox cycles at 900 °C.	42
Figure 21. XRD profile of fresh YSM and YSM after 3 redox cycles at 900 °C.	43
Figure 22. XRD profile of the La _{1-x} Sr _x MnO ₃ family with x = 0.5 (LSM), x = 0.25 (LSM7525) and x = 0.10 (LSM9010) after calcination at 1400 °C.	44
Figure 23. SEM images 30000 × magnification for a) LSM fresh b) LSM7525 fresh and c) LSM9010 fresh	45
Figure 24. N ₂ adsorption isotherms for LSM, LSM7525 and LSM9010.	46
Figure 25. TGA profile of LSM, LSM7525 and LSM9010 at 800 °C.	49
Figure 26. TGA profile of LSM, LSM7525 and LSM9010 at 900 °C.	49
Figure 27. O ₂ and CO production for LSM, LSM7525 and LSM9010 at 800 °C.	50
Figure 28. O ₂ and CO production for LSM, LSM7525 and LSM9010 at 900 °C.	51
Figure 29. 1-(1-X) ^{1/3} versus time for LSM9010 at 800 °C with 15 Vol% CH ₄ during reduction.	54

Figure 30. $\ln(r_0)$ versus $(1/T)$ for LSM.	54
Figure 31. $\ln(r_0)$ versus $(1/T)$ for LSM7525.	55
Figure 32. $\ln(r_0)$ versus $(1/T)$ for LSM9010.	55
Figure 33. Activation energies calculated for LSM, LSM7525 and LSM9010.....	56
Figure 34. Reduction extent as a function of size variance at 900 °C.	58
Figure 35. EDS images a) La distribution on fresh LSM b) La distribution on fresh LSM9010 c) Mn distribution on fresh LSM d) Mn distribution on fresh LSM9010 e) Sr distribution on fresh LSM f) Sr distribution on fresh LSM9010.	59
Figure 36. XRD profiles of LSM, LSM7525 and LSM9010 before and after 3 redox cycles at 900 °C.....	61
Figure 37. SEM images 30000 × magnification a) LSM after 3 redox cycles at 900 °C b) LSM7525 after 3 redox cycles at 900 °C.....	62
Figure 38. SEM images 30000 × magnification a) fresh LSMA b) fresh LSMF.	63
Figure 39. TGA profile of LSMA, LSMF and LSM at 800 °C.	64
Figure 40. TGA profile of LSMA, LSMF and LSM at 900 °C.	65
Figure 41. O ₂ and CO production for LSMA, LSMF and LSM during the three redox cycles at 800 °C.....	66
Figure 42. O ₂ and CO production for LSMA, LSMF and LSM during the three redox cycles at 900 °C.....	67
Figure 43. EDS images a) Mn distribution on the surface of fresh LSMA b) Sr distribution on the surface of fresh LSMA c) Al distribution on the surface of fresh LSMA.	68
Figure 44. XRD profiles of fresh LSMA, LSMA after 3 cycles at 900 °C, fresh LSMF and LSMF after 3 cycles at 900 °C.....	69
Figure 45. SEM images of a) Fresh LSMA b) LSMA after three redox cycles at 900 °C.	70
Figure 46. TGA profiles of LSM7525 and LSMA7525 at 800 °C.	71
Figure 47. TGA profiles of LSM7525 and LSMA7525 at 900 °C.	72
Figure 48. O ₂ and CO production for LSM7525 and LSMA7525 at 800 °C.....	73
Figure 49. O ₂ and CO production for LSM7525 and LSMA7525 at 900 °C.....	74
Figure 50. TGA profiles of CM reduced thermally and using CH ₄ at 800 °C.....	77
Figure 51. TGA profiles of LSM reduced thermally and using CH ₄ at 800 °C.....	78
Figure 52. TGA profiles of LSM9010 reduced thermally and using CH ₄ at 800 °C.....	79
Figure 53. TGA profiles of LSM9010 reduced thermally and using CH ₄ at 900 °C.....	79
Figure 54. O ₂ and CO production values for CM reduced thermally and using CH ₄ during the three redox cycles at 800 °C.....	80
Figure 55. O ₂ and CO production values for LSM reduced thermally and using CH ₄ during the three redox cycles at 800 °C.	81
Figure 56. O ₂ and CO production values for LSM9010 reduced thermally and using CH ₄ during the three redox cycles at 800 °C.	82
Figure 57. O ₂ and CO production values for LSM9010 reduced thermally and using CH ₄ during the three redox cycles at 900 °C.	83
Figure 58. $1-(1-X)^{1/3}$ versus time for thermal reduction of LSM9010 at 800 °C.....	84

Figure 59. $\ln(r_0)$ vs $(1/T)$ for LSM9010 under thermal reduction.....	85
Figure 60. TGA profiles of LSM9010, LSM7525, LSM, LSMA and LSMF for 10 redox cycles at 900 °C.....	87
Figure 61. O ₂ production values for LSM, LSM7525, LSM9010, LSMA and LSMF during the 10 redox cycles at 900 °C.	88
Figure 62. CO production values for LSM, LSM7525, LSM9010, LSMA and LSMF during the 10 redox cycles at 900 °C.	89
Figure 63. Reduction extent and final oxygen non-stoichiometry versus the Goldschmidt tolerance factor at 800 °C.....	92
Figure 64. Reduction extent and final oxygen non-stoichiometry versus the Goldschmidt tolerance factor at 900 °C.....	93
Figure 65. Reduction extent and final oxygen non-stoichiometry versus the Goldschmidt tolerance factor for samples with the same B –site composition at 800 °C.....	93
Figure 66. Reduction extent and final oxygen non-stoichiometry versus the Goldschmidt tolerance factor for samples with the same B –site composition at 900 °C.....	94
Figure 67. Reduction extent and final oxygen non-stoichiometry versus the Goldschmidt tolerance factor for samples with the same A –site composition at 800 °C.....	94
Figure 68. Reduction extent and final oxygen non-stoichiometry versus the Goldschmidt tolerance factor for samples with the same A –site composition at 900 °C.....	95
Figure 69. Reduction extent and final oxygen non-stoichiometry versus the Goldschmidt tolerance factor for LSM, LSM7525 and LSM9010 800 °C.	95
Figure 70. Reduction extent and final oxygen non-stoichiometry versus the Goldschmidt tolerance factor for LSM, LSM7525 and LSM9010 900 °C.	96
Figure 71. Reduction extent and final oxygen non-stoichiometry versus the Goldschmidt tolerance factor for samples having Mn with the same oxidation states at 800 °C.	97
Figure 72. Reduction extent and final oxygen non-stoichiometry versus the Goldschmidt tolerance factor for samples having Mn with the same oxidation states at 900 °C.	97
Figure 73. Reduction extent and final oxygen non-stoichiometry versus A –site cation size variance for samples having Mn in the B -site at 800 °C.	101
Figure 74. Reduction extent and final oxygen non-stoichiometry versus A –site cation size variance for samples having Mn in the B -site at 900 °C.	101
Figure 75. Reduction extent and final oxygen non-stoichiometry versus the A –site cation size variance for LSM, LSM7525 and LSM9010 at 800 °C.....	102
Figure 76. Reduction extent and final oxygen non-stoichiometry versus the A –site cation size variance for LSM, LSM7525 and LSM9010 at 900 °C.....	102
Figure 77. Reduction extent and final oxygen non-stoichiometry versus the A –site cation size variance for samples having Mn with the same oxidation state at 800 °C.	103
Figure 78. Reduction extent and final oxygen non-stoichiometry versus the A –site cation size variance for samples having Mn with the same oxidation state at 900 °C.	104
Figure 79. Reduction extent and final oxygen non-stoichiometry versus the A –site metal and oxygen electronegativity difference for samples having Mn in the B –site at 800 °C.	106

Figure 80. Reduction extent and final oxygen non-stoichiometry versus the A –site metal and oxygen electronegativity difference for samples having Mn in the B –site at 900 °C.	106
Figure 81. Reduction extent and final oxygen non-stoichiometry versus the B –site metal and oxygen electronegativity difference for samples having the same A –site composition at 800 °C.....	107
Figure 82. Reduction extent and final oxygen non-stoichiometry versus the B –site metal and oxygen electronegativity difference for samples having the same A –site composition at 900 °C.....	107
Figure 83. Born-Haber cycle for the computation of La-O bond strength in perovskite with La in the A -site.	111
Figure 84. Reduction extent and final oxygen non-stoichiometry versus A –site metal-oxygen bond strength for samples with Mn in the B –site at 800 °C.....	112
Figure 85. Reduction extent and final oxygen non-stoichiometry versus A –site metal-oxygen bond strength for samples with Mn in the B –site at 900 °C.....	112
Figure 86. Reduction extent and final oxygen non-stoichiometry versus B –site metal-oxygen bond strength for samples with the same A –site composition at 800 °C.....	113
Figure 87. Reduction extent and final oxygen non-stoichiometry versus B –site metal-oxygen bond strength for samples with the same A –site composition at 900 °C.....	114
Figure 88. Reduction extent and final oxygen non-stoichiometry versus A –site metal-oxygen bond strength for LSM, LSM7525 and LSM9010 at 800 °C.....	114
Figure 89. Reduction extent and final oxygen non-stoichiometry versus A –site metal-oxygen bond strength for LSM, LSM7525 and LSM9010 at 900 °C.....	115
Figure 90. Reduction extent and final oxygen non-stoichiometry versus A –site metal-oxygen bond strength for the samples having Mn with the same oxidation state at 800 °C.	116
Figure 91. Reduction extent and final oxygen non-stoichiometry versus A –site metal-oxygen bond strength for the samples having Mn with the same oxidation state at 900 °C.	116
Figure 92. O ₂ and CO production for LSM and LSM7525 during three redox cycles at 900 °C.....	133

List of Symbols, Abbreviation and Nomenclature

Symbol	Definition
ABO_3	Perovskite oxide with A = alkaline, alkaline-earth or rare-earth metals, B = d-block transition metal, O = oxygen
$(A'_{1-x}A''_x)BO_3$	Perovskite oxide with A' = trivalent lanthanide cation, A'' = divalent alkaline earth cation, B = d-block transition metal, O = oxygen
A_r	Pre-exponential factor (s^{-1})
CM	$CaMnO_3$
C_n	Coordination number
D_O	Bond dissociation energy of O_2 ($kJmol^{-1}$)
δ	Oxygen non-stoichiometry
Δ_A	Difference between the ionic radii of the A' and A'' cations for the $(A'_{1-x}A''_x)BO_3$ perovskite (nm)
ΔH	Change in enthalpy ($kJmol^{-1}$)
ΔH_f	Enthalpy of formation ($kJmol^{-1}$)
ΔH_s	Heat of sublimation ($kJmol^{-1}$)
Δm_{red}	Change in mass of the perovskite sample after the completion of the reduction phase (mg)
E_a	Activation energy ($kJmol^{-1}$)
LBM	$La_{0.5}Ba_{0.5}MnO_3$
LCM	$La_{0.5}Ca_{0.5}MnO_3$
LSM7525	$La_{0.75}Sr_{0.25}MnO_3$
LSM9010	$La_{0.90}Sr_{0.10}MnO_3$
LSM	$La_{0.5}Sr_{0.5}MnO_3$
LSMA7525	$La_{0.75}Sr_{0.25}Mn_{0.5}Al_{0.5}O_3$
LSMA	$La_{0.5}Sr_{0.5}Mn_{0.5}Al_{0.5}O_3$
LSMC	$La_{0.5}Sr_{0.5}Mn_{0.5}Co_{0.5}O_3$
LSMF	$La_{0.5}Sr_{0.5}Mn_{0.5}Fe_{0.5}O_3$
LSMN	$La_{0.5}Sr_{0.5}Mn_{0.5}Ni_{0.5}O_3$
m_0	Mass of the perovskite sample before reduction (mg)
m_f	Final mass of the perovskite sample after reduction (mg)
$m_{f,red}$	Mass of the perovskite sample at the completion of the reduction phase (mg)
$m_{i,red}$	Mass of the perovskite sample at the onset of the reduction phase (mg)
m_s	Original mass of the perovskite sample (mg)
m_t	Mass of the perovskite sample at time t (mg)

M_O	Molar mass of monoatomic oxygen (g/mol)
M_s	Molar mass of the perovskite sample (mg)
$M - O$	Metal-oxygen bond strength (kJmol^{-1})
p/p_0	Relative pressure
r_0	Intrinsic surface reaction rate when conversion fraction is zero (s^{-1})
R	Intrinsic surface reaction rate (s^{-1})
r_A	A –site ionic radii (nm)
r_B	B –site ionic radii (nm)
r_O	Ionic radii of oxygen (nm)
R	Universal gas constant ($8.314 \text{ Jmol}^{-1}\text{K}^{-1}$)
R_{ext}	Reduction extent
σ^2	A –site cation size variance (pm^2)
T	Goldschmidt tolerance factor
T	Temperature (K)
X	Conversion fraction
YSM	$\text{Y}_{0.5}\text{Sr}_{0.5}\text{MnO}_3$

Abbreviation	Definition
BET	Brunauer-Emmett-Teller
BJH	Barrett-Joyner-Halenda
EDS	Energy Dispersive Spectroscopy
FESEM	Field Emission Scanning Electron Microscope
GHG	Greenhouse Gas
IEA	International Energy Agency
IUPAC	International Union of Pure and Applied Chemistry
NASA	National Aeronautics and Space Administration
SEM	Scanning Electron Microscope
TGA	Thermogravimetric Analysis
XRD	X-Ray Powder Diffraction

CHAPTER ONE: INTRODUCTION

1.1. Problem Statement and Objectives

The planet Earth might be a “Pale Blue Dot” in the vastness of the cosmos as described by the late Carl Sagan [1]. Nevertheless, it is a home to 8.7 million diverse array of species [2], [3]. All the 7.6 billion humans existing today are categorized as the species Homo sapiens [4], [5]. Thus, it follows that the number of individual life forms inhabiting Earth is mind-numbingly large. As seen through the human eyes, at first glance life may be perceived as a separate or individual entity. However, the interconnectedness of the Earth’s systems has resulted in the abundant life forms [6]. The interconnectedness and interdependence of life on Earth has been beautifully and poetically described by Alan Watts: “...Each one of us, not only human beings but every leaf, every weed, exists in the way it does, only because everything else around it does. The individual and the universe are inseparable.” [7].

The Earth’s climate is governed by the interaction between the sun and the Earth’s systems comprising of the geosphere and biosphere [6]. A delicate balance is created between all the elements present in the Earth’s systems through the web of interconnectedness. Consequently, a significant change in one element of the climate system can disturb the equilibrium between the Earth’s systems [6]. The evidences for this claim are clearly visible. The CO₂ concentration in the atmosphere has increased by 43% in the last 150 years, reaching to a current level of more than 400 ppm [8], [9]. At the same time, the global surface temperature has been increasing since the beginning of the 20th century and the sea level has been rising since the end of the 19th century [10], [11]. Global warming

and climate change can trigger frequent extreme weather events and also displace 143 million people by 2050 [12], [13].

The issue or problem the world is currently facing is multifaceted. On one hand, the threat posed by global warming and climate change caused by anthropogenic activities is alarming. Simultaneously, human civilization is strongly dependent on fossil fuels for its primary source of energy and will continue to be heavily reliant on fossil fuels in the foreseeable future. Currently, 81% of the global primary energy is derived from fossil fuels [14]. It is predicted that by 2040, 77% of the global primary energy will be acquired from fossil fuels [15]. The growing population and changing lifestyle will accelerate the global energy demand. It has been forecasted that the global energy usage will increase by 28% from 2015 to 2040 [15].

Converting CO₂ to fuels or useful chemicals can tackle both the issue of climate change and meeting the global energy demand. Presently, about 200 Mt of CO₂ per year is used for synthesizing chemicals and for non-chemical purposes [16]. The fact that anthropogenic activities release around 32, 000 Mt of CO₂ a year suggests that there are plenty of opportunities to improve the current CO₂ utilization processes and to develop new technologies for CO₂ conversion [16]. However, the great stability of the CO₂ molecule, high cost of CO₂ capture, separation, purification and transportation, high cost of co-reactants, small market size for CO₂ utilization and lack of appropriate incentives from the government and the lack of commitment from the industry are the key challenges for CO₂ conversion [17]–[19].

CO₂ can be converted into valuable chemicals and fuels via thermochemical, electrochemical and photochemical pathways. In terms of CO₂ conversion, the

thermochemical conversion of CO₂ is more mature than the electrochemical and photochemical methods [16], [20]. CO₂ could be converted electrochemically into desired products such as hydrocarbons, CO and formate depending on the metal present as the electrode [20]. The field of electrochemical conversion of CO₂ has received a great deal of attention from the industry and academia recently [20]. Nevertheless, low Faradaic efficiencies, low solubility of CO₂ in water, high cost of product separation and deactivation of electrodes are some challenges faced in the area of electrochemical conversion of CO₂ [20]. Mostly, photocatalysts based on TiO₂ are used for the photochemical conversion of CO₂ into fuels [20]. The data from 1980s to 2013 reveal the absence of significant development in improving the performances of photocatalysts for CO₂ conversion [20]. Despite the great amount of research activities regarding photocatalysis, low photon efficiency of materials and inadequate photocatalytic reactors are some of the hurdles encountered in the photochemical conversion of CO₂ [20].

Thermochemically CO₂ can be directly converted into CH₄, hydrocarbons, methanol and dimethyl ether and indirectly converted into CO [20]. CO can later be converted into valuable oxygenates and hydrocarbons [20]. In order to develop thermochemical processes with a low carbon footprint, numerous studies have been performed regarding solar-powered thermochemical splitting of CO₂ [21]–[24]. The redox properties of non-stoichiometric oxides such as ceria has been widely investigated for the thermochemical splitting of CO₂. Ceria has been in the spotlight because of its fast kinetics, favorable oxidation thermodynamics and structural stability [25]. However, the poor reduction thermodynamics of ceria results in elevated temperatures of 1723 K for its reduction [25]–[28]. Perovskites have recently gained attention in the field of thermochemical splitting of

CO₂ because of the superior reduction performance of perovskites in comparison to ceria, the stability of the perovskites' crystallographic structure after undergoing multiple redox cycles and the plethora of perovskite materials with varying physicochemical properties that could be easily synthesized [25], [26], [29]. In particular, manganite-based perovskites have displayed outstanding chemical activity and stability [25], [26], [29], [30].

Perovskite oxides are structures with the unit cell formula ABO₃, where, A is alkaline, alkaline-earth or rare-earth metals, B is d-block transition metal and O is oxygen [31]. The redox properties of perovskites are utilized for the thermochemical splitting of CO₂ [22], [30]. Perovskites can undergo redox cycling under isothermal conditions or using a temperature-swing approach [32]. Most of the thermochemical splitting of CO₂ investigations have utilized the temperature-swing method where the perovskite is reduced at high temperatures of 1400 °C and re-oxidized at 1050 °C [26], [29], [30]. Studies have shown that isothermal processes eliminates the solid state heat recovery which is required in processes incorporating the temperature-swing approach [32]. *Venstrom et al.* have shown that isothermal thermochemical splitting of CO₂ produces CO at rates similar to approaches using temperature-swing [32]. *Muhich et al.* have illustrated that isothermal H₂O splitting produces more H₂ than the temperature-swing H₂O splitting method [33]. According to the work of *Muhich et al.*, the frequent heating and cooling of the metal oxides results in a lower overall efficiency of the process as both heat and time is lost [33]. Most of the studies regarding the thermochemical splitting of CO₂ using perovskites utilizes only thermal energy to reduce the perovskites during the redox cycling [26], [29], [30]. However, using CH₄ as a reducing agent can lower the temperature required for reduction of the perovskite [21].

Integrating various metals in the A and B –site of manganite-based perovskites have resulted in redox materials displaying excellent thermochemical splitting of CO₂ performances. Manganite-based perovskites materials such as La_{0.5}Sr_{0.5}MnO₃, Y_{0.5}Sr_{0.5}MnO₃ and La_{0.5}Ca_{0.5}MnO₃ have shown stronger activity for the thermochemical splitting of CO₂ to CO than ceria [26], [29], [34]. Similarly, the work of *Ezbiri et al.* reveal that substituting the B –site of La_{1-x}Sr_xMnO₃ perovskite material with Al enhances its reduction extent and stability [25]. The Fe content in La_{1-x}Sr_xMn_{1-y}Fe_yO₃ perovskites greatly affects its magnetic and transport properties [35]. Also, Fe-based oxygen carriers show strong activity for H₂ production from H₂O splitting and total oxidation of CH₄ reactions [36]. La_{1-x}Sr_xFeO₃ perovskites have displayed good stability and repeatability for CH₄ oxidation reactions [36]. Multiple studies have illustrated that substituting the A and B –site of perovskites with different metals affects its activity for CH₄ oxidation reactions [37].

Therefore, the objectives of the present study are outlined below:

1. Investigate the redox performances of manganite-based perovskites under isothermal conditions and under reduction condition where CH₄ is used as a reducing agent. To be more specific, investigate the effect A and B –site substitution on the CO₂ conversion performance of the manganite-based perovskites and discuss the performances using XRD, SEM and EDS.
2. Investigate kinetic parameters such as activation energy for the reduction phase of the perovskites and examine different factors that could affect the reduction of the perovskite such as temperature, Goldschmidt tolerance factor, size variance, metal-oxygen electronegativity difference and metal-oxygen bond strength.

1.2. Methodology

Initially the effect of A –site substitution on the CO₂ conversion performances of the manganite-based perovskites was investigated. The redox cycles of four different samples (CaMnO₃, La_{0.5}Ca_{0.5}MnO₃, La_{0.5}Sr_{0.5}MnO₃ and Y_{0.5}Sr_{0.5}MnO₃) with varying A –site composition were analyzed and compared. Based on the activity and stability of the material, La_{0.5}Sr_{0.5}MnO₃ was identified as the best performing material amongst the four samples investigated. Factors affecting the activity and stability of the samples were examined. Then an optimal A –site composition for the family of La_{1-x}Sr_xMnO₃ perovskite was further investigated by varying the Sr content (x = 0.5, 0.25, 0.10). La_{0.5}Sr_{0.5}MnO₃ was identified as the optimal composition for the family of La_{1-x}Sr_xMnO₃ perovskite based on its activity and stability. Activation energy for the reduction of the perovskites was evaluated using the grain model. In order to study the effect of B –site substitution on the CO₂ conversion performances of the manganite-based perovskites La_{0.5}Sr_{0.5}Mn_{0.5}Al_{0.5}O₃, La_{0.5}Sr_{0.5}Mn_{0.5}Fe_{0.5}O₃ and La_{0.75}Sr_{0.25}Mn_{0.5}Al_{0.5}O₃ were synthesized. The redox performances of La_{0.5}Sr_{0.5}Mn_{0.5}Al_{0.5}O₃, La_{0.5}Sr_{0.5}Mn_{0.5}Fe_{0.5}O₃ and La_{0.75}Sr_{0.25}Mn_{0.5}Al_{0.5}O₃ revealed no significant improvement in the performance when compared to the La_{0.5}Sr_{0.5}MnO₃ and La_{0.75}Sr_{0.25}Mn_{0.5}O₃. Long-term stability tests are performed to further investigate the stability of the perovskite materials. The trends observed in the reduction performances of the perovskites were successfully analyzed using different factors such as temperature, Goldschmidt tolerance factor, size variance, metal-oxygen electronegativity difference and metal-oxygen bond strength.

1.3. Thesis Overview

Chapter 2 of this thesis contains literature review of key topics relevant to this study such as global warming and climate change, global energy demand, different CO₂ conversion pathways and perovskites as materials used for the thermochemical splitting of CO₂.

Chapter 3 presents the detailed methodology of the study, the results of the study and the thorough discussion of the results. Synthesis method followed by characterization techniques such as XRD, SEM, EDS and N₂ physisorption have been discussed. Similarly, the data obtained from the Thermogravimetric Analyzer showcasing the redox cycles of the perovskites are discussed. The trends observed in the redox performances of the different perovskites are explored and the reasons for identifying the optimal composition have been presented. Kinetic parameters such as activation energy have been evaluated. In addition, long-term stability tests have also been examined in this section.

Chapter 4 investigates the possible factors that could affect the reduction of the perovskites studied such as Goldschmidt tolerance factor, size variance, metal-oxygen electronegativity difference and metal-oxygen bond strength. These factors are used to explain the trends observed in the reduction performances of the perovskites studied.

Chapter 5 summarizes the thesis with the key conclusions of the study and also provides some recommendations.

1.4. Statement of Contributions

All the experiments, analysis of experimental data and writing of the thesis were carried out by Pradeep Shrestha under the supervision of Dr. Nader Mahinpey (Supervisor). In addition, Dr. Mahesh Nair (Post-Doctoral fellow in the Energy and Environment Research Group) provided helpful guidance during both the experimental part and analytical part of the study.

CHAPTER TWO: LITERATURE REVIEW

2.1. Global Warming and Climate Change

The planet Earth is located at an incredible distance of 149,600,000 km from the sun [38]. However, this giant ball of glowing gases powers the multitude of living organisms inhabiting Earth [39], [40]. As this blue planet rotates and revolves around the sun, continuous change takes place at the cellular level and the gigantic tectonic plates are always on the move [41]. The Earth's systems are comprised of the biosphere and geosphere [42]. The geosphere can be further divided into lithosphere, atmosphere, hydrosphere and cryosphere [42]. The energy from the sun fuels the Earth's climate system [6]. The interaction between the sun, biosphere and geosphere regulates the Earth's climate [6]. The interconnectedness and interdependence of all the Earth's systems creates a delicate balance between all these systems. Thus, a significant alteration in just one of the elements of the climate system can disrupt the balance between the Earth's systems [6].

Numerous scientific evidences show that the planet Earth has been plagued by global warming and climate change. Research conducted by the National Aeronautics and Space Administration's (NASA) Goddard Institute for Space Studies shows that the global surface temperature has been increasing since the dawn of the 20th century as illustrated in Figure 1 [10]. 2016 has been identified as the warmest year recorded so far [10]. Similarly, sea level has also been rising from 1880 as shown in Figure 2 [11].

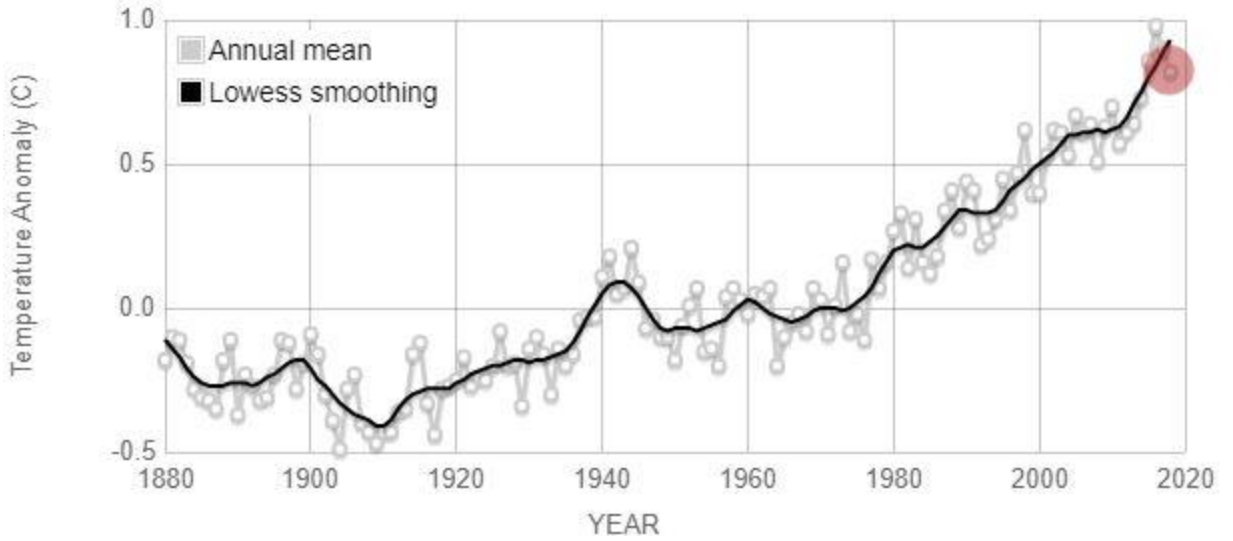


Figure 1. Change in global surface temperature relative to 1951-1980 average temperatures [10].

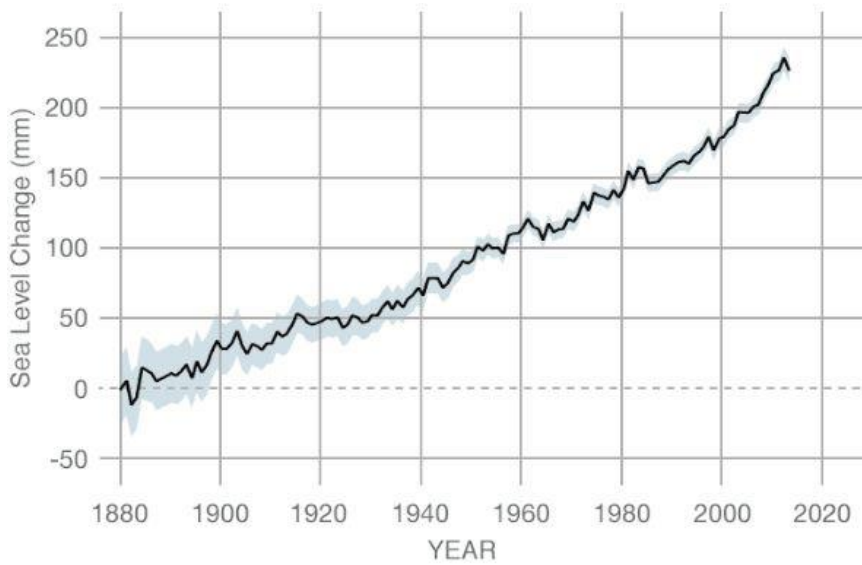


Figure 2. Change in sea level from 1870 to 2013 [11].

Increasing global surface temperatures and rising sea level are just the tip of the iceberg. Shrinking ice sheets, retreating glaciers, increasing occurrence of extreme weather events and acidification of oceans are further evidences of climate change [8].

Majority of the climate scientists have reached a consensus that the primary cause of global warming and climate change is the escalation of the greenhouse effect stemming from anthropogenic activities [9]. The greenhouse gases (GHGs) like water vapor, carbon dioxide, methane and nitrous oxide in the atmosphere trap some of the heat radiating away from earth, thus keeping the planet warm. Moreover, GHGs such as CO₂ have a longer life-span [9]. So, as the concentration of GHGs such as CO₂ increases in the atmosphere, the temperature of the planet rises up. CO₂ is considered as the major contributor to global warming and climate change [9]. Figure 3 shows the CO₂ level in the atmosphere from 400,000 years ago till now. Currently, the CO₂ level in the atmosphere is at more than 400 ppm, which is the highest level it has ever been since 400,000 years ago [8].

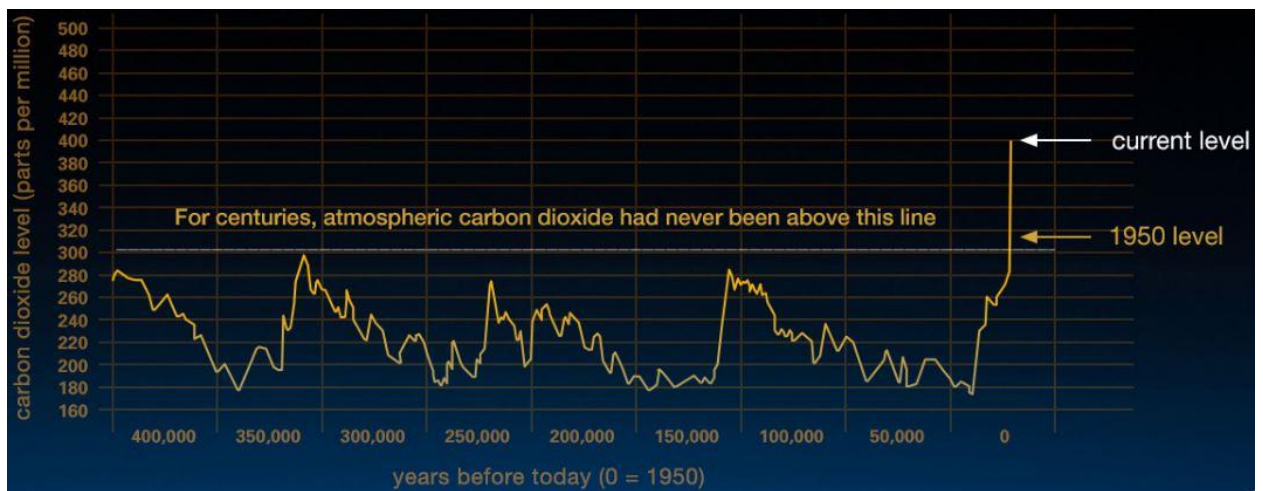


Figure 3. CO₂ level in the atmosphere from 400,000 years ago to the present time [8].

The second half of the 18th century marked the beginning of the industrial revolution [43]. With the advent of the industrial revolution, humans started using fossil fuels (coal, oil and natural gas) as an additional source of energy [44]. As new technologies powered by fossil fuels, such as steam engine, started to emerge, the use of fossil fuels increased rapidly. In

addition, the industrial revolution improved the quality of life of humans. Consequently, the population of the world increased by 10 times from 1700 to 2011 [44]. Both the increase in population and the change in lifestyle compounded the demand of energy. To fulfill the energy demand, more and more fossil fuels were utilized. As a result, in the last 150 years the concentration of atmospheric CO₂ increased by 43 % [9].

The consequences of global warming and climate change are devastating. Changes in precipitation patterns, more frequent droughts and heat waves, more intense hurricanes and 1-4 feet increase in sea level by 2100 are some of the long-term effects of global climate change [13]. Since 2008, on average 22.5 million people have been displaced by climate or weather-related calamities every year [45]. According to the World Bank's report, without the joint actions taken at the national and global levels, because of climate change more than 143 million people could be displaced by 2050 [12].

2.2. Energy Demand

The current global human civilization heavily relies on fossil fuels as its primary source of energy. As of 2016, fossil fuels (coal, oil and natural gas) comprises 81% of the total global primary source of energy [14]. The breakdown of the global primary sources of energy is illustrated in Figure 4.

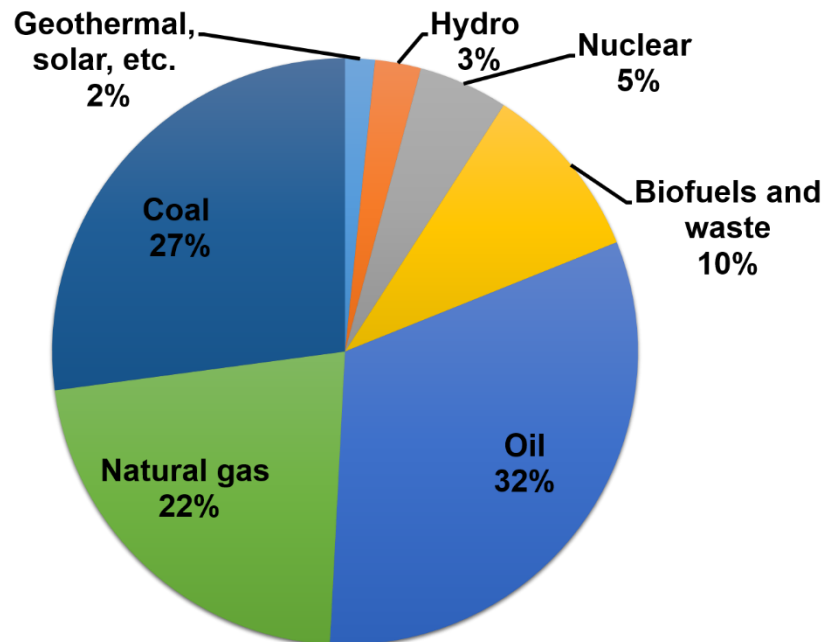


Figure 4. Global primary sources of energy in 2016. Based on IEA data from the IEA (2018) World Energy Balances, www.iea.org/statistics. All rights reserved; as modified by Pradeep Shrestha

Similarly, 65% of the total global electricity is generated using fossil fuels (coal, oil and gas) [46]. The high inefficiencies of electric power plants and vehicles further contributes to the emission of GHGs such as CO₂. Electric power plants can only convert 35% of the

energy input into useful energy output [19], [47]. Likewise, 65-80 % of the energy input is lost in vehicles such as cars [19].

According to a report published by the United Nations, the world population will increase from current population of 7.6 billion to 8.6 billion in 2030 and to 9.8 billion in 2050 [5]. Moreover, our lifestyle has become more energy intensive. Currently a person uses about three times more energy than in 1900 [48]. Both the growing population and more energy intensive lifestyle escalates the global energy demand. Consequently, it is projected that the global energy usage will increase by 28% from 2015 to 2040 [15]. Most importantly it has been predicted that fossil fuels will remain as the dominant primary source of energy in the foreseeable future. By 2040, fossil fuels will constitute 77% of the global primary source of energy [15].

2.3. CO₂ Conversion

The consequences of climate change continues to be a threat for life on Earth. At the same time, humans are largely dependent on fossil fuels at the present time and will continue to be heavily reliant on it in the near future. An alternative method to simultaneously tackle the problem of climate change and meet the global energy demand is converting CO₂ to fuels or useful chemicals.

2.3.1. Background, Challenges and Opportunities

The utilization of CO₂ into chemicals had been realized and implemented since 150 years ago [16]. The first major CO₂ conversion process was introduced in 1869 as the formation of salicylic acid from phenol-salts and CO₂. The second major CO₂ utilization process entered the scene in 1882 as CO₂ was converted into NaHCO₃-Na₂CO₃. Developed in 1922, synthesis of urea from CO₂ and ammonia has been identified as the third major CO₂ conversion process discovered [16]. The catalytic conversion of CO₂ into methanol and organic carbonates was later introduced in 1970. Currently, around 200 Mt of CO₂ are utilized every year for the synthesis of chemicals and also for other non-chemical purposes [16]. Out of the 200 Mt, 114 Mt and 8 Mt of CO₂ are used to synthesize urea and methanol respectively [16]. Compared to the 32, 000 Mt/y of CO₂ released as a result of human activities, the present CO₂ utilization capacity definitely requires further improvement and expansion [16].

However, one of the major hurdles in the conversion of CO₂ is its stability. CO₂ is a linear non-polar molecule with double bonds shared between the carbon and oxygen atoms [47] [19]. The carbon in the CO₂ molecule is electrophilic in nature whereas the oxygen atoms

are nucleophilic [47]. The carbon atom in the CO₂ molecule is at its highest oxidation state of +4 [17]. The conversion of CO₂ into products having carbon in the same oxidation state as CO₂ requires relatively lower energy [16]. Conversion of CO₂ into carboxylates, lactones, carbamates and urea are examples of low energy processes. The conversion of CO₂ into products having carbon with oxidation states of +2 or lower requires higher energy. The synthesis of CO₂ into products such as HCOOH, CO, CH₃OH and H₂CO are high energy processes [16]. Synthesis of energy dense fuels from CO₂ using thermal energy derived from fossil fuels causes more emission of CO₂ than its conversion [16]. Consequently, CO₂ has been mostly converted to simpler chemicals using less energy intensive pathways and energy dense co-reactants such as olefins, dienes and amines [16]. Nevertheless, studies show that new catalytic processes for CO₂ conversion can utilize between 300 to 500 Mt/y CO₂ at most [16].

Besides the high energy intensity of CO₂ conversion processes, there are other challenges for the utilization of CO₂ as well. CO₂ needs to be captured, separated, purified and transported before it can be converted. The high cost associated with the capture, separation, purification and transportation of CO₂ hinders the development of CO₂ conversion projects [19]. Similarly, the very high cost of co-reactants such as H₂ for the conversion of CO₂ into fuels is a barrier for carrying out CO₂ utilization projects [18], [19]. The small market size for CO₂ utilization processes is discouraging [19]. Minimal government incentives and the absence of commitment from the industry further impedes the development of CO₂ conversion projects [19].

Despite the obstacles, CO₂ conversion remains an interesting field for new and innovative technologies. Numerous research and investigations have been carried out in the field of

CO₂ conversion. The objective is to convert CO₂ to useful chemicals and fuels via routes that are less energy intensive and have a low carbon footprint.

2.3.2. Different Pathways for CO₂ Conversion

The conversion of CO₂ into fuels and useful chemicals can be carried out using heterogeneous or homogeneous catalysts. Heterogeneous catalysts are preferred because they are easy to recycle and also the generated products can be easily separated from the catalyst [49]. Moreover, CO₂ can be converted thermocatalytically, electrocatalytically and photocatalytically. Direct hydrogenation of CO₂ into valuable products such as methane, hydrocarbons and oxygenates can take place using H₂ [20]. Similarly, using CH₄, CO₂ can be converted into CO and H₂. In an additional step, CO can be converted into hydrocarbons and oxygenates [20].

There are multiple sources of H₂ required for the hydrogenation of CO₂. However, for a sustainable environment it is key that the generation of H₂ has a low carbon footprint. Currently, H₂ is derived primarily from the steam reforming of methane [20]. The energy required for this highly endothermic reaction is presently supplied by the combustion of fossil fuels [20]. Consequently, CO₂ is released. In addition, the CO produced by the steam reforming of methane reaction is converted to CO₂ via water-gas shift reaction. Even though autothermal reforming can reduce the CO₂ emissions, challenges such as coking and poisoning of the catalysts still persist [20]. Similarly, H₂ can also be produced from the liquefaction, pyrolysis and gasification of biomass [20]. H₂ generated from the

electrolysis of water reduces the separation costs [20]. However, the electricity required for the electrolysis process when generated from fossil fuels contribute to the release of CO₂. Photocatalysts such as metal oxides, nitrides and sulfides as well as green algae and cyanobacteria can also dissociate water into H₂ and O₂ [20]. But the H₂ productivity is low using the aforementioned photocatalysts and microorganisms. From an environmental perspective, the production of H₂ from water using renewable energy sources is favorable.

The electrocatalytic conversion of CO₂ has garnered a lot of attention since the past few decades [20]. The electrocatalytic conversion of CO₂ dates back to the 19th century [20]. CO₂ can be directly converted into valuable products at the surface of the electrodes [20]. The selectivity of the products is determined by the metal present as the electrode [20]. Cu electrode favors the formation of hydrocarbons from CO₂ [20]. Au, Ag and Zn electrodes are selective towards the generation of CO from CO₂ [20]. Likewise, In, Pb, Sn and Cd electrodes mainly generate formate from CO₂. Ni, Fe, Pt and Ti electrodes mostly yield H₂ [20]. Despite the enormous amount of attention from the industry and academia, low Faradaic efficiencies, low solubility of CO₂ in water, high cost associated with product separation and deactivation of electrodes are some of the major hurdles encountered in the field of electrocatalytic conversion of CO₂ [20].

The 1970s mark the beginning of photocatalysis [20]. Data from 1980s to 2013 reveal lack of substantial development in enhancing the performance of photocatalyst for the conversion of CO₂ to fuels [20]. Most of the photocatalysts used in the conversion of CO₂ to fuels are based on TiO₂ [20]. P25 is a commercially used titania photocatalyst as it is readily available [20]. Addition of noble metals such as Pd, Rh, Pt, Au and Cu as co-catalysts increases the rate of photocatalytic conversion of CO₂ [20], [51]. Similarly, the

research work conducted by the group of professor Masakazu Anpo illustrate that TiO₂ based catalysts supported on zeolites and mesoporous structures display great photocatalytic activities [20]. Despite the numerous research activities in the field of photocatalysis, the low photon efficiency of materials and inadequate photocatalytic reactors are some of the challenges in the photocatalytic conversion of CO₂ [20].

Thermocatalytically, CO₂ can be converted into valuable fuels and chemicals such as hydrocarbons and oxygenates. The CH₄ produced from the methanation of CO₂ can be used in steam reforming processes, for the generation of heat and electricity as well as in vehicles [20]. Nickel and supported noble metals can convert CO₂ to CH₄ [20]. Co and Fe-based catalysts have the ability to directly convert CO₂ into hydrocarbons [20]. Fe-based catalysts have been extensively used for CO₂ Fischer-Tropsch processes. Doping Fe-based catalysts with Mn, Cu, K and Ce improves the selectivity of the catalyst towards higher hydrocarbons [20]. Metals and oxides of copper and zinc have the ability to convert CO₂ to methanol [20]. Methanol is considered as a vital intermediate during the mass production of chemicals [20]. In the 1980s Lurgi GmbH developed a process to convert CO₂ to methanol [20]. Only in 2011 the first plant to convert CO₂ to methanol was set up in Iceland by Carbon Recycling International [20]. However, the low productivity of methanol is still a major problem [20]. The methanol produced in one reactor can be converted into dimethyl ether (DME) in another reactor via dehydration [20]. An alternate method is to use bifunctional catalysts to convert CO₂ to DME in one step [20]. The DME produced can be used in vehicles as a replacement for diesel [20].

For creating a low carbon footprint scenario it is key that heat used in the thermocatalytic processes are derived from renewable energy sources. Thus, numerous research work have

been carried out in the field of solar powered thermochemical splitting of CO₂ [21]–[24]. CO produced from the thermochemical splitting of CO₂ can be used to produce valuable chemicals such as methanol and higher hydrocarbons [20]. The redox properties of non-stoichiometric metal oxides such as ceria have been widely investigated in the field of solar-driven thermochemical splitting of CO₂. Ceria has garnered most of the attention because of its fast kinetics, favorable oxidation thermodynamics and structural stability [25]. However, ceria displays poor reduction thermodynamics as extremely high temperatures of 1723 K are required for reduction of ceria [25]–[28]. Although perovskite oxides have been extensively investigated for solid oxide fuel cells, recently perovskite oxides have sparked interest in the field of solar powered thermochemical splitting of CO₂ [25]. The superior reduction performance of perovskites in comparison to ceria, the stability of the perovskites' crystallographic structure after undergoing multiple redox cycles and the plethora of perovskite materials with varying physicochemical properties that could be easily synthesized makes perovskites an extremely attractive material for the thermochemical splitting of CO₂ [25], [26], [29].

2.4. Perovskites

2.4.1. History and Background

The term perovskite was coined by Gustav Rose in 1839 after the Russian Secretary of the Interior Lev Alexeievitch Perovsky (1792 – 1856) to describe the structure of the mineral, CaTiO_3 , then discovered [52]. All other materials having similar structure to CaTiO_3 are characterized as perovskites. Underneath the surface of the earth from the seismic discontinuity at 670 km to the core-mantle boundary, the perovskite phase abundant in MgSiO_3 occupies about 50-90% of the volume [52]. Besides the naturally occurring perovskites such as CaTiO_3 and MgSiO_3 , perovskites can also be synthesized via sol-gel, hydrothermal, solid state reaction, electrospinning and polymeric precursor methods [53].

Perovskite oxides are structures with the unit cell formula ABO_3 , where, A is alkaline, alkaline-earth or rare-earth metals, B is d-block transition metal and O is oxygen [31].

Although majority of the compounds with the perovskite structures are oxides, there are also nitrides, halides and carbides with the perovskite structure [54]. An ideal cubic perovskite structure for the compound SrTiO_3 is illustrated in Figure 5. As illustrated in Figure 5, Sr^{2+} , Ti^{4+} and O^{2-} species form a cubic lattice with Sr^{2+} at the center of the cube [55]. $[\text{TiO}_6]$ octahedral is formed at each corner of the cube with Ti^{4+} at the middle of the octahedral and also at the corner of the cubic lattice [55]. Usually the

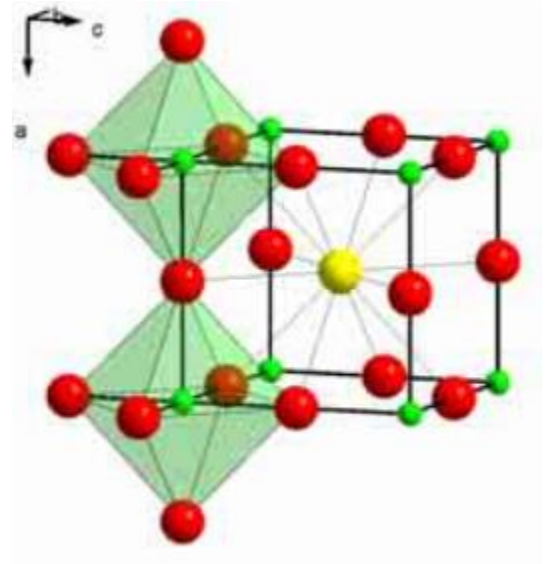


Figure 5. Ideal cubic perovskite structure of SrTiO_3 [55].

coordination number for the A –site cation is 12 and the coordination number for the B –site cation is 6. Thus, usually the A –site cation is larger than the B –site cation [54], [56].

2.4.2. Properties

One of the exceptional properties of perovskite is that it can accommodate a wide range of cations in its A and B –site. About 90% of the metals in the periodic table can form stable perovskite oxide structures [54]. Different metals can be partially or completely substituted in the A and B –site of perovskites [29], [54]. Thus, a wide range of perovskite compounds with varying physicochemical properties can be synthesized [25], [26], [37].

Although a wide range of perovskite compounds could be synthesized, most of the perovskite compounds do not have the ideal cubic structure. In the beginning the mineral CaTiO_3 was assumed to have a cubic structure. However, the orthorhombic structure of CaTiO_3 was later discovered [56]. There are multiple factors responsible for the distortion of the perovskite structure from the ideal cubic structure. Ionic radii of cations is one of the major factors contributing to the distortion of the cubic perovskite structure. The Goldschmidt tolerance factor (t) measures the deviation of perovskite structure from the ideal cubic structure. The Goldschmidt tolerance factor can be computed using the following formula [55]:

$$t = \frac{r_A + r_O}{\sqrt{2}(r_B + r_O)} \quad (1)$$

Where, r_A and r_B are the A –site and B –site ionic radii respectively. r_O is the ionic radii of oxygen. For an ideal cubic perovskite structure $t = 1$ [54], [55]. At room temperature only a small fraction of perovskites have simple cubic structure [56]. The perovskite maintains a cubic structure for $0.89 < t < 1$ according to *Johnsson et al.* [55]. Perovskites with $0.8 <$

$t < 1$ are usually stable as pointed out by *Attfield* [57]. According to the formula for the tolerance factor, as r_A decreases t also decreases. The BO_6 octahedra of the perovskite structure tilts to fill up the space left out by the smaller A –site metal for perovskites with values of t in the lower section of the range $0.8 < t < 1$ [55], [58]. GdFeO_3 has a t value of 0.81 [55]. The tilting of the FeO_6 octahedra is illustrated in Figure 6, resulting in an orthorhombic structure [55]. Perovskites, such as BaNiO_3 , with $t > 1$ have a hexagonal structure [55]. The values of t affects the stability of the perovskite. Studies performed by *Dey et al.* shows that manganite based perovskites with the lowest t value produces the highest amount of O_2 per gram of catalyst [26]. Similarly, *Navrotsky* showed that for perovskites in the form $\text{A}^{2+}\text{B}^{4+}\text{O}_3$, as t decreases the perovskite becomes less stable [59].

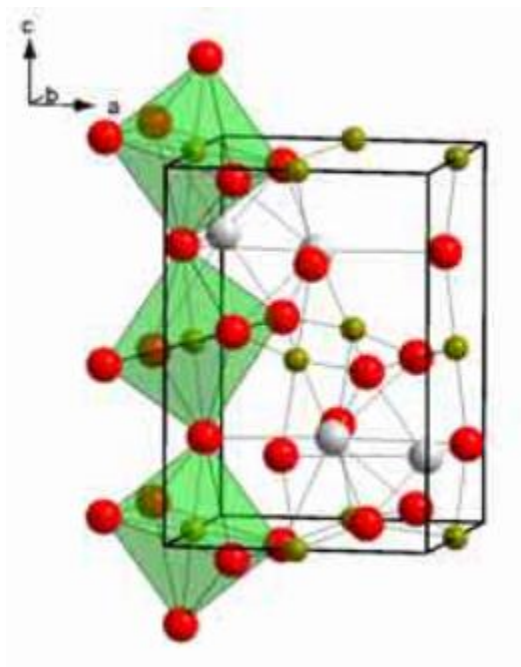


Figure 6. Tilting of the FeO_6 octahedra in the case of GdFeO_3 perovskite [55].

In some perovskites the distortion of the structure can be attributed to the Jahn-Teller active B –site cations [55]. In the perovskite LnMnO_3 ($\text{Ln} = \text{La, Pr or Nb}$), the electrons in the $3d^4$

orbital for Mn^{3+} ions are divided into 3 t_g and 1 e_g electron [55]. Having odd number of electrons in the e_g orbital stretches the MnO_6 octahedral [55].

Another factor that can explain some of the properties of perovskites is the statistical variance of the A –site cation radius distribution or the A –site cation size variance (σ^2). Perovskites with two different cations in the A –site can be represented as $(A'_{1-x}A''_x)\text{BO}_3$, where A' is a trivalent lanthanide cation and A'' is a divalent alkaline earth cation. The disorder in the structure of the perovskite caused by the random distribution of A –site cations with different radii is quantified using σ^2 [57], [60], [61]. For the $(A'_{1-x}A''_x)\text{BO}_3$ perovskite, σ^2 can be computed using the formula [57]:

$$\sigma^2 = x(1 - x)(\Delta_A)^2 \quad (2)$$

Where Δ_A is the difference between the ionic radii of the A' and A'' cations. *Rodriguez-Martinez et al.* have shown that both the ferromagnetic-metal-paramagnetic-insulator transition temperature and the Curie temperature of manganese-based perovskites decreases linearly with the size variance [60], [61].

Similarly, the electronegativity difference between the metal cations and oxygen in perovskite materials can also explain some of the trends observed in their properties. When the oxygen non-stoichiometry of perovskite oxides versus the electronegativity of the B –site cation was plotted, *Liu et al.* obtained an inverted volcano plot [62]. Likewise, *Wang et al.* showed a linear relationship between the metal-oxygen electronegativity difference in lanthanum-based perovskites and the ignition temperature [63]. In addition, *Voorhoeve et al.*, *Murali Dhar et al.* and *Futai et al.* all showed that the catalytic activity of perovskites

increased with decrease in metal-oxygen bond strength or binding energy of surface oxygen [54], [64]–[66].

2.4.3. Applications

Perovskites are also known for their versatile roles. While some perovskites act as metals, some also behave as insulators. Similarly, some perovskite materials are semiconductors and some are superconductors [52]. Perovskites are also applied in the field of ceramics, refractories and electronics [52]. Perovskites oxides have been studied for wastewater treatment applications as well. Experiments have shown that heterogeneous catalysts such as $\text{SrCo}_{1-x}\text{Ti}_x\text{O}_3$ perovskite display good activity and stability for the oxidation of organic contaminants in water [67]. Perovskites have been extensively studied for solid oxide fuel cells [25]. Moreover, recently perovskites have been widely investigated for thermochemical splitting of CO_2 and H_2O for syngas and H_2 production [25]. The redox cycling of perovskites are utilized to perform the thermochemical splitting of CO_2 and H_2O as illustrated in Figure 7 [25], [26], [29], [30]. Reducing agents such as CH_4 or thermal energy can be used in the non-stoichiometric reduction of the ABO_3 perovskite into $\text{ABO}_{3-\delta}$ [21], [26], [29]. Oxidizing agents such as CO_2 or H_2O can then be introduced for the re-oxidation of $\text{ABO}_{3-\delta}$ into ABO_3 and simultaneous production of CO and H_2 [26], [29].

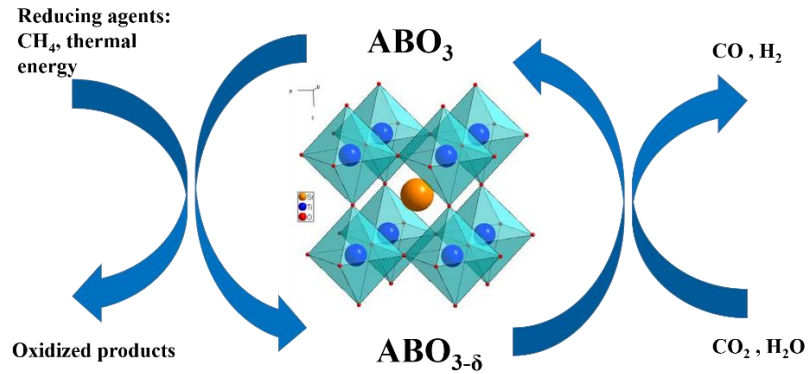


Figure 7. Redox cycle of perovskite ABO_3 [68].

2.4.4. Manganite-Based Perovskites

Manganite-based perovskites have been extensively investigated in a wide range of applications such as magnetic information storage and retrieval, automotive catalysis, solid oxide fuel cells, and thermochemical splitting of CO_2 and H_2O [25], [69], [70]. Manganite-based perovskites owes its versatility to its interesting properties such as excellent magnetotransport features, high electronic conductivity and good chemical activity and stability [25], [26], [29], [69], [70]. In the case of thermochemical splitting of CO_2 , manganite-based perovskites have displayed outstanding chemical activity and good stability [25], [26], [29], [30].

The thermochemical splitting of CO_2 can be achieved by utilizing the redox properties of perovskites [22], [30]. The redox cycling of perovskites can be performed under isothermal conditions or using a temperature-swing approach [32]. At isothermal conditions, the partial pressure of oxidizing agents such O_2 , CO_2 or H_2O can be varied in order to obtain the reduction and oxidation cycles of the perovskites [32]. Most of the thermochemical splitting of CO_2 studies that have been performed utilizes the temperature-swing approach

where the perovskites is reduced at elevated temperatures of 1400 °C and re-oxidized at 1050 °C [26], [29], [30]. However, the temperature-swing method demands solid state heat recovery after the oxidation phase [32]. Studies have shown that isothermal processes eliminates the requirement of solid state heat recovery [32]. Furthermore, *Venstrom et al.* have illustrated that isothermal thermochemical splitting of CO₂ produces CO at rates similar to approaches using temperature-swing [32]. Moreover, *Muhich et al.* have conducted investigations that show that isothermal H₂O splitting produces more H₂ than the temperature-swing H₂O splitting method [33]. *Muhich et al.* further suggest that the frequent heating and cooling of the metal oxides results in a lower overall efficiency of the process as both heat and time is lost [33]. Most of the research work involving thermochemical splitting of CO₂ using perovskites utilizes thermal energy to reduce the perovskites during the redox cycling [26], [29], [30]. However, using reducing agents such as CH₄ can lower the temperature required for reduction of the perovskite [21].

Combining different metals in the A and B –site of manganite-based perovskites have resulted in redox materials displaying excellent thermochemical splitting of CO₂ performances. *Nair et al.* showed that La_{0.5}Sr_{0.5}MnO₃ perovskite synthesized by pechini method displays strong activity and stability for CO production from CO₂ [29]. Similarly, the research work of *Dey et al.* illustrates the exceptional O₂ and CO production capacity of Y_{0.5}Sr_{0.5}MnO₃ perovskite during the redox cycling at relatively lower temperatures [26]. Likewise, the studies performed by *Dey et al.* also shows that La_{0.5}Ca_{0.5}MnO₃ perovskite produces more CO than ceria during the thermochemical splitting of CO₂ [34]. *Ezbiri et al.* have conducted studies with substituting the B –site of La_{1-x}Sr_xMnO₃ perovskite with aluminum [25]. The work of *Ezbiri et al.* reveal that substituting the B –site of La₁₋

$x\text{Sr}_x\text{MnO}_3$ perovskite material with Al enhances the surface with Mn and decreases Sr on the surface [25]. Consequently, both the reduction extent and stability is improved [25]. *Galvez et al.* also mention that substituting the B –site of $\text{La}_{1-x}\text{Sr}_x\text{MnO}_3$ and $\text{La}_{1-x}\text{Ca}_x\text{MnO}_3$ perovskites decreases the formation of CaCO_3 and SrCO_3 formation [71]. $\text{La}_{1-x}\text{Sr}_x\text{Mn}_{1-y}\text{Fe}_y\text{O}_3$ perovskites are attractive materials for solid oxide fuel cells because of its unique electronic and magnetic properties [35]. The Fe content in $\text{La}_{1-x}\text{Sr}_x\text{Mn}_{1-y}\text{Fe}_y\text{O}_3$ perovskites strongly affects its magnetic and transport properties [35]. Also, for H_2 production from H_2O splitting and total oxidation of CH_4 reactions, Fe-based oxygen carriers display great activity [36]. Studies have shown that LaFeO_3 perovskite displays great oxygen mobility and hold a great amount of vacancies in its structure [36]. Similarly, $\text{La}_{1-x}\text{Sr}_x\text{FeO}_3$ perovskites have displayed good stability and repeatability for CH_4 oxidation reactions [36]. Numerous studies have shown that substituting the A and B –site of perovskites with different metals affects its activity for CH_4 oxidation reactions [37].

CHAPTER THREE: EXPERIMENTS AND DISCUSSION

3.1. Experiments

3.1.1. Synthesis

Pechini-type sol-gel method or modified Pechini method was utilized to synthesize the different composition of perovskites. The step-by-step process is displayed in Figure 8. The history of the Pechini method dates to 1967, when Maggio Paul Pechini (1927 – 2007) patented a process to synthesize titanate and niobite dielectrics films [72], [73].

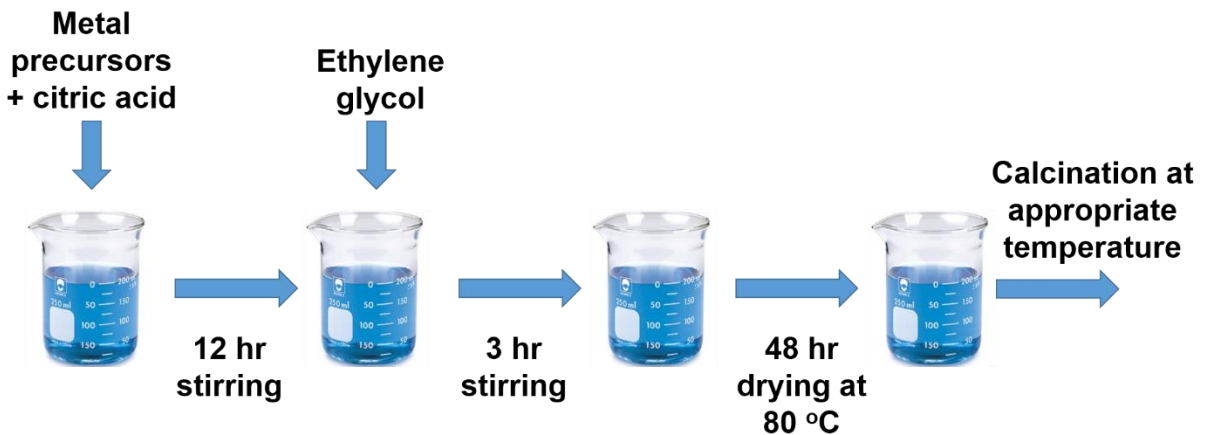


Figure 8. Step-by-step procedure for synthesizing perovskite structured metal oxides using Pechini method [74].

The whole objective of the Pechini-type sol-gel method is to maintain the three-dimensional homogeneity of the multiple metal cations present. Firstly, metal nitrates are used as precursors because they are cheaper, abundant and highly soluble in water [72]. Citric acid is then added to form chelates with the metal cations as illustrated in Figure 9 [73]. The molar ratio of citric acid to metal cation is 1.5:1 [29]. Typically this ratio is between 1 and 3 [72]. To form a three-dimensional network of the metal cations, the metal

chelates that were previously formed had to be combined in all the three directions. For this reason, ethylene glycol was used enabling the process of polyesterification and hence formation of the three-dimensional network of the metal cations as shown in Figure 9 [73]. The molar ratio of citric acid and ethylene glycol used is also 1.5:1 [29]. The aqueous solution then prepared is heated in the oven at 80 °C for 48 hours to remove water and in the process polymeric resin is formed [29], [72], [75]. The dry polymeric resin was grinded well and is then calcined for 2 hours at 1400 °C [29]. Eventually the organic part is removed and pure phase perovskite samples were obtained [29], [72], [75].

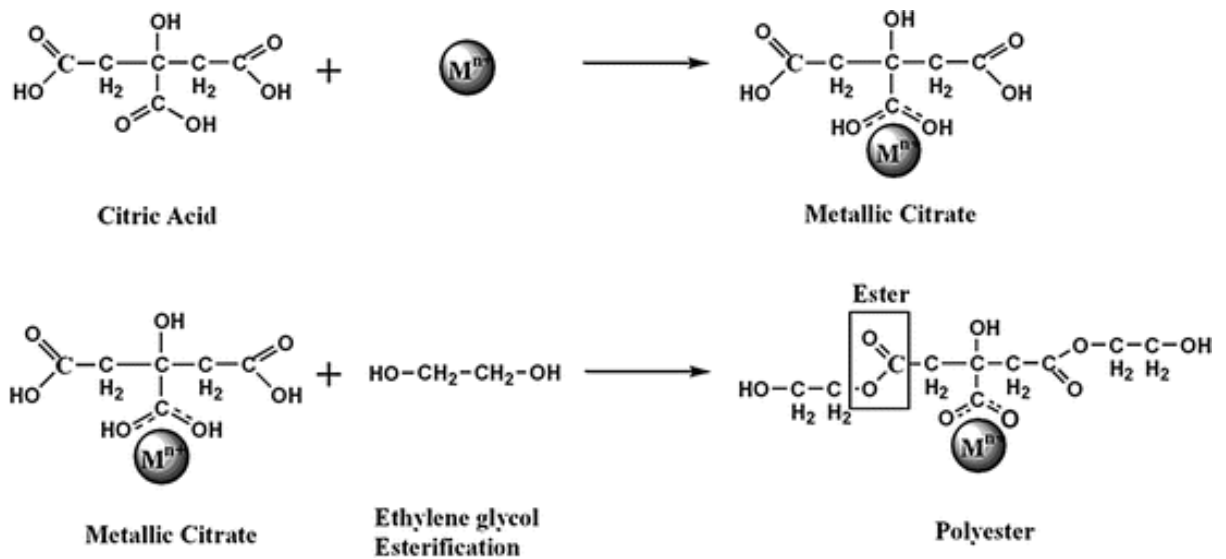


Figure 9. Reaction Schematic of Pechini Method [75].

3.1.2. Characterization

3.1.2.1. X-Ray powder Diffraction (XRD)

The X-Ray powder Diffraction (XRD) was performed using a Rigaku Multiflex instrument with Cu K-alpha as the X-ray source as shown in Figure 10. The Rigaku Multiflex instrument was operated at 40 kV and 40 mA. The values of two-theta between 20 and 80, with degree step of 0.02-degree step and counting time of 2 degree per minute was used for obtaining the XRD profiles.



Figure 10. Rigaku Multiflex System Used for XRD Analysis of the Perovskites Samples Synthesized

3.1.2.2. Scanning Electron Microscope (SEM)

The morphology, particle size, surface structure and surface elemental distribution were investigated using a FEI Quanta 250 FEG field emission scanning electron microscope (FESEM) integrated with energy dispersive spectroscopy (EDS). The FESEM produced high-resolution images of the perovskite samples from magnification of 100× upto 30,000×.

3.1.2.3. Nitrogen Physisorption

To analyze the surface area, pore size and volume of the synthesized perovskite samples a Micromeritics ASAP 2020 Surface Area and Porosity Analyzer was used as shown in Figure 11. The samples were degassed at 150 °C for 3 hours before analysis to remove adsorbed impurities such as water. The specific surface area was evaluated via BET (Brunauer-Emmett-Teller) method. The BET-surface area was calculated by utilizing the section between relative pressures (p/p_0) of 0.05 to 0.2 on the N₂ adsorption isotherm at -196 °C. The pore volume was determined using the Barrett-Joyner-Halenda (BJH) method.



Figure 11. Micromeritics ASAP 2020 Surface Area and Porosity Analyzer.

3.1.2.4. Thermogravimetric Analyzer

To evaluate the carbon dioxide conversion performance of the synthesized perovskite samples an atmospheric thermogravimetric analyzer (TGA), NETZSCH TG 209 F1 Libra (shown in Figure 12), was used. A ramp rate of 20 °C/min was used to reach various temperatures up to 900 °C. About 20 mg of sample was used in all the experiments for consistency. The balance precision of the TGA is 0.0001 mg. The three gases used in all

the experiments were nitrogen, methane and carbon dioxide, which all flowed into the TGA via three different streams.

During the ramping of the temperature from room temperature to either 700, 800 or 900 °C only nitrogen gas flowed in the system at 20 mL/min. Conditions changed once it reached the appropriate temperatures for performing the isothermal redox reactions. Firstly, for reduction methane was introduced at 2 mL/min (15 Vol%) along with nitrogen (18 mL/min) as the reducing agent for 7 minutes. Then the system was purged with pure nitrogen at 20 mL/min for 5 minutes. Eventually, for re-oxidation carbon dioxide at 10 mL/min (50 Vol%) along with nitrogen (10 mL/min) flowed into the TGA for 15 minutes. With that completed one redox cycle. The same program was used to perform experiments with three redox cycles and ten redox cycles. The sample weight and temperature were measured and recorded for future analyses purposes.



Figure 12. NETZSCH (TG 209 F1 Libra) TGA Used to Evaluate the CO₂ Conversion Performance.

3.2. Results and Discussion

3.2.1. A-site Substitution and Effect of temperature

Once the perovskite samples were prepared by Pechini method, XRD analyses were performed in order to verify the phase purity. Figure 13 shows the XRD profile of the different samples synthesized. Except for $\text{La}_{0.5}\text{Ba}_{0.5}\text{MnO}_3$ (LBM) and $\text{La}_{0.5}\text{Sr}_{0.5}\text{Mn}_{0.5}\text{Ni}_{0.5}\text{O}_3$ (LSMN), the rest of the samples displayed pure phase. Similarly, melting problem was observed when calcining the sample $\text{La}_{0.5}\text{Sr}_{0.5}\text{Mn}_{0.5}\text{Co}_{0.5}\text{O}_3$ (LSMC) both at 1200 and 1400 °C.

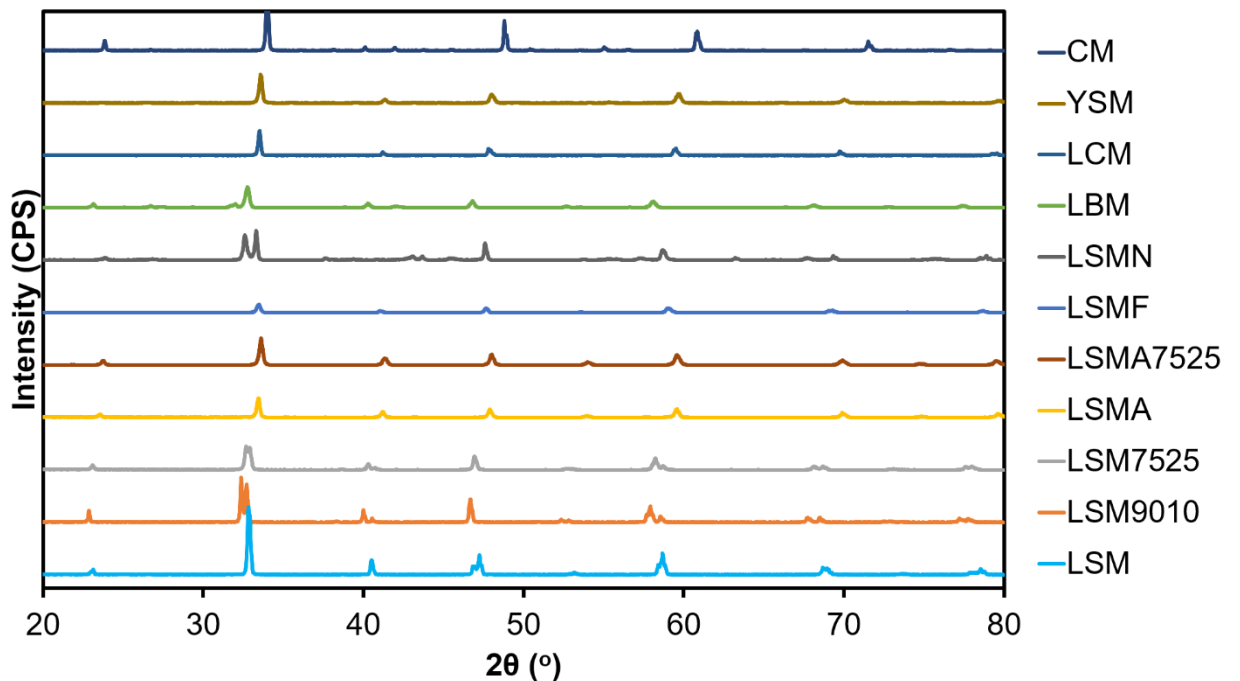


Figure 13. XRD pattern for the various samples synthesized

Initially the redox performances of the samples CaMnO_3 (CM), $\text{La}_{0.5}\text{Ca}_{0.5}\text{MnO}_3$ (LCM), $\text{La}_{0.5}\text{Sr}_{0.5}\text{MnO}_3$ (LSM) and $\text{Y}_{0.5}\text{Sr}_{0.5}\text{MnO}_3$ (YSM) with varying A -site composition and the same B -site composition were tested in the TGA for three cycles. The redox reactions were

performed at 700, 800 and 900 °C and the results are illustrated in Figure 14, Figure 15 and Figure 16. At all the temperatures, CM has the greatest reduction extent in the first cycle. The reduction extent (R_{ext}) of the samples were calculated using the formula:

$$R_{ext} = \frac{\Delta m_{red}}{m_s} = \frac{m_{i,red} - m_{f,red}}{m_s} \quad (3)$$

Where, Δm_{red} is the change in mass of the perovskite sample after the completion of the reduction phase, m_s is the original mass of the perovskite sample, $m_{i,red}$ is the mass of the perovskite sample at the onset of the reduction phase and $m_{f,red}$ is the mass of the perovskite sample at the completion of the reduction phase. Reduction extent is the mass of monoatomic oxygen released per unit mass of the perovskite sample.

The redox active site in all the three samples is Mn [25], [76]. Also, it is known that Mn in the state Mn^{4+} is more easily reducible than in Mn^{3+} [30]. The oxidation state of Mn in CM is +4 which is higher than in LCM (3.5+), LSM (3.5+) and YSM (+3.5). Thus, CM is reduced the most during the first redox cycle. However, it displays the most unstable behavior amongst the three as shown in Figure 14, Figure 15 and Figure 16. At 900 °C, CM does not even get re-oxidized in the first cycle. Alkaline earth metals such as Ca and Sr can form carbonates when exposed to CO_2 [71]. Studies have shown that $La_{1-x}Ca_xMnO_3$ perovskites with $x > 0.6$ have the tendency to form calcium carbonates [37]. In our investigation, for CM $x = 1$. After the three redox cycles for CM, the color of the sample changed from black to light grey or white, indicating the formation of carbonate species.

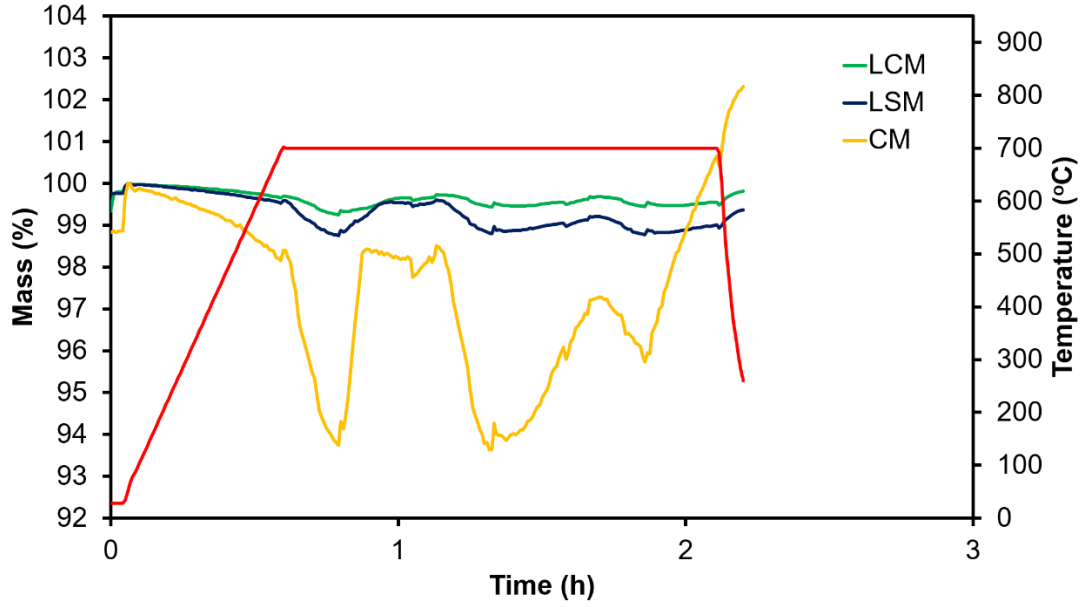


Figure 14. Three redox cycle performances of CM, LCM and LSM at 700 °C

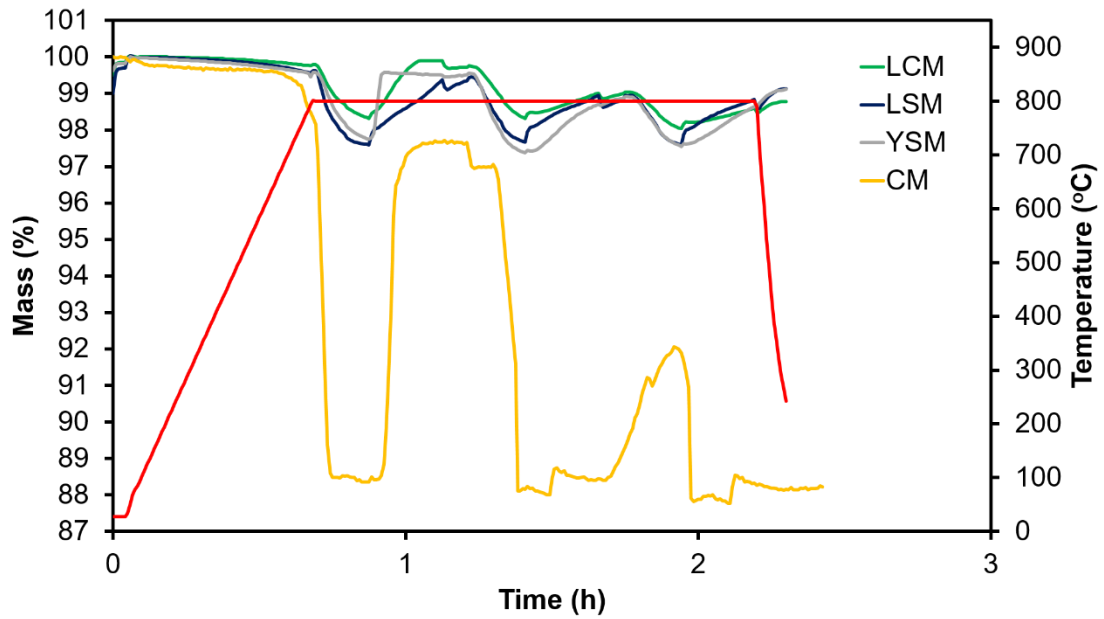


Figure 15. Three cycle redox performance of CM, LCM, LSM and YSM at 800 °C

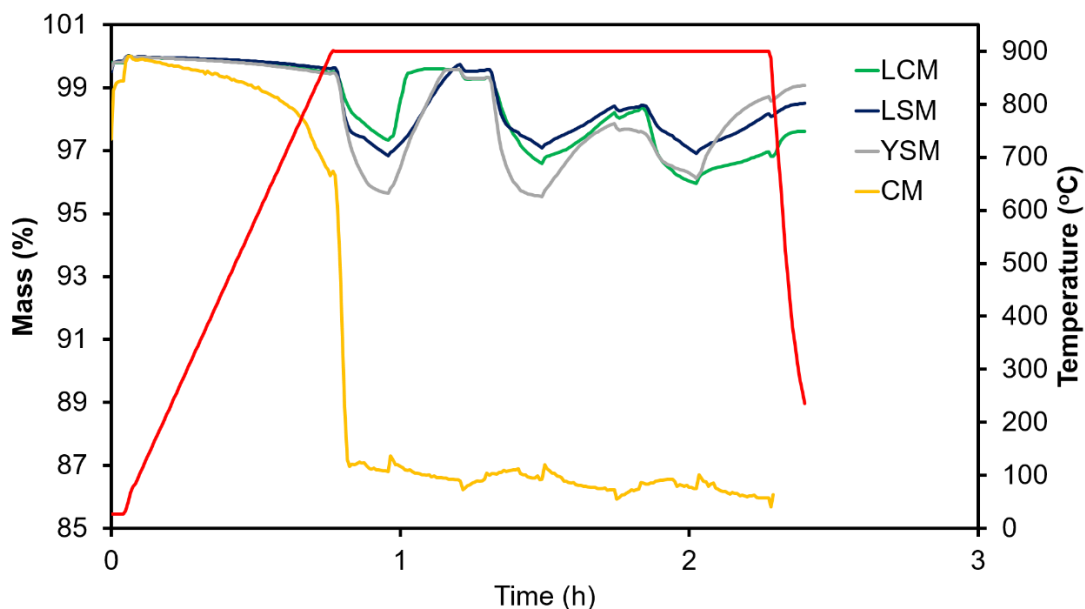


Figure 16. Three cycle redox performance of CM, LCM, LSM and YSM at 900 °C

The effect of temperature on the activity of the perovskite samples were also investigated. For all the samples CM, LCM, LSM and YSM the reduction extent increased with temperature as illustrated in Figure 17. Since the reduction reactions of perovskites are endothermic in nature, thermodynamically reduction is favored at higher temperatures. The greatest reduction extent is observed at 900 °C. Therefore, all the reactions henceforth were performed at 800 and 900 °C. From Figure 17 it is evident that choosing a perovskite catalyst having a redox active site with a higher oxidation state can reduce the operating temperature. Nevertheless, it is also vital to investigate the ability of the metals in the perovskite to resist carbonate formation. In our investigation CM is a prime example of a catalyst displaying greater activity but poor stability.

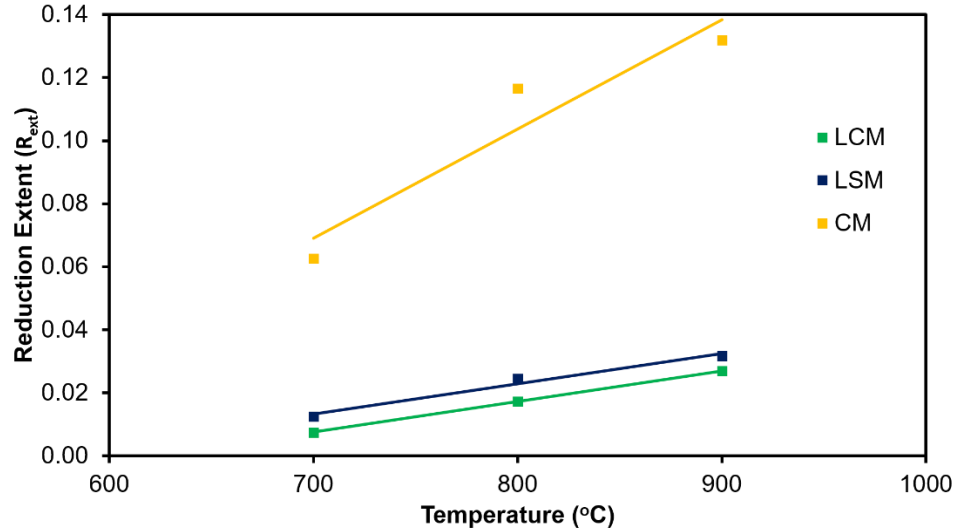


Figure 17. Reduction extent as a function of temperature for CM, LCM and LSM

At 700, 800 and 900 °C, CM displays superior activity during the first cycle compared to LCM, LSM and YSM as observed in Figure 14, Figure 15, Figure 16 and Figure 17. At 900 °C, CM produces $4122 \mu\text{molg}^{-1} \text{O}_2$ corresponding to the largest reduction extent as shown in Figure 18. Since there was no re-oxidation in the first cycle for CM at 900 °C, the CO production was zero. Amongst LCM, LSM and YSM, it is clear from Figure 14, Figure 15, Figure 16 and Figure 17 that YSM displays the greatest activity, followed by LSM and then LCM. At 900 °C YSM, LSM and LCM produce 1362 , 992 and $840 \mu\text{molg}^{-1} \text{O}_2$ respectively during the reduction step of the first cycle. Similarly, YSM, LSM and LCM produce 2458 , 1813 and $1422 \mu\text{molg}^{-1} \text{CO}$ respectively during the re-oxidation step of the first cycle at 900 °C. Numerous studies have shown that the properties of manganite based perovskites are altered as a result of the disorder in the structure caused by cation size mismatch in the A –site [57], [60], [61]. Size variance (σ^2) or variance of the A –site cation radii distribution is a parameter that measures the disparity in the radii of the A –site cations. Since the difference between the ionic radii of Y (0.119 nm) and Sr (0.144 nm) is greater than that of La (0.136 nm) and Sr as well as La and Ca (0.134 nm), YSM has the

largest σ^2 value of 159 pm² followed by LSM (16 pm²) and then LCM (1 pm²). The A – site cation radii mismatch primarily displaces the oxide ions from their average crystallographic positions randomly, thus altering their properties [60]. Therefore, as illustrated in Figure 19 a trend is observed in the values of reduction extent as the size variance increases. YSM having the largest σ^2 value displays the greatest reduction extent followed by LSM and then by LCM. Size variance (σ^2) will be discussed in more details in section 4.2 of this thesis.

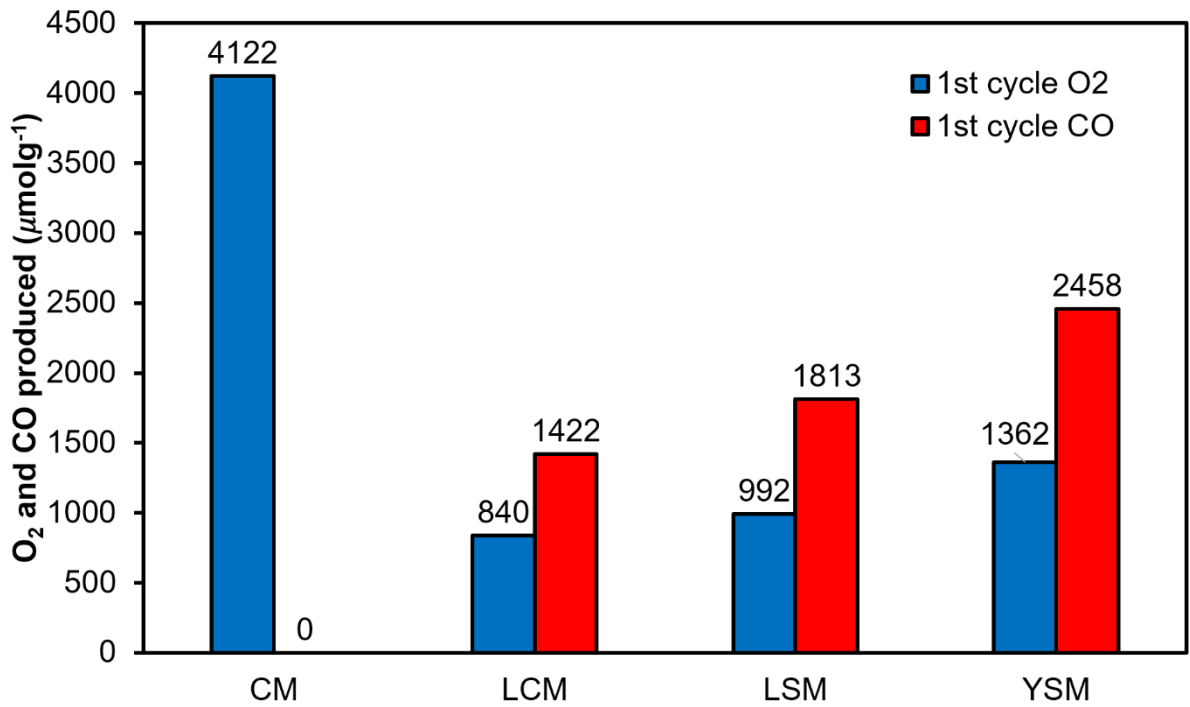


Figure 18. O₂ and CO production during the first redox cycle at 900 °C for CM, LCM, LSM and YSM.

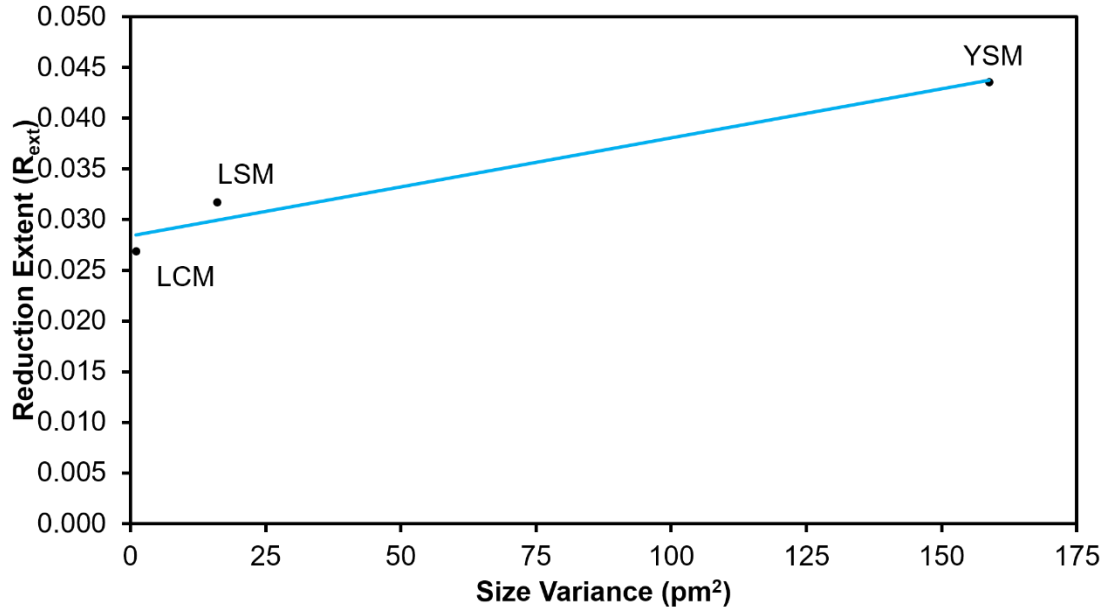


Figure 19. Reduction extent as a function of size variance.

In terms of activity, YSM displayed better performance than LSM. However, XRD analysis after three redox cycles showed formation of carbonate phases (SrCO_3) only in the case of YSM (Figure 20). LSM did not show any SrCO_3 peaks after the three redox cycles as observed in Figure 20.

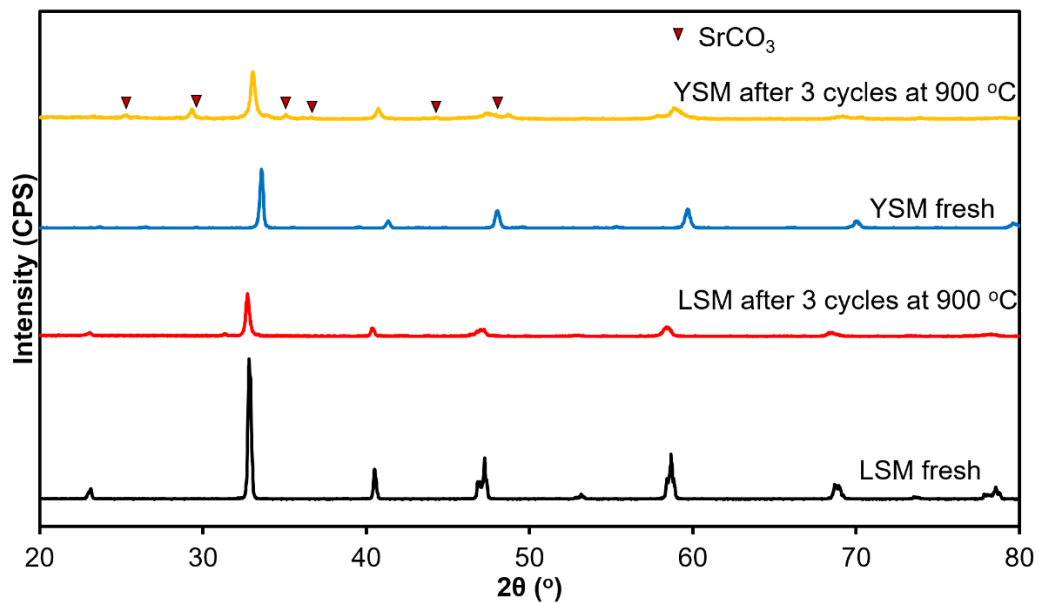


Figure 20. XRD profiles of YSM and LSM before and after three redox cycles at 900 °C.

Figure 21 provides a clearer view of the SrCO_3 peaks in the case of YSM after the three redox cycles at $900\text{ }^\circ\text{C}$. *Steinfeld et al.* showed that there is correlation between the metal-oxygen bond strength in a perovskite and its resistance to carbonate formation [22]. Greater the metal-oxygen bond strength, the more resistant the perovskite is to carbonate formation [22]. The larger metal-oxygen bond strength of LSM than YSM might be one of the reasons for the greater resistance against SrCO_3 formation for LSM than YSM. The metal-oxygen bond strength and its relationship with activity will be discussed in section 4.4 of this thesis.

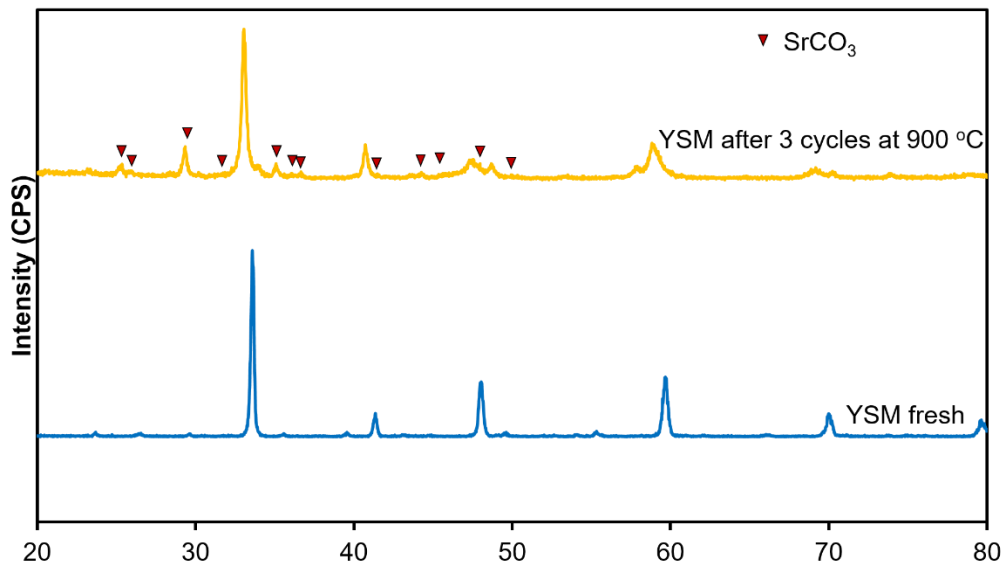


Figure 21. XRD profile of fresh YSM and YSM after 3 redox cycles at $900\text{ }^\circ\text{C}$.

Therefore, out of the four samples (CM, LCM, LSM and YSM) that were initially investigated, LSM displayed the optimal performance based on its good activity and resistance to carbonate formation. Due to this reason, the family of $\text{La}_{1-x}\text{Sr}_x\text{MnO}_3$ was further investigated to find an optimal A –site composition by varying the Sr content ($x = 0.5, 0.25, 0.10$).

3.2.2. Optimal A-site Composition

Three samples $\text{La}_{0.5}\text{Sr}_{0.5}\text{MnO}_3$ (LSM), $\text{La}_{0.75}\text{Sr}_{0.25}\text{MnO}_3$ (LSM7525) and $\text{La}_{0.90}\text{Sr}_{0.10}\text{MnO}_3$ (LSM9010) belonging to the $\text{La}_{1-x}\text{Sr}_x\text{MnO}_3$ perovskite family were synthesized via Pechini method and were all calcined at 1400°C . The XRD profile of these samples are illustrated in Figure 13, but a clearer comparison of the XRD profile between these three samples are shown in Figure 22. As evident in Figure 22, increasing the Sr^{2+} content in the $\text{La}_{1-x}\text{Sr}_x\text{MnO}_3$ perovskite results in the shifting of the Bragg peaks towards higher angles. A similar shift in the peaks with increase in the Sr^{2+} were observed by *Steinfeld et al.* and *Abanades et al* [30], [71]. SEM results shown in Figure 23 conveys that higher Sr^{2+} content in $\text{La}_{1-x}\text{Sr}_x\text{MnO}_3$ results in smaller crystallite or grain size. Studies conducted by *Haile et al.* have also shown $\text{La}_{1-x}\text{Sr}_x\text{MnO}_3$ perovskites with higher Sr^{2+} content yield smaller grain size [77].

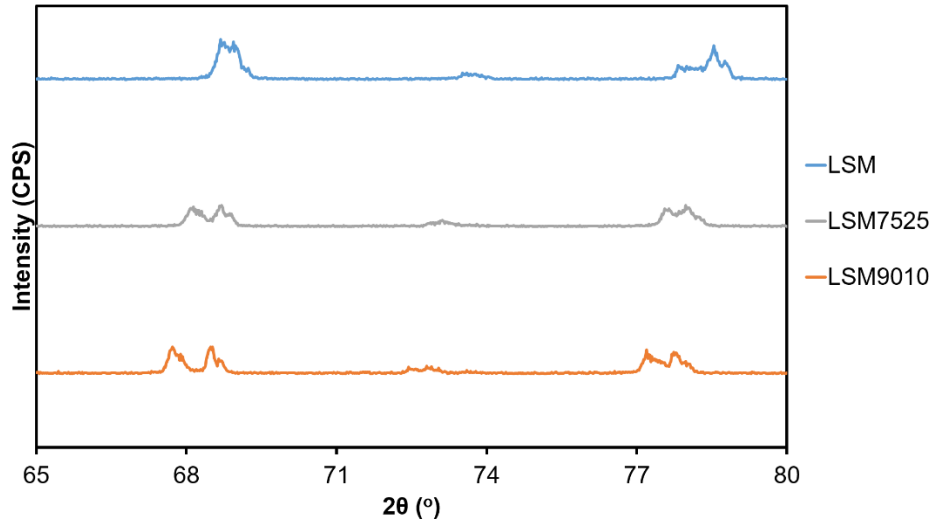


Figure 22. XRD profile of the $\text{La}_{1-x}\text{Sr}_x\text{MnO}_3$ family with $x = 0.5$ (LSM), $x = 0.25$ (LSM7525) and $x = 0.10$ (LSM9010) after calcination at 1400°C .

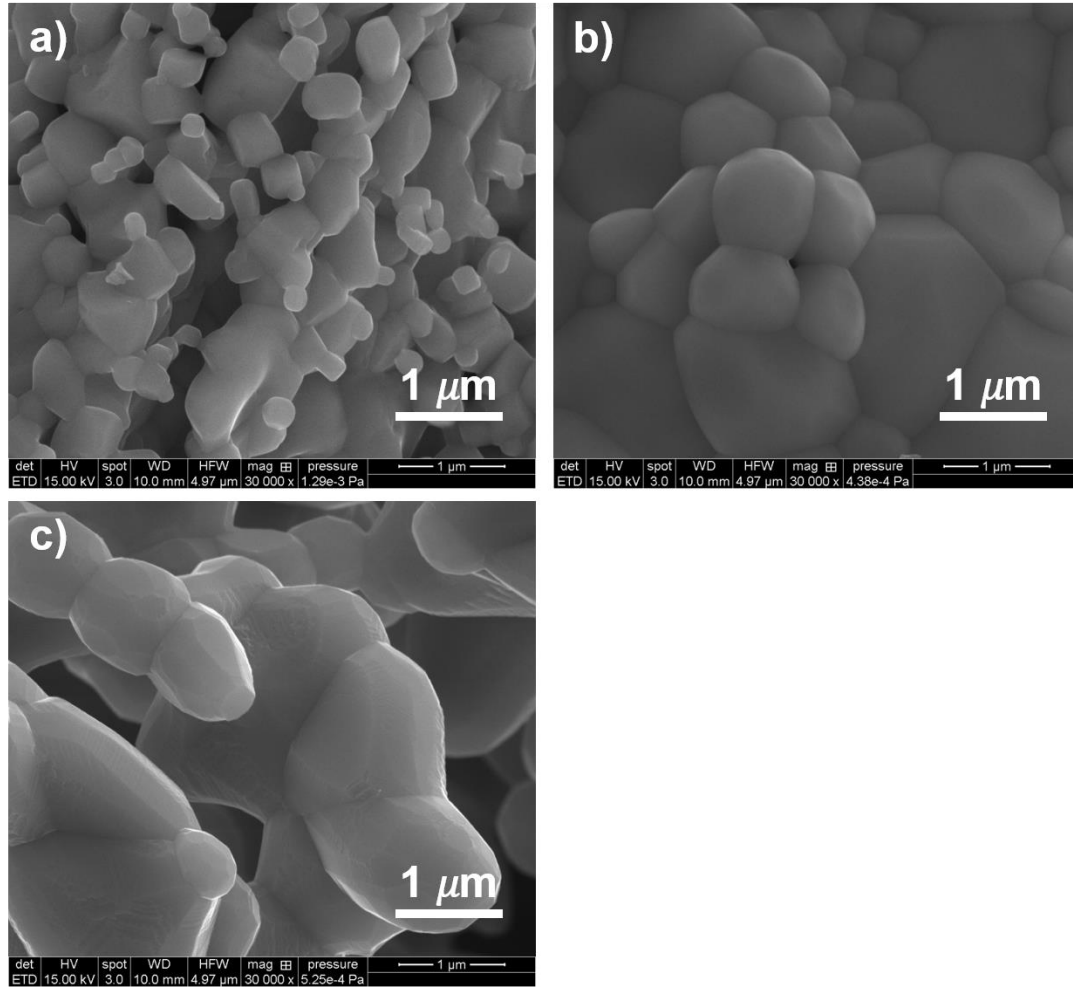


Figure 23. SEM images 30000 × magnification for a) LSM fresh b) LSM7525 fresh and c) LSM9010 fresh

The textural properties of LSM, LSM7525 and LSM9010 such as specific surface area, pore volume and pore size were also investigated using a Micromeritics ASAP 2020 Surface Area and Porosity Analyzer. The analyzer utilizes nitrogen adsorption at its normal boiling point of $-196\text{ }^{\circ}\text{C}$ or 77 K [78]–[80]. The nitrogen adsorption isotherms obtained at $-196\text{ }^{\circ}\text{C}$ for LSM, LSM7525 and LSM9010 are illustrated in Figure 24. All the three isotherms corresponds most closely to Type II isotherm as outlined by the International Union of Pure and Applied Chemistry (IUPAC) [81], [82]. Type II isotherms are produced by the physisorption of gases such as N_2 on non-porous or macroporous materials. The

gradual curvature of all the three isotherms at lower values of relative pressure as observed in Figure 24 indicates the significant co-occurrences of the monolayer formation and the inception of the multilayer adsorption [81]. As the value of the relative pressure (p/p_0) approaches 1, the volume adsorbed increases sharply for LSM, LSM7525 and LSM9010. This is another characteristic of Type II isotherm [81]. For non-porous and macroporous materials the adsorption and desorption isotherm overlap with each other forming no hysteresis loop. In the case of LSM7525 the adsorption and desorption isotherms overlapped with each other as illustrated in Figure 24. However, hysteresis loops were observed in the case of LSM and LSM9010. Moreover, the hysteresis loop associated to LSM is more pronounced than that related to LSM9010. Nevertheless, both the hysteresis loop in the case of LSM and LSM9010 corresponds to the Type H3 hysteresis loop as classified by IUPAC [81], [83]. Type H3 hysteresis loops are produced by adsorbents with macropores that are not entirely filled with pore condensate [81]. Plate-like particles can combine together to form non-rigid clusters. These clusters can also produce the Type H3 hysteresis loop [81].

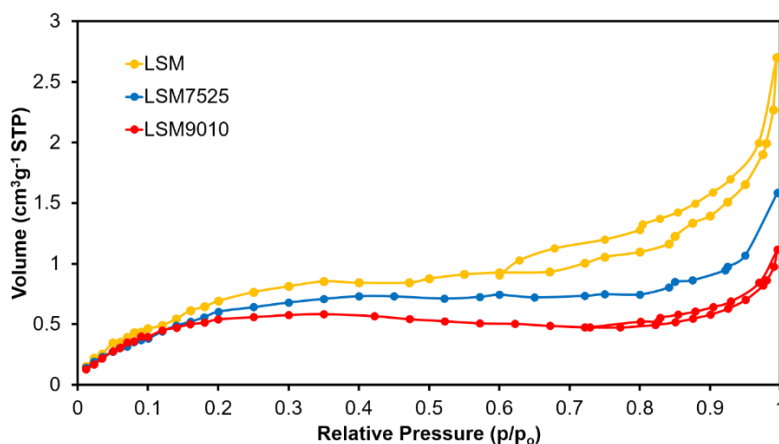


Figure 24. N_2 adsorption isotherms for LSM, LSM7525 and LSM9010.

The total pore volume of the samples were evaluated from the volume of N₂ adsorbed at 0.995 relative pressure (p/p₀) [84]. At values of p/p₀ very close to 1, such as 0.995, it is assumed that all the accessible pores are occupied by N₂. From Figure 24 it is clear that the greatest amount of N₂ is absorbed onto LSM and the least amount of N₂ is absorbed onto LSM9010. Thus, LSM has the highest pore volume of 0.004177 cm³g⁻¹ and LSM9010 has the least pore volume of 0.001731 cm³g⁻¹. The pore volume values are summarized in Table 1. From the results it seems that the pore volume increases with the strontium content.

Table 1. Textural properties of fresh LSM, fresh LSM7525 and fresh LSM9010.

Sample	BET Surface Area (m²g⁻¹)	Pore Volume (cm³g⁻¹)	Pore Size (nm)
LSM fresh	2.9865 ± 0.1218	0.004177	8.87
LSM7525 fresh	2.7385 ± 0.0883	0.002450	6.87
LSM9010 fresh	2.2727 ± 0.0474	0.001731	7.41

The specific surface area was determined using the Brunauer-Emmett-Teller (BET) method [85]. The BET method utilizes the section of the N₂ adsorption isotherm between relative pressure values of 0.05 and 0.2 [79], [86], [87]. The BET surface area values of LSM, LSM7525 and LSM9010 are listed in Table 1. Synthesis method and calcination temperature affect the surface area of the synthesized perovskite sample [54]. All the three samples (LSM, LSM7525 and LSM9010) were prepared via the same Pechini method and calcined at 1400 °C. Consequently, fresh LSM, fresh LSM7525 and fresh LSM9010 have very similar BET surface area values. Nevertheless, if the BET surface area values are compared to the first, second, third or fourth decimal place, then fresh LSM has the greatest

surface area of $2.9865 \text{ m}^2\text{g}^{-1}$ and LSM9010 has the least surface area of $2.2727 \text{ m}^2\text{g}^{-1}$. The low BET surface area values of these three samples can be attributed to the high calcination temperature of $1400 \text{ }^\circ\text{C}$ [54].

The pore sizes are determined using the Barrett-Joyner-Halenda (BJH) method [85]. The pore size values of fresh LSM, fresh LSM7525 and fresh LSM9010 are outlined in Table 1. Fresh LSM, fresh LSM7525 and fresh LSM9010 have pore sizes of 8.87, 6.87 and 7.41 nm respectively. In contrast to the BET surface area and pore volume, there is not a clear trend in the pore size with respect to the strontium content.

The redox performances of LSM, LSM7525 and LSM9010 were investigated for three cycles at 800 and 900 $^\circ\text{C}$ in the TGA. The TGA profiles at 800 and 900 $^\circ\text{C}$ are displayed in Figure 25 and Figure 26 respectively. It is evident from the TGA profiles that LSM is reduced the most at both the temperatures whereas LSM9010 is reduced the least. The oxidation states of the redox active site, Mn, in LSM, LSM7525 and LSM9010 are +3.5, +3.25 and +3.10 respectively. More Sr^{2+} content in the $\text{La}_{1-x}\text{Sr}_x\text{MnO}_3$ perovskite leads to an increase in concentration of Mn^{4+} . Consequently, amongst LSM, LSM7525 and LSM9010, LSM has the greatest Mn^{4+} concentration and least Mn^{3+} concentration. Whereas LSM9010 has the least Mn^{4+} concentration and highest Mn^{3+} concentration. Since Mn^{4+} is easily reduced than Mn^{3+} , LSM displays the best reduction performance.

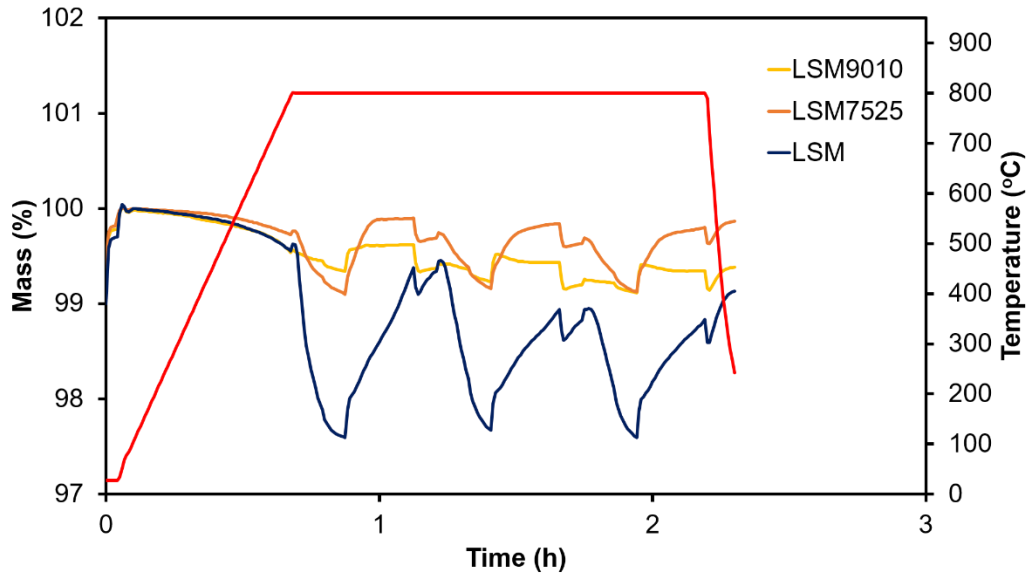


Figure 25. TGA profile of LSM, LSM7525 and LSM9010 at 800 °C.

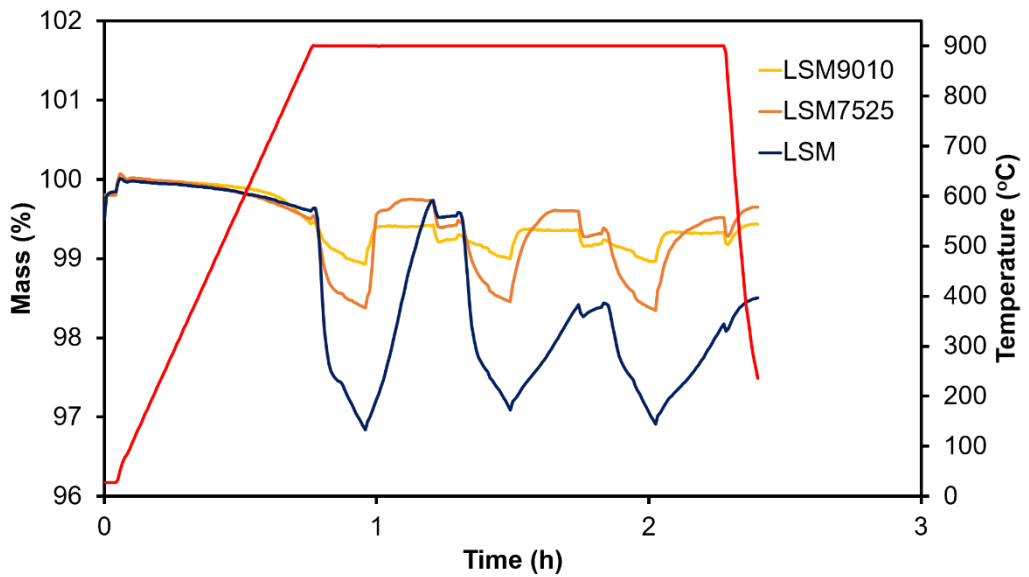


Figure 26. TGA profile of LSM, LSM7525 and LSM9010 at 900 °C.

Since LSM has the greatest reduction extent, it produces the highest amount of O₂ and corresponding CO gas during all three redox cycles at both 800 and 900 °C as illustrated in Figure 27 and Figure 28. At 800 °C, during the first redox cycle LSM, LSM7525 and LSM9010 produce 765, 282 and 212 μmolg^{-1} O₂ respectively. Corresponding to the O₂

evolved, LSM, LSM7525 and LSM9010 produce 1164, 499 and 176 μmolg^{-1} CO respectively during the first redox cycle at 800 °C. As mentioned previously, higher temperature favors the reduction of the perovskite, therefore at 900 °C LSM, LSM7525 and LSM9010 produce more O₂ and CO than at 800 °C. At 900 °C, during the first redox cycle LSM, LSM7525 and LSM9010 produce 992, 529 and 337 μmolg^{-1} O₂ respectively. Similarly, in the first cycle at 900 °C, LSM, LSM7525 and LSM9010 produce 1813, 857 and 307 μmolg^{-1} CO respectively. It is evident from both Figure 27 and Figure 28 the activity of all the samples LSM, LSM7525 and LSM9010 decreases after the first redox cycle at both 800 and 900 °C. But after the first redox cycles, the activity remains similar during the second and third redox cycles for all the three samples.

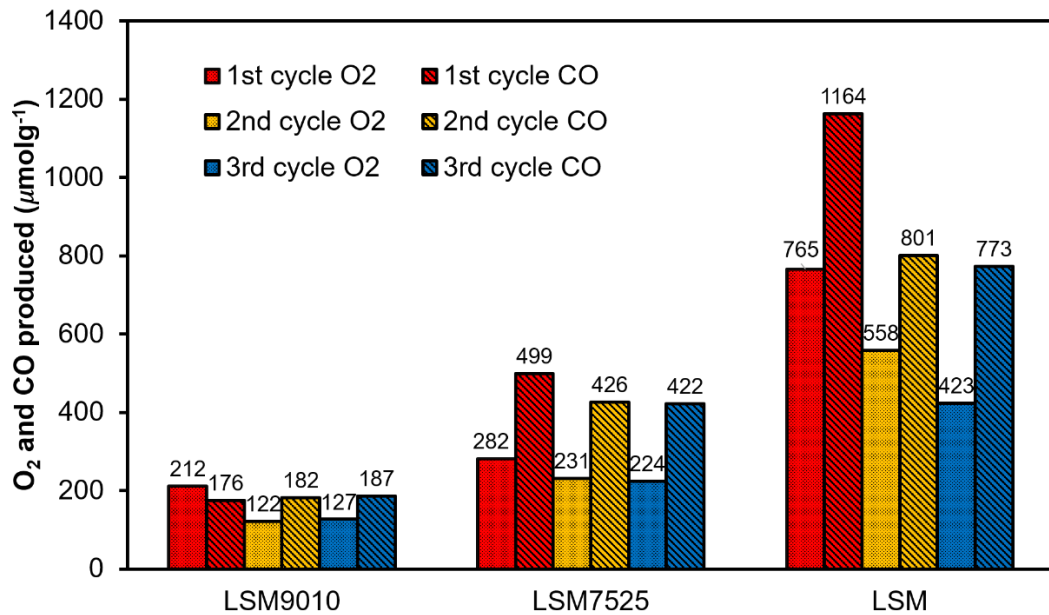


Figure 27. O₂ and CO production for LSM, LSM7525 and LSM9010 at 800 °C.

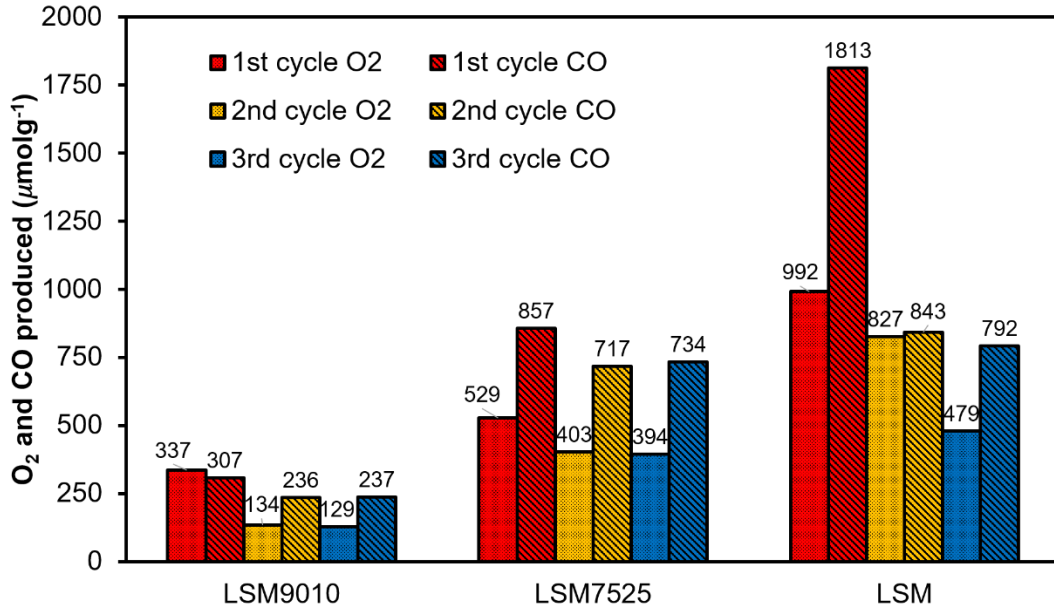


Figure 28. O₂ and CO production for LSM, LSM7525 and LSM9010 at 900 °C.

A kinetic study regarding the performance of LSM, LSM7525 and LSM9010 was then conducted to evaluate parameters such as activation energy. According to the research work conducted by *Fierro et al.* the reduction of perovskite can be analyzed using the contracting-sphere or shrinking grain model [54]. Initially the rate of reduction is rapid and slowly decreases due to mass-transfer limitation.

The solid-state reaction is governed by the equation [88], [89]:

$$\frac{dX}{dt} = A_r e^{\frac{-E_a}{RT}} f(X) \quad (4)$$

Where, t is the time, A_r is the pre-exponential factor, E_a is the activation energy, R is the universal gas constant, T is the temperature, X is the conversion fraction and $f(X)$ is the reaction model which is the function of X . X can be computed using the equation:

$$X = \frac{m_0 - m_t}{m_0 - m_f} \quad (5)$$

Where, m_0 is the mass of the perovskite sample before reduction, m_t is the mass at time t and m_f is the final mass after reduction. For a contracting-sphere or volume model $f(X)$ is evaluated as [88]:

$$f(X) = 3(1 - X)^{2/3} \quad (6)$$

In equation 1, the term $A_r e^{\frac{-E_a}{RT}}$ is the intrinsic surface reaction rate (r).

Thus, by substituting equation 6 in 4, we obtain:

$$\frac{dX}{dt} = 3r(1 - X)^{2/3} \quad (7)$$

Integrating the differential equation 7 from $t = 0$ to $t = t$, we get:

$$1 - (1 - X)^{\frac{1}{3}} = rt \quad (8)$$

Equation 8 is a form of Mampel's law for a three-dimensional shrinking grain model. When the reaction is under kinetic control, according to equation 8, the plot of $1 - (1 - X)^{\frac{1}{3}}$ versus t should produce a straight line with slope having the value of the intrinsic surface reaction rate (r). The linear section observed in the plot of $1 - (1 - X)^{\frac{1}{3}}$ versus t during the initial phase of reduction corresponds to the kinetically controlled region as illustrated in Figure 29. When identifying the linear section in the plot it is vital that the region falls during the very start of the reduction phase and has a maximum slope value. This maximum slope value is the intrinsic surface reaction rate (r). In the case of reduction of LSM9010 at 800 °C the slope of the linear section or the value of r is 0.0016 s^{-1} . The kinetic-controlled region is succeeded by the part governed by both mass-transfer and surface reactions. Thus, as time proceeds the reaction rate slows down, indicated by the decreasing slope of the tangent

to the plot of $1 - (1 - X)^{\frac{1}{3}}$ versus t. The maximum slope value of the kinetic-controlled region or the intrinsic surface reaction rate (r) is also the true intrinsic surface reaction rate when conversion fraction (X) is zero. Thus,

$$r_0 = r$$

Where, r_0 is the intrinsic surface reaction rate when $X = 0$.

From equation 4, 6 and 7:

$$r_0 = A_r e^{\frac{-E_a}{RT}} \quad (9)$$

Taking the natural logarithm of both sides in equation 9, we get:

$$\ln(r_0) = \frac{-E_a}{R} \left(\frac{1}{T} \right) + \ln A_r \quad (10)$$

Therefore, the slope of the plot of $\ln(r_0)$ versus $(1/T)$ would provide the activation energy.

Thus, the r_0 values of the samples LSM, LSM7525 and LSM9010 were computed at different temperatures using the plot of $1 - (1 - X)^{\frac{1}{3}}$ versus t as shown in Figure 29.

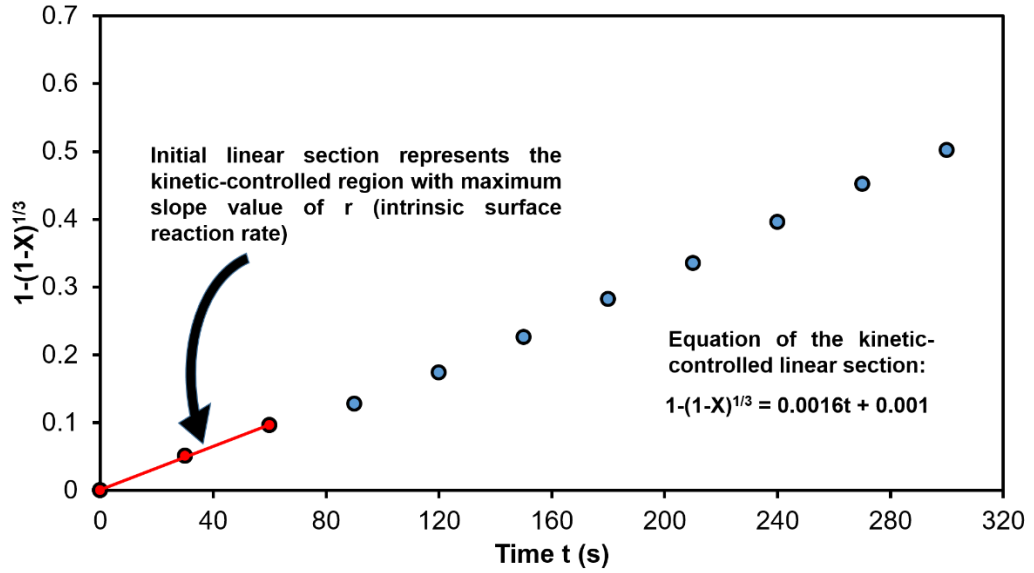


Figure 29. $1-(1-X)^{1/3}$ versus time for LSM9010 at 800 °C with 15 Vol% CH_4 during reduction.

Once the r_0 values were obtained for the samples, $\ln(r_0)$ versus $(1/T)$ was plotted as shown in Figure 30, Figure 31 and Figure 32. The activation energies are then evaluated by multiplying the absolute value of the slope of the linear fit and the universal gas constant.

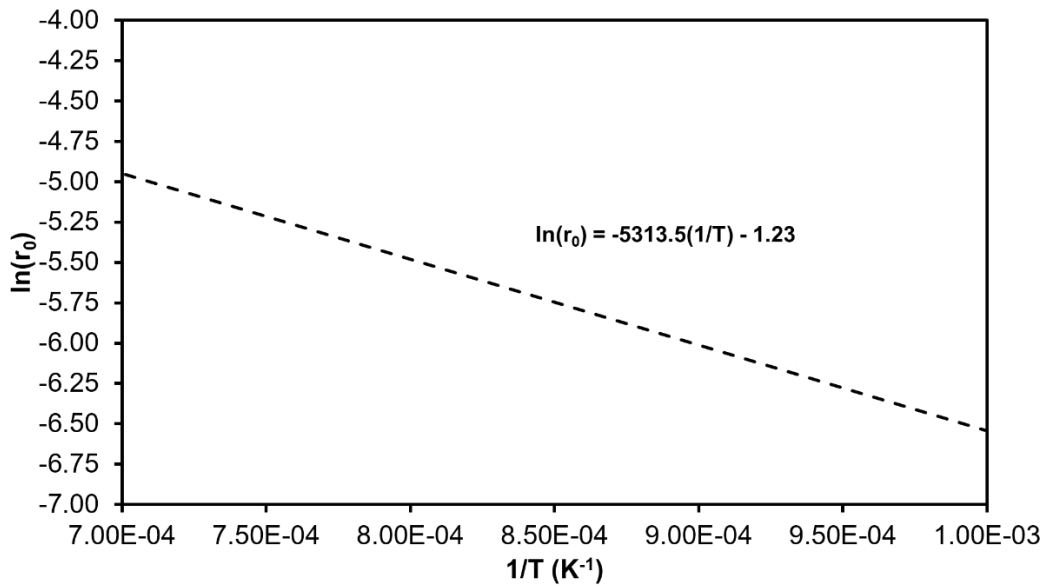


Figure 30. $\ln(r_0)$ versus $(1/T)$ for LSM.

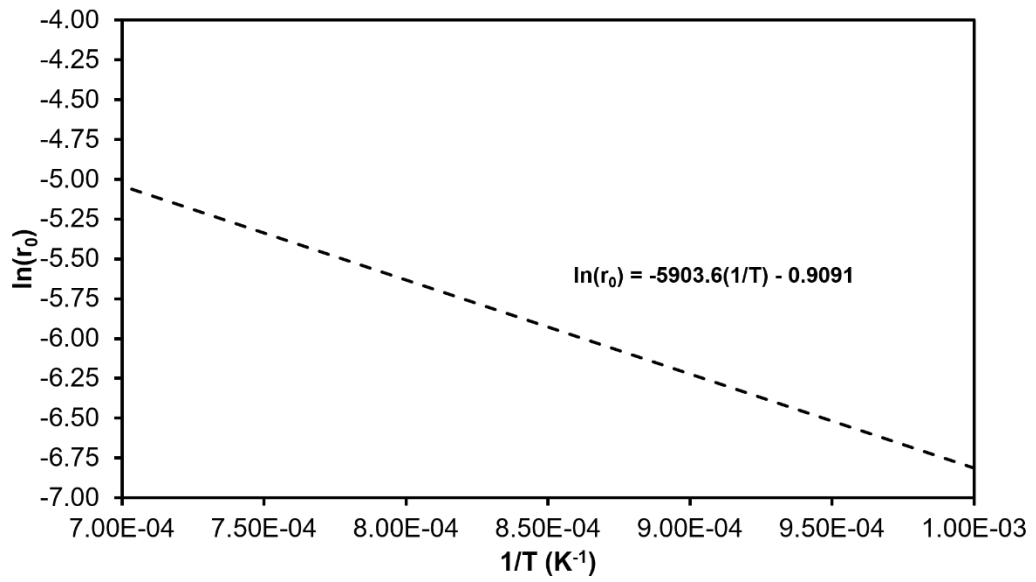


Figure 31. $\ln(r_0)$ versus $(1/T)$ for LSM7525.

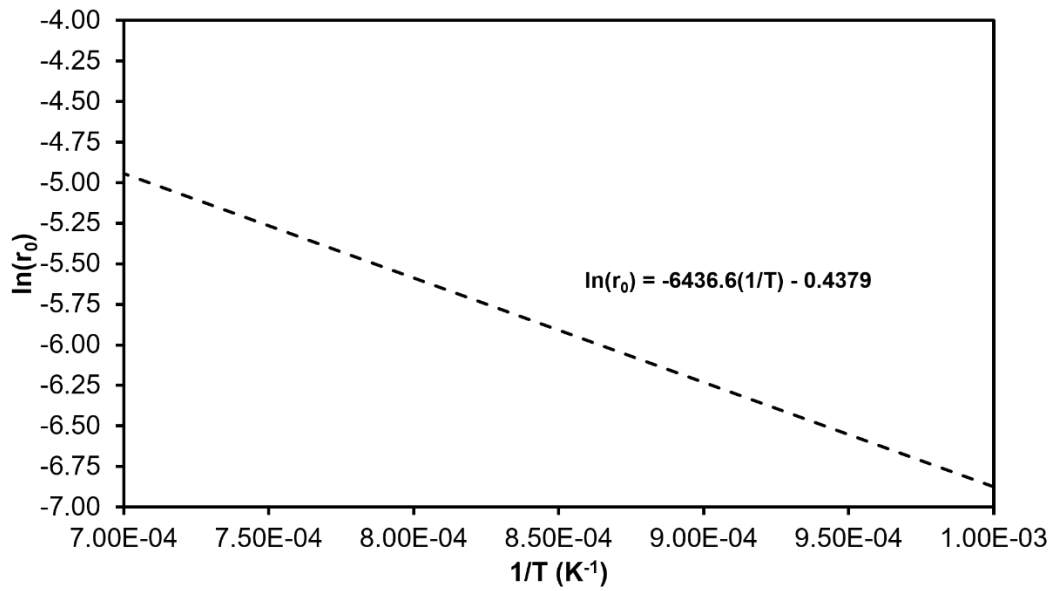


Figure 32. $\ln(r_0)$ versus $(1/T)$ for LSM9010.

The activation energies of LSM, LSM7525 and LSM9010 were computed and are illustrated in Figure 33. LSM has the lowest activation energy of 44 kJmol⁻¹ and LSM9010 has the highest activation energy of 54 kJmol⁻¹. It is clearly evident that as the Sr²⁺ content in the La_{1-x}Sr_xMnO₃ perovskite family increases the activation energy for reduction decreases. Similar trend was observed by Abanades et al [30]. It has previously been mentioned that the concentration of Mn⁴⁺ increases and the concentration of Mn³⁺ decreases as Sr²⁺ content in La_{1-x}Sr_xMnO₃ perovskite increases. Moreover, Mn⁴⁺ is easily reducible than Mn³⁺. Thus, LSM has the best reduction performance, followed by LSM7525 and then by LSM9010. The accuracy of our activation energy calculations would have improved if reduction experiments were performed at more temperature values.

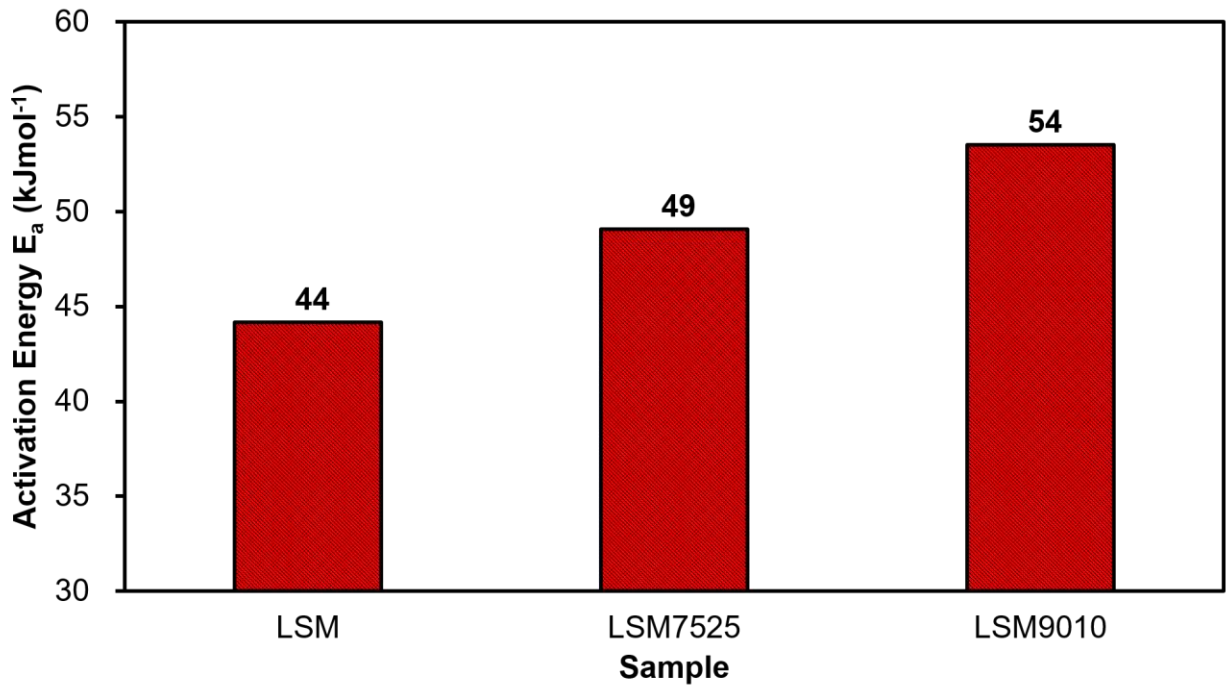


Figure 33. Activation energies calculated for LSM, LSM7525 and LSM9010.

The performances of LSM, LSM7525 and LSM9010 are further analyzed on the basis of size variance (σ^2) as it was done for YSM, LSM and LCM. Since LSM has 50% La (0.136

nm) and 50% Sr (0.144 nm), LSM has greater disparity in the radii of the A –site cations than LSM7525 and LSM9010. Similarly, LSM9010 has the least disparity in the radii of the A –site cations amongst LSM, LSM7525 and LSM9010. LSM, LSM7525 and LSM9010 have size variance (σ^2) values of 16.00, 12.00 and 5.76 pm² respectively. This mismatch in the radii of the A –site cations displaces the oxide ions from their average crystallographic position randomly as mentioned previously. Ultimately, differences in the size variances generates perovskites with differing properties. According to Figure 34, reduction extent increases with size variance for the La_{1-x}Sr_xMnO₃ perovskite family with x = 0.10, 0.25 and 0.50. LSM with the largest σ^2 is reduced the greatest and LSM9010 with the lowest σ^2 is reduced the least. A similar trend was observed for YSM, LSM and LCM. Although the trend displayed in Figure 34 suggests that there could be relationship between σ^2 and the reduction extent of the perovskite, the effect of σ^2 on the reduction extent should not be viewed under isolation. Factors such as the concentration of redox active species Mn and its oxidation state, tolerance factor and metal-oxygen bond energy along with σ^2 could together have a synergistic effect on the performance of the perovskite.

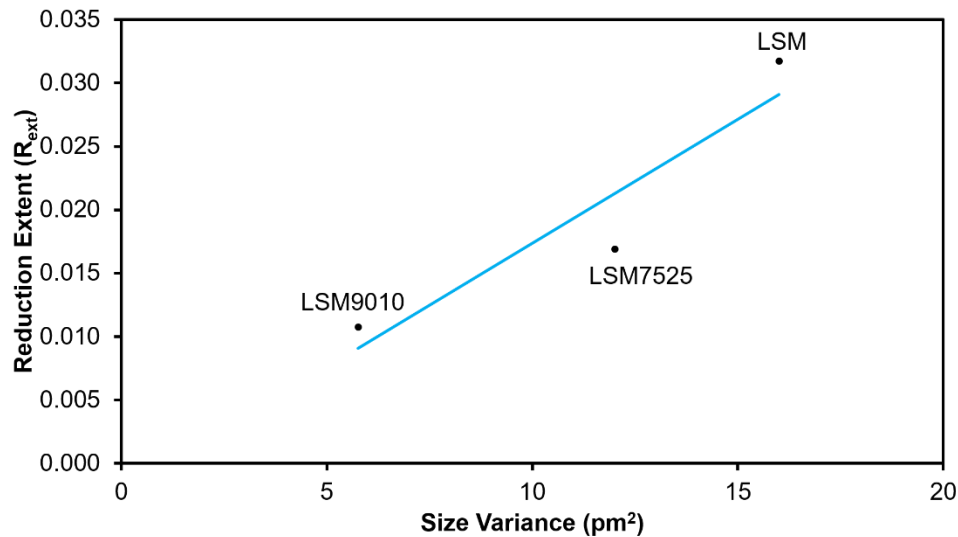


Figure 34. Reduction extent as a function of size variance at 900 °C.

Energy Dispersive Spectroscopy (EDS) images of LSM, LSM7525 and LSM9010 were taken in order to study the elemental distribution on the surface of the catalysts. The EDS images provided the mapping of the elements La, Mn, Sr and O on the surface of the perovskite catalysts. Figure 35a and Figure 35b shows the distribution of La (turquoise color) on the surface of fresh LSM and fresh LSM9010 respectively. Similarly, Figure 35c and Figure 35d shows the distribution of Mn (green color) as well as Figure 35c and Figure 35d shows the distribution of Sr (blue color).

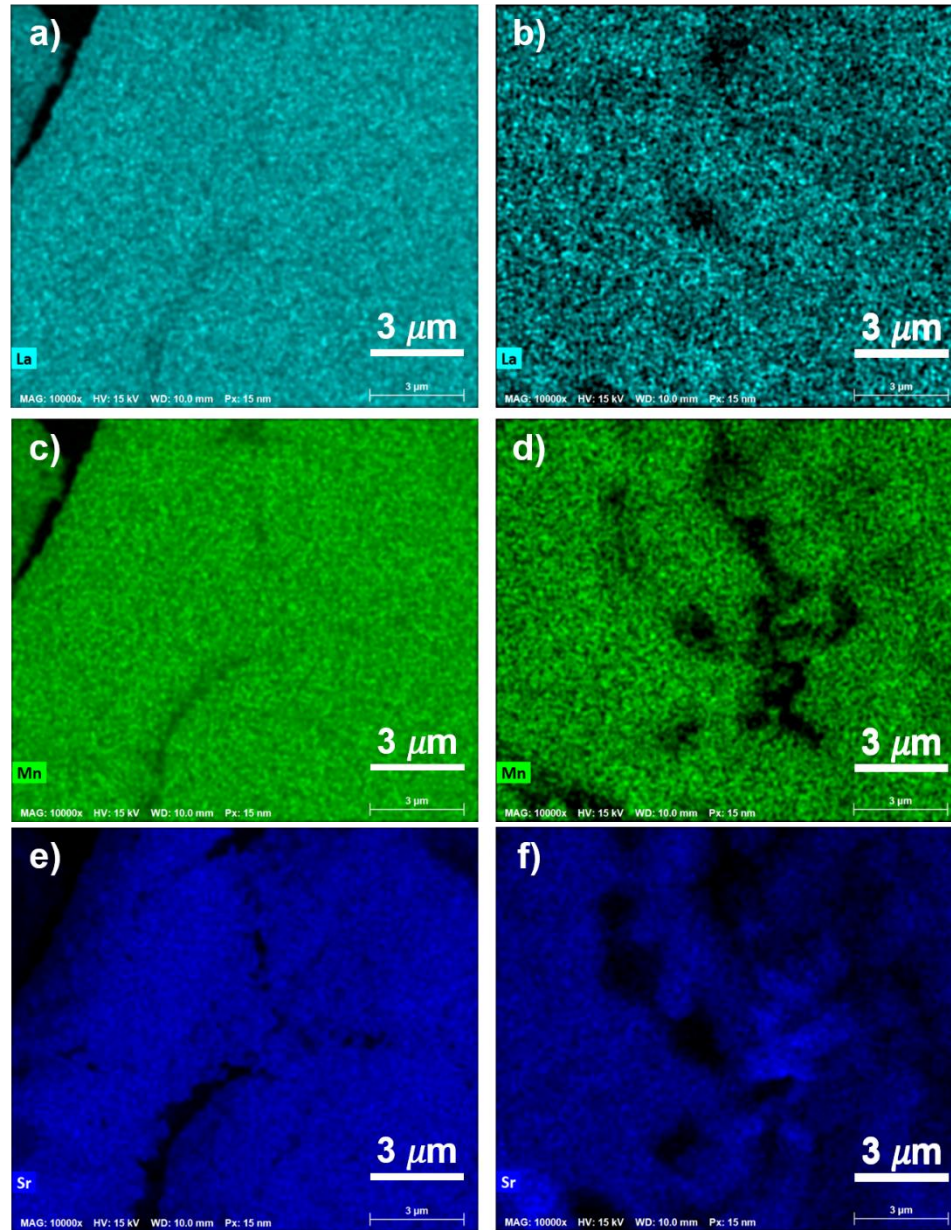


Figure 35. EDS images a) La distribution on fresh LSM b) La distribution on fresh LSM9010 c) Mn distribution on fresh LSM d) Mn distribution on fresh LSM9010 e) Sr distribution on fresh LSM f) Sr distribution on fresh LSM9010.

In the $\text{La}_{1-x}\text{Sr}_x\text{MnO}_3$ perovskite family with $x = 0.10, 0.25$ and 0.50 , LSM displayed the greatest activity and LSM9010 displayed the poorest activity. Thus, the elemental distribution on the surface of fresh LSM and fresh LSM9010 are compared in Figure 35. Figure 35a, Figure 35c and Figure 35e shows the homogeneous distribution of La, Mn and Sr respectively on the surface of fresh LSM. In Figure 35b it is evident that La is

homogeneously distributed on the surface of fresh LSM9010. However, Figure 35d shows the uneven distribution of Mn on the surface of fresh LSM9010 as indicated by some black regions devoid of the green color representing Mn. Instead these Mn absent regions are populated by Sr as indicated by bright blue spots in Figure 35f. The elemental distribution of Mn is particularly of greater importance in this case as it is the redox active site. Since, fresh LSM9010 is missing the redox active site in various regions of its surface, its activity is furthered hindered.

After the three redox cycles, XRD tests were performed on LSM, LSM7525 and LSM9010. The XRD profiles of fresh LSM, LSM7525 and LSM9010 samples and after three redox cycles at 900 °C are presented in Figure 36. All the three samples do not show any additional peaks in the XRD profiles indicating no new phase formation. Also, carbonate peaks are not evident in the XRD profiles of LSM, LSM7525 and LSM9010 as it was observed for YSM as shown in Figure 21.

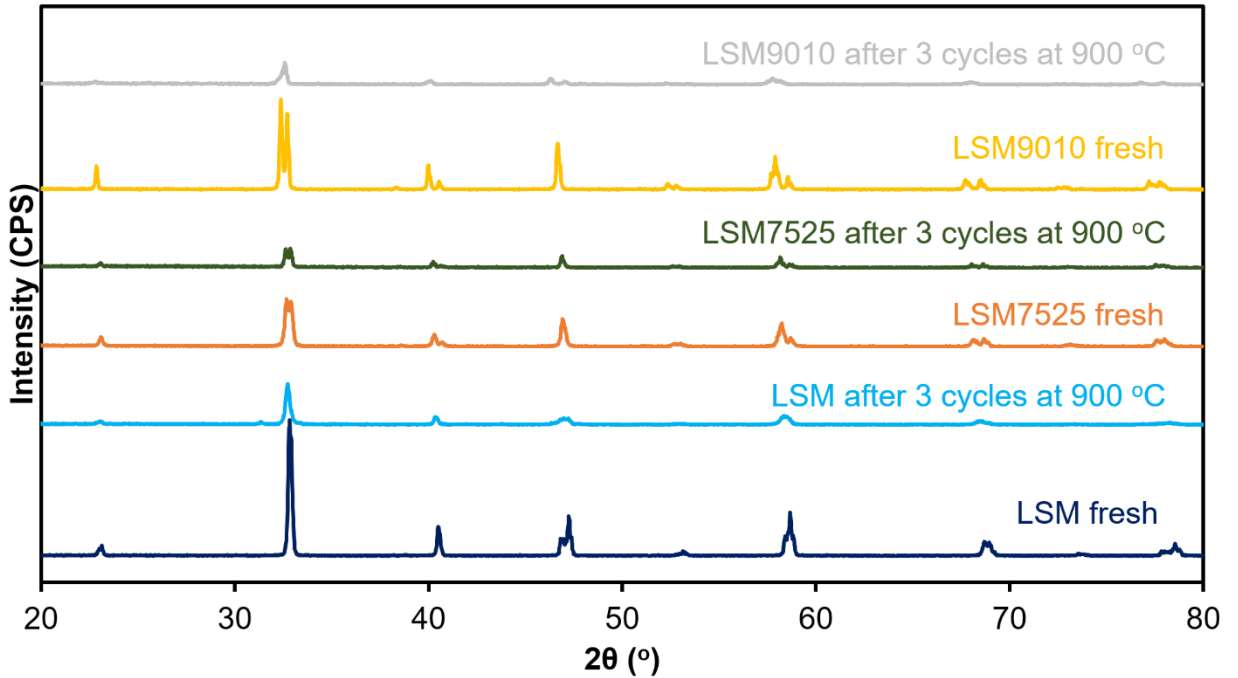


Figure 36. XRD profiles of LSM, LSM7525 and LSM9010 before and after 3 redox cycles at 900 °C.

Similarly, SEM images of the samples were also taken after the completion of the redox cycles to analyze and compare the effect of multiple reduction and oxidation reactions on the textural properties of the different samples. The SEM images of LSM and LSM7525 after three redox cycles at 900 °C are illustrated in Figure 37. By comparing Figure 37a to Figure 23a, the agglomeration of particles leading to the formation of larger crystallites or grains can be observed in the case of LSM after three redox cycles. The amalgamation of the particles can also be observed in the case of LSM7525 as well by comparing Figure 37b and Figure 23b. Higher temperatures, such as 900 °C, at which the redox reactions are performed causes the particles to coalesce into larger ones as also reported by Demont et al. and Galvez et al [30], [71]. Sintering and powder densification reduces the surface area for the redox reactions to occur and also hinders the mass transfer of gases to the redox

active sites [30]. Consequently, after the first cycle the activity of LSM, LSM7525 and LSM9010 is reduced as illustrated in Figure 27 and Figure 28. However, after the first cycle, the CO production remains almost the same in the consecutive second and third cycles for LSM, LSM7525 and LSM9010. This evidence suggests that the effect of sintering is minimal after the first redox cycle.

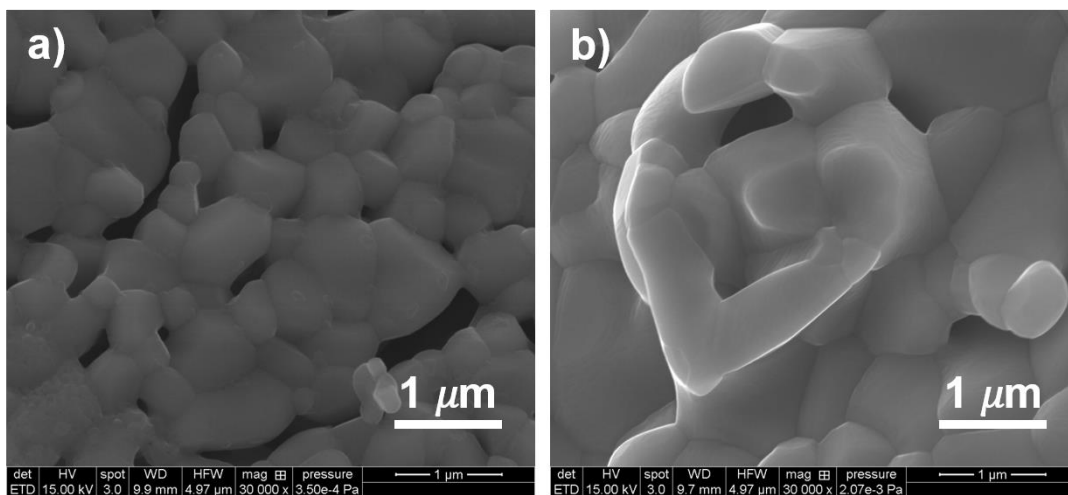


Figure 37. SEM images 30000 × magnification a) LSM after 3 redox cycles at 900 °C b) LSM7525 after 3 redox cycles at 900 °C.

3.2.3. B-site Substitution

For the A –site substitution, LSM was the optimal composition producing the highest amount of O₂ and CO. Next objective was to enhance the performance of the catalyst by performing B –site substitution. Investigation conducted by *Ezbiri et al.* showed that lanthanum-strontium-manganese-based perovskite substituted with aluminum in the B –site results in higher Mn and lower Sr concentration on the surface[25]. Consequently, La_{1-x}Sr_xMnO₃ perovskite substituted with Al in the B -site resulted in greater reduction extent and lower strontium carbonate formation than non-substituted samples [25]. Similarly, *Galvez et al.* showed that substitution of Mn by Al in the B –site of La_{1-x}Sr_xMnO₃ perovskite reduced the formation of strontium carbonate [71]. In addition, La_{1-x}Sr_xFeO₃

and $\text{La}_{1-x}\text{Sr}_x\text{Mn}_{1-y}\text{Fe}_y\text{O}_3$ perovskites have gained attention regarding CO and H_2 production as well as solid oxide fuel cells because of their unique properties [26], [35], [90], [91]. Thus, in our study we decided to substitute Mn with Al and Fe in the $\text{La}_{1-x}\text{Sr}_x\text{MnO}_3$ perovskite and compare their redox performances.

$\text{La}_{0.5}\text{Sr}_{0.5}\text{Mn}_{0.5}\text{Al}_{0.5}\text{O}_3$ (LSMA), $\text{La}_{0.5}\text{Sr}_{0.5}\text{Mn}_{0.5}\text{Fe}_{0.5}\text{O}_3$ (LSMF) and $\text{La}_{0.75}\text{Sr}_{0.25}\text{Mn}_{0.5}\text{Al}_{0.5}\text{O}_3$ (LSMA7525) were synthesized using Pechini method. $\text{La}_{0.5}\text{Sr}_{0.5}\text{Mn}_{0.5}\text{Ni}_{0.5}\text{O}_3$ (LSMN) was also synthesized but impurities were observed as shown in Figure 13. *Nair et al.* also observed impurities in the case of LSMN [29]. Likewise, $\text{La}_{0.5}\text{Sr}_{0.5}\text{Mn}_{0.5}\text{Co}_{0.5}\text{O}_3$ was prepared via Pechini method. However, during calcination melting was observed at both 1400 and 1200 °C. Single phase LSMA, LSMF and LSMA7525 were obtained as verified by the XRD profiles in Figure 13. SEM images were also taken as illustrated in Figure 38.

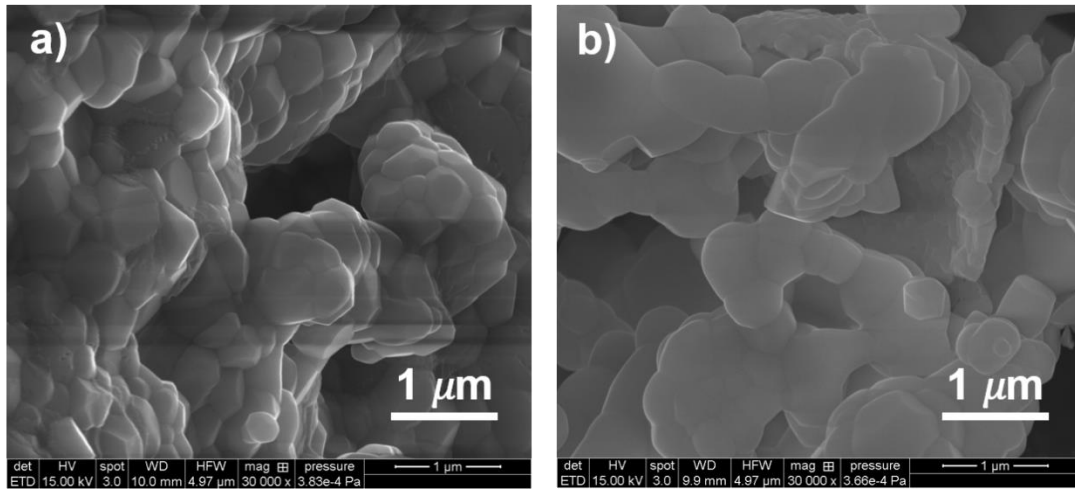


Figure 38. SEM images 30000 × magnification a) fresh LSMA b) fresh LSMF.

Initially the redox performances of LSMA and LSMF were investigated for three cycles at 800 and 900 °C in the TGA. The TGA profiles at 800 and 900 °C are displayed in Figure 39

and Figure 40 respectively. The profile of LSM is also added for comparison purposes. LSMA, LSMF and LSM all have the same A –site. It is evident from Figure 39 and Figure 40 that the performance of LSMA and LSMF are very similar at both 800 and 900 °C. However, LSM outperforms both LSMA and LSMF in regards to the reduction extent at both the temperatures. Substituting Mn with Al and Fe did not improve the stability of the perovskite as observed in Figure 40. As in the case of LSM, the activity of both LSMA and LSMF decreases after the first cycle but remains stable afterwards.

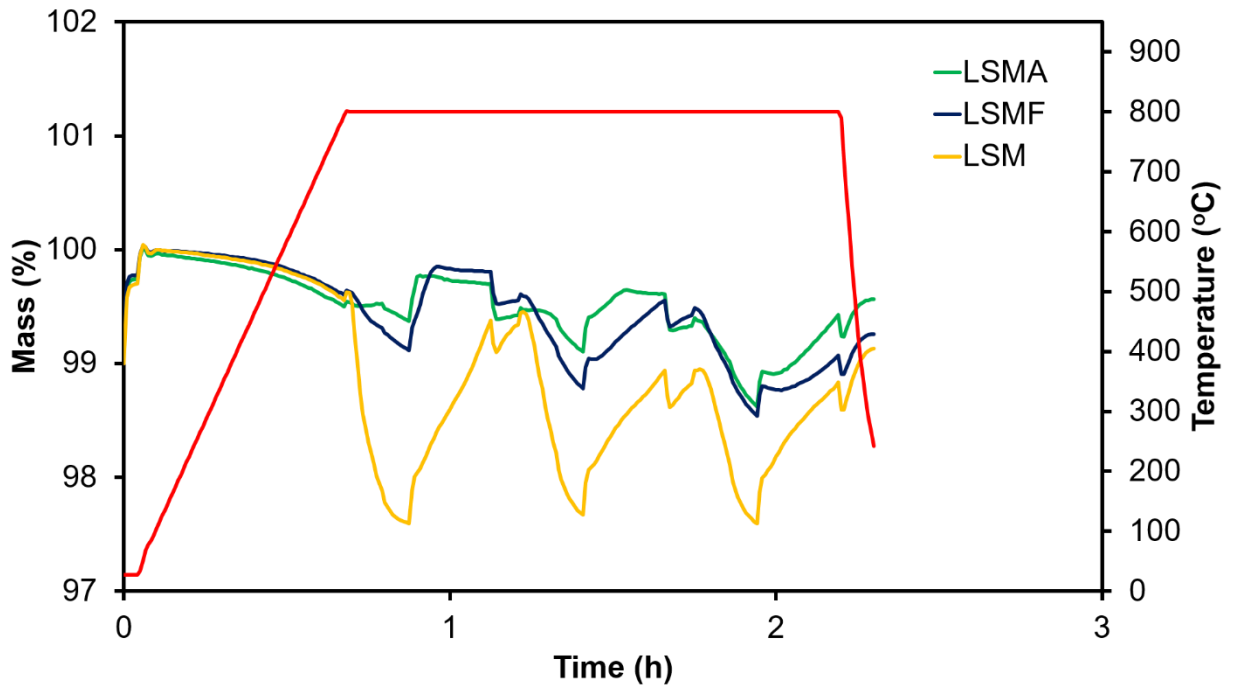


Figure 39. TGA profile of LSMA, LSMF and LSM at 800 °C.

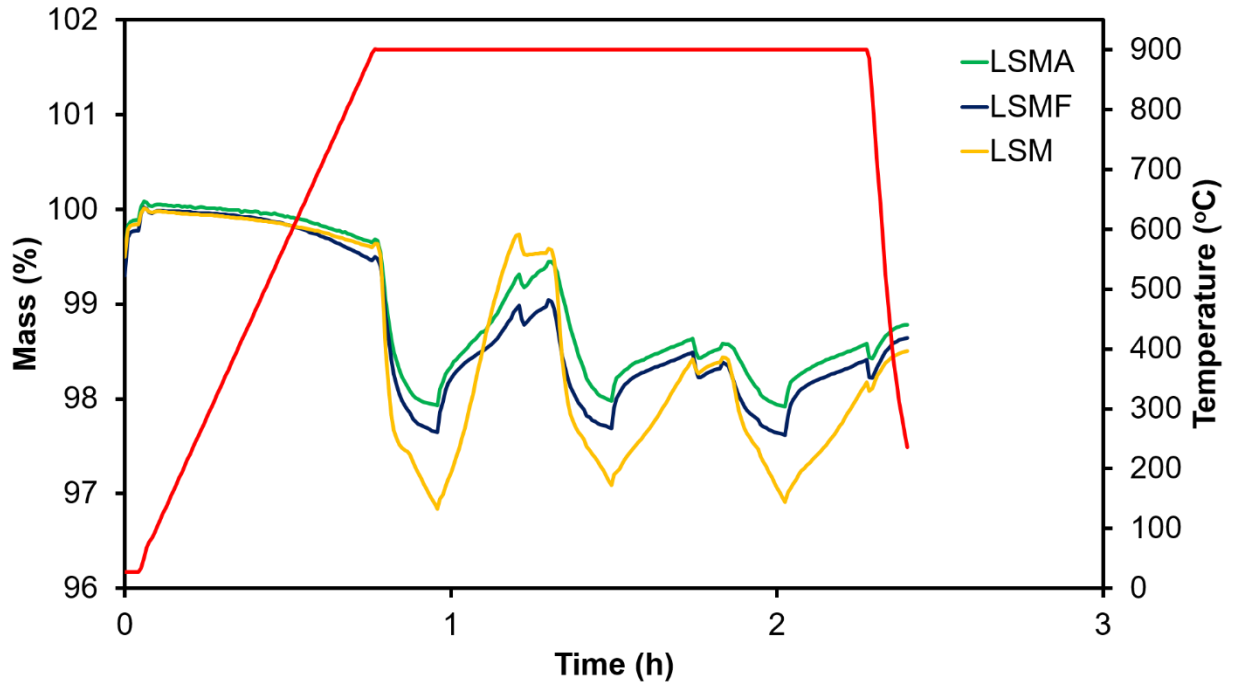


Figure 40. TGA profile of LSMA, LSMF and LSM at 900 °C.

Corresponding to the largest reduction extent, LSM produces the greatest amount of O₂ and CO compared to LSMA and LSMF at both 800 and 900 °C. At 800 °C, during the first cycle LSM, LSMA and LSMF produce 765, 201 and 288 μmolg^{-1} O₂ respectively as shown in Figure 41. As observed in the TGA profile in Figure 39 LSMA and LSMF display similar performances. Similarly, LSM, LSMA and LSMF produces 1164, 250 and 460 μmolg^{-1} CO respectively at 800 °C.

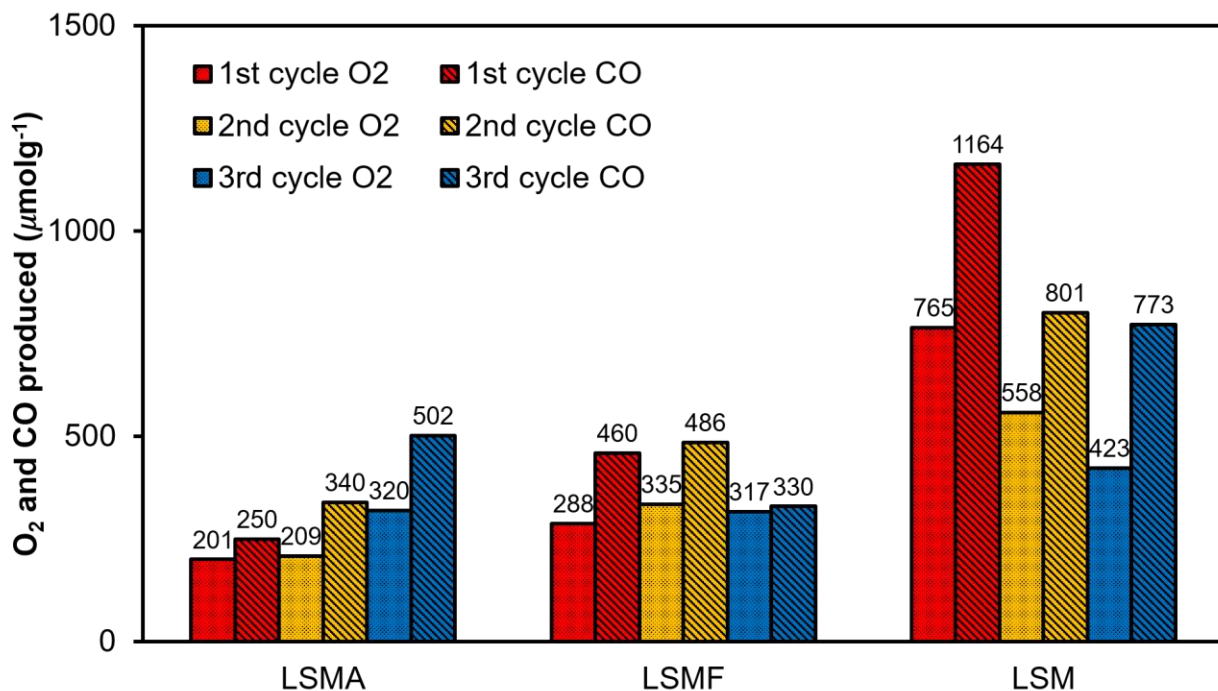


Figure 41. O₂ and CO production for LSMA, LSMF and LSM during the three redox cycles at 800 °C.

At 900 °C, during the first cycle, LSM, LSMA and LSMF produce 992, 674 and 742 μmolg^{-1} O₂ respectively as shown in Figure 42. During the re-oxidation phase of the catalyst in the first cycle, LSM, LSMA and LSMF produce 1813, 949 and 872 μmolg^{-1} CO respectively at 900 °C. LSM, LSMA and LSMF all show reduced activity after the first cycle, as LSM, LSMA and LSMF produce 827, 459 and 424 μmolg^{-1} O₂ respectively during the second cycle at 900 °C. Nevertheless, the activity remains stable after the first cycle as LSM, LSMA and LSMF produce similar amounts of CO in the second and third cycle. LSM produces 843 and 792 μmolg^{-1} CO during the second and third cycle respectively at 900 °C. LSMA produces 409 and 415 μmolg^{-1} CO during the second and third cycle respectively at 900 °C. Similarly, LSMF produces 504 and 499 μmolg^{-1} CO during the second and third cycle respectively at 900 °C. The re-oxidation percentages of LSM at 900 °C during the first, second and third cycle are 91%, 42% and 40% respectively. LSMA is

re-oxidized 70%, 30% and 31% in the first, second and third cycle respectively at 900 °C. Lastly, LSMF undergoes 59%, 34% and 34% re-oxidation during the first, second and third cycle respectively at 900 °C. From these results it is evident that LSMA and LSMF have similar performances.

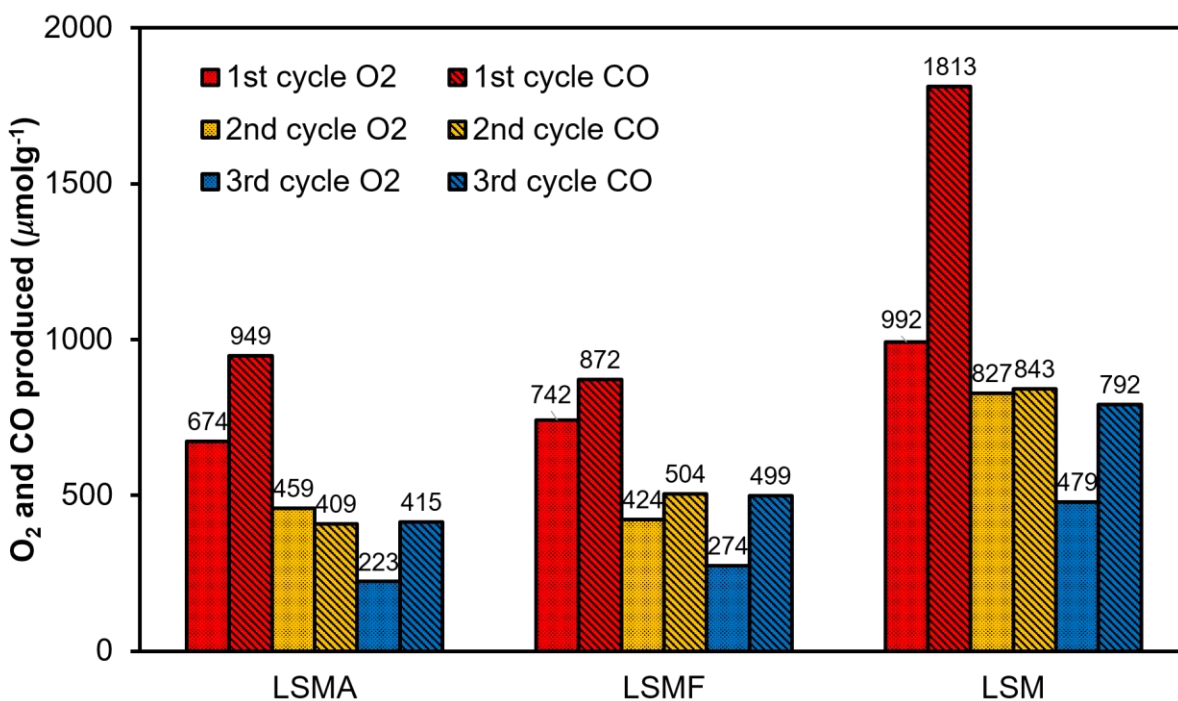


Figure 42. O₂ and CO production for LSMA, LSMF and LSM during the three redox cycles at 900 °C.

Most importantly, the performances of LSM, LSMA and LSMF reveal that substituting Mn by Al or Fe did not improve either the activity or stability of the catalyst compared to LSM. Research work of *Nair et al.* also concluded that the performance of La_{1-x}Sr_xMnO₃ perovskite was not enhanced by substituting Mn with Al or Fe [29]. The results that we obtained along with the results of *Nair et al.* are in contradiction to the work of *Ezbiri et al.* [25] The differences in the synthesis method of the catalysts as well as variations in the redox conditions could be some of the reasons for the discrepancy in the results.

EDS images as illustrated in Figure 43 can provide one of the explanations for the reduced activity of LSMA compared to LSM. Mn is the redox active site for LSM as well as for LSMA [25]. Figure 43a shows the distribution of Mn on the surface of fresh LSMA as represented by the green color. There are multiple regions in Figure 43a indicated by darker regions where Mn is absent. These regions devoid of Mn is occupied by chunks of Sr and Al instead as shown in Figure 43b and Figure 43c.

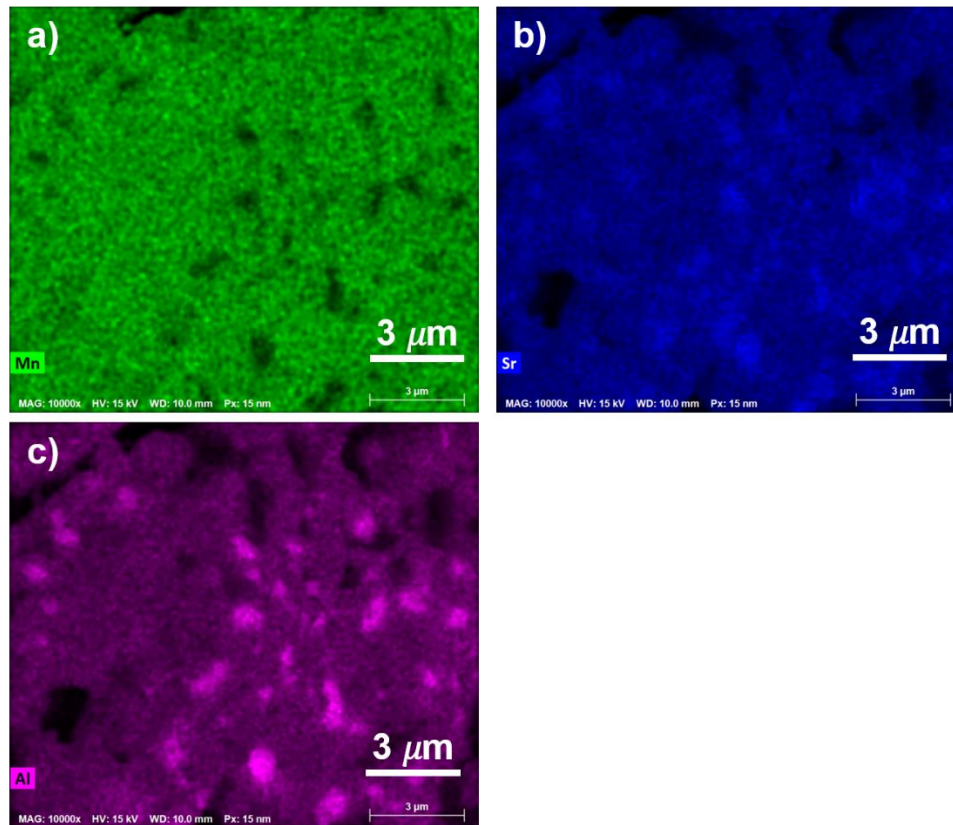


Figure 43. EDS images a) Mn distribution on the surface of fresh LSMA b) Sr distribution on the surface of fresh LSMA c) Al distribution on the surface of fresh LSMA.

In Figure 43b, the blue color represents Sr on the surface of LSMA. The bright blue spots indicates the regions with higher concentration of Sr. Similarly, the pink color in Figure 43c represents the distribution of Al over the surface of LSMA. Regions with higher concentration of Al are indicated by bright pink spots. Under careful observation it is clear

that the bright blue and bright pink spots in Figure 43b and Figure 43c respectively corresponds to the darker regions in Figure 43a devoid of Mn. Since the redox active site Mn is replaced by Al and Sr on the surface of LSMA, the activity of LSMA is reduced compared to LSM.

XRD tests were performed on LSMA and LSMF after undergoing three redox cycles. The XRD profiles of LSMF and LSMA after three redox cycles at 900 °C are displayed in Figure 44. After three redox cycles at 900 °C, XRD profiles of both LSMA and LSMF did not show any additional peaks or new phases. The single phase of both LSMA and LSMF perovskites was preserved after the three redox cycles. Just as in the case of LSM, no strontium carbonate peaks were observed in the XRD profiles of both LSMA and LSMF.

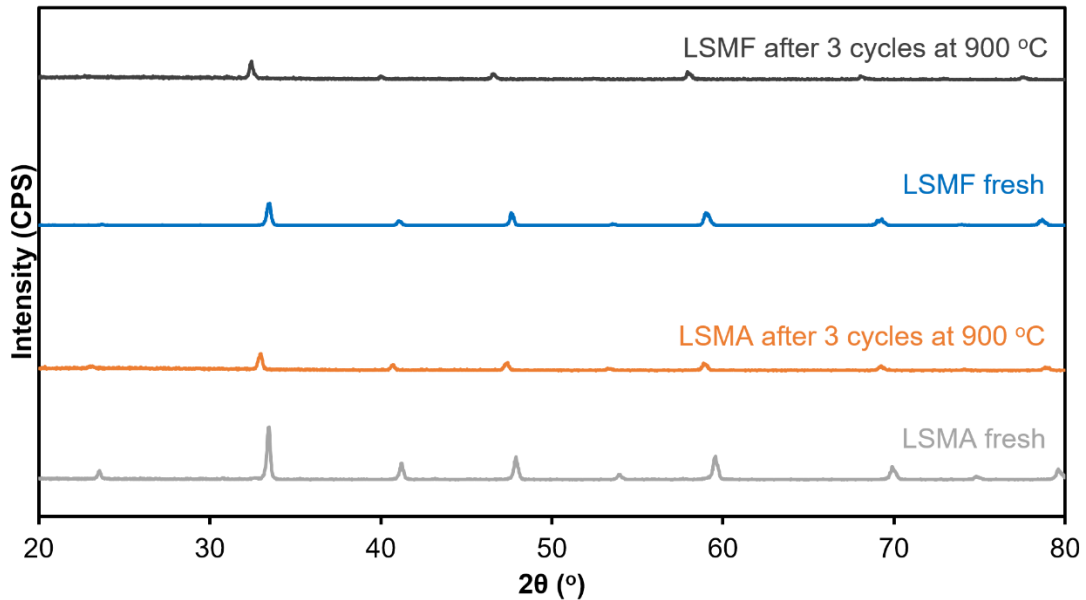


Figure 44. XRD profiles of fresh LSMA, LSMA after 3 cycles at 900 °C, fresh LSMF and LSMF after 3 cycles at 900 °C.

The perovskite samples were subjected to multiple redox cycles. SEM images of the samples were captured in order to study the impact of the redox cycles on the textural properties and surface topography of the samples. Figure 45 shows the SEM images of

LSMA before and after the three redox cycles at 900 °C. By comparing Figure 45a and Figure 45b, it is evident that the agglomeration of particles resulted in the formation of larger sized crystallite as the LSMA sample underwent three redox cycles. The higher temperature of 900 °C at which the perovskite sample is subjected to during the redox cycles causes the particles to coalesce to form larger ones [30], [71]. Similar results were observed previously in the case of LSM and LSM7525 as illustrated in Figure 37. Sintering as well as powder densification diminish the surface area for redox reactions and obstruct the mass transfer of gases to the redox active sites [30]. As a result the activity of both LSMA and LSMF decreases after the first cycle. However, the amount of CO produced in the second and third cycle remain the same for both LSMA and LSMF as shown in Figure 42. Thus, sintering and powder densification have minimal impact on the activity of LSMA and LSMF after the first redox cycle. Stable performances after the first redox cycle were also observed for LSM, LSM7525 and LSM9010 (Figure 27 and Figure 28).

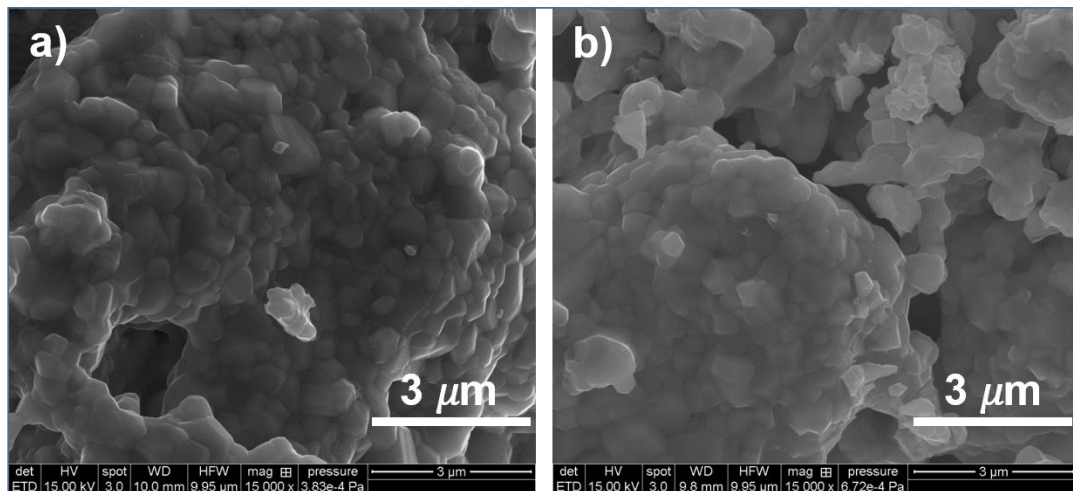


Figure 45. SEM images of a) Fresh LSMA b) LSMA after three redox cycles at 900 °C.

In addition to LSMA and LSMF, the redox performance of $\text{La}_{0.75}\text{Sr}_{0.25}\text{Mn}_{0.5}\text{Al}_{0.5}\text{O}_3$ (LSMA7525) was also investigated. The TGA profiles of LSM7525 and LSMA7525 are

displayed together for comparison purposes in Figure 46 and Figure 47. Figure 46 and Figure 47 shows the changes in the mass of LSM7525 and LSMA7525 as they both undergo redox cycling at 800 °C and 900 °C respectively. It is evident from Figure 46 that LSM7525 and LSMA7525 very identical performances at 800 °C in terms of both activity and stability. At 900 °C, LSM7525 and LSMA7525 display very similar performances in terms of stability. However, LSM7525 has a slightly greater activity than LSMA7525 as illustrated in Figure 47.

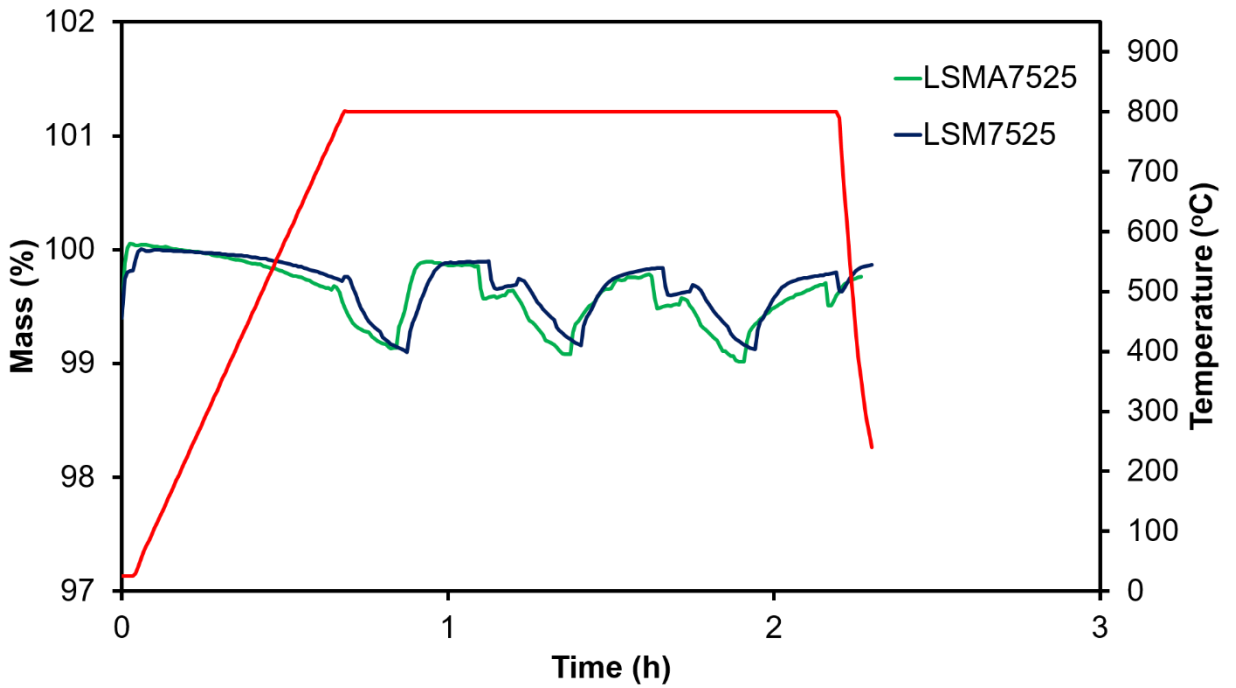


Figure 46. TGA profiles of LSM7525 and LSMA7525 at 800 °C.

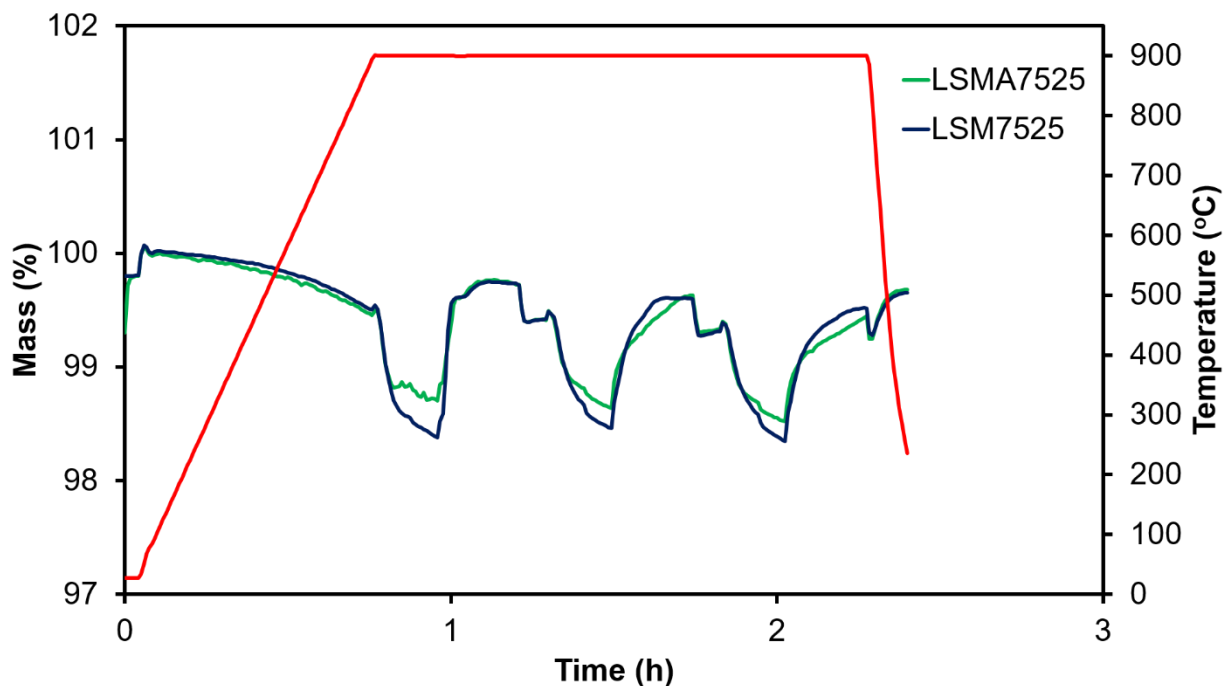


Figure 47. TGA profiles of LSM7525 and LSMA7525 at 900 °C.

The O₂ and CO production values for LSM7525 and LSMA7525 at 800 and 900 °C are displayed in Figure 48 and Figure 49 respectively. The identical performances of LSM7525 and LSMA7525 at 800 °C that were observed in Figure 46 are also reflected in Figure 48. At 800 °C, during the first, second and third cycle LSM7525 produces 282, 231 and 224 μmolg^{-1} O₂. At 800 °C, during the first, second and third cycle LSMA7525 produces 289, 255 and 241 μmolg^{-1} O₂. Similarly, during the first, second and third cycle LSM7525 produces 499, 426 and 422 μmolg^{-1} CO at 800 °C. During the first, second and third cycle LSMA7525 produces 478, 441 and 433 μmolg^{-1} CO at 800 °C. Figure 49 shows that at 900 °C, the activity of LSM7525 is slightly greater than that of LSMA7525 during the three redox cycles. At 900 °C, during the first, second and third cycle LSM7525 produces 529, 403 and 394 μmolg^{-1} O₂. At 900 °C, during the first, second and third cycle LSMA7525

produces 421, 353 and 347 μmolg^{-1} O_2 . Similarly, during the first, second and third cycle LSM7525 produces 857, 717 and 734 μmolg^{-1} CO at 900 °C. During the first, second and third cycle LSMA7525 produces 666, 620 and 581 μmolg^{-1} CO at 900 °C. As in the case of LSM, LSM7525, LSM9010, LSMA and LSMF, the activity of LSMA7525 decreases after the first cycle and remains the same in the second and third cycle at both 800 and 900 °C. Sintering and powder densification play a significant role in reducing the activity of LSMA7525 after the first cycle. Nevertheless, sintering and powder densification have minimal impact on the activity of LSMA7525 after the first cycle. Therefore, substituting Mn with Al in the B –site did not improve both the activity and stability of LSMA7525 compared to LSM7525.

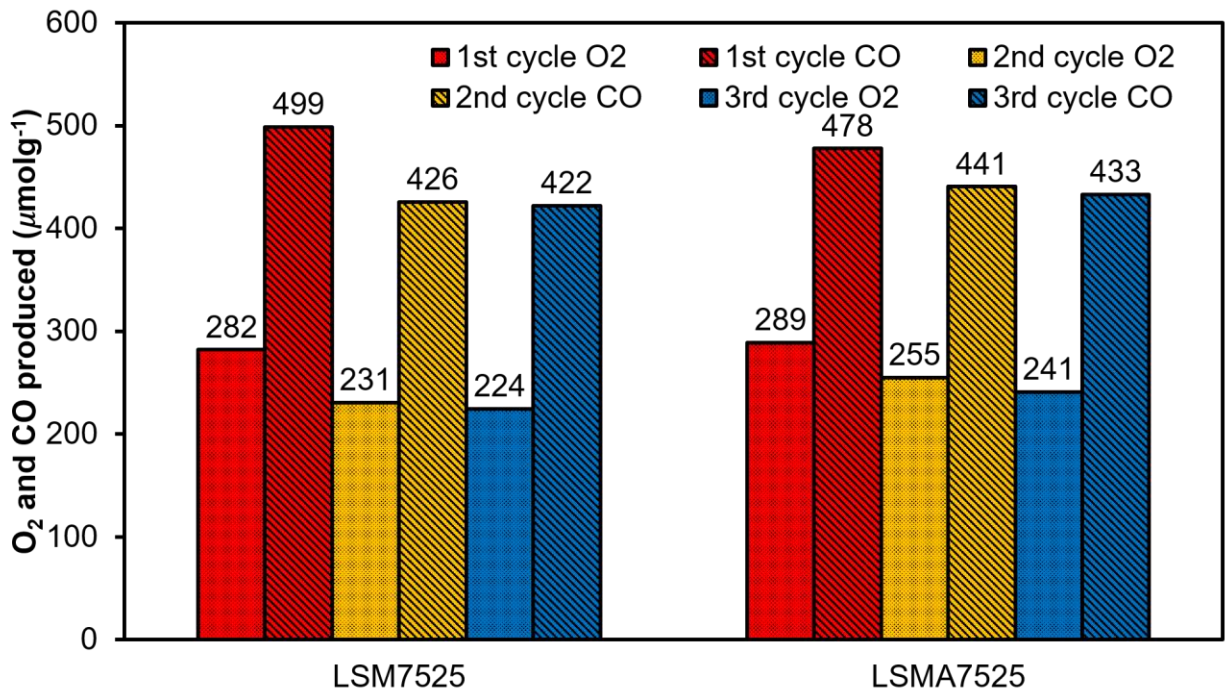


Figure 48. O_2 and CO production for LSM7525 and LSMA7525 at 800 °C.

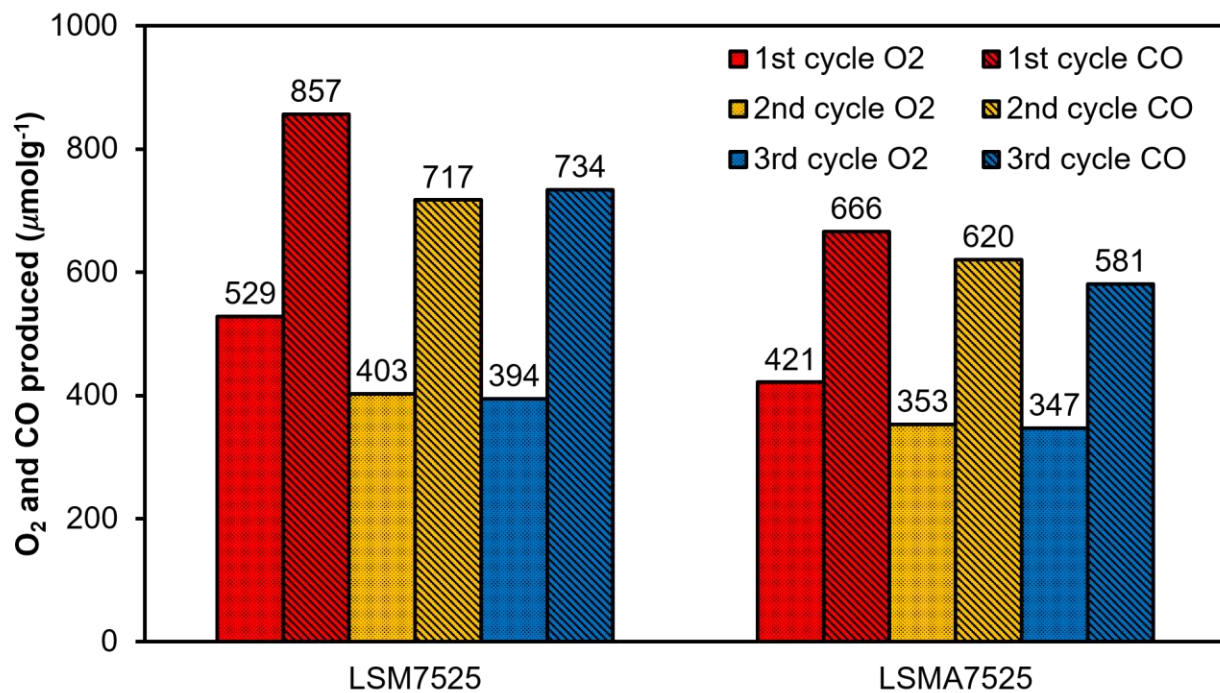


Figure 49. O₂ and CO production for LSM7525 and LSMA7525 at 900 °C.

3.2.4. Comparison between thermal reduction and reduction using methane

There have been numerous studies performed regarding the solar thermochemical splitting of CO₂ using perovskites [25], [26], [71]. However, the thermal reduction phase during the redox cycle of the perovskites takes place at extremely high temperatures of 1400 °C [26], [29]. *Steinfeld et al.* have mentioned that the use of methane (CH₄) as a reducing agent lowers the reduction temperature of perovskites [21]. Thus, in our study we have also used CH₄ for the reduction of the perovskites. By using CH₄ the reduction temperature was lowered down to a range of 700 – 900 °C. Perovskites were reduced to a much larger extent at 900 °C using CH₄ than at 1400 °C using solar thermal energy without any CH₄ [26], [29]. A comparison of the amount of O₂ evolved via the two different reduction routes is presented in Table 2. *Nair et al.* synthesized the perovskite samples La_{0.5}Sr_{0.5}MnO₃ (LSM), La_{0.5}Ca_{0.5}MnO₃ (LCM) and Y_{0.5}Sr_{0.5}MnO₃ (YSM) using the same Pechini method and calcination temperature as we used in our investigation [29]. Reduction of the perovskites was performed by *Nair et al.* at 1400 °C under thermal energy for 45 minutes. Whereas in our investigation the reduction was performed at 900 °C under 15 % (by volume) CH₄ for 7 minutes. Under the reduction conditions in our study, LSM produced 992 μmolg⁻¹ O₂ during the first redox cycle. But under the reduction conditions mentioned by *Nair et al.* 256 μmolg⁻¹ O₂ was produced. Similarly, LCM produced 840 μmolg⁻¹ O₂ under the reduction conditions in our study. While under the reaction conditions outlined by *Nair et al.*, LCM produced 314 μmolg⁻¹ O₂. Lastly, in our investigation YSM produced 1362 μmolg⁻¹ O₂. *Nair et al.* reported 539 μmolg⁻¹ O₂ was produced by YSM. In addition, *Dey et al.* synthesized LSM, LCM and YSM via the solid-state reactions route [26]. However, the reduction conditions in the investigation conducted by *Dey et al.* was identical to the

reduction conditions reported by *Nair et al.* [26], [29]. Under the reduction conditions reported by Dey et al. LSM, LCM and YSM produced 201, 315 and 483 μmolg^{-1} O_2 during the first redox cycle. Thus, it is evident that perovskites are reduced to a greater extent under CH_4 than only under thermal energy.

Table 2. O_2 evolution during the reduction phase of the first redox cycle under different reduction conditions.

Sample	Synthesis method	Reduction Conditions		1 st Cycle O_2 evolved (μmolg^{-1})	References
		Temp ($^{\circ}\text{C}$)	Reducing Agent		
LSM	Pechini	900	CH_4	992	This study
	Pechini	1400	None	256	[29]
	Solid-state reactions	1400	None	201	[26]
LCM	Pechini	900	CH_4	840	This study
	Pechini	1400	None	314	[29]
	Solid-state reactions	1400	None	315	[26]
YSM	Pechini	900	CH_4	1362	This study
	Pechini	1400	None	539	[29]
	Solid-state reactions	1400	None	483	[26]

In our investigation we also conducted numerous redox cycling of the perovskites in the TGA under thermal energy without CH_4 during the reduction phase. This section explores the differences in the performances of the perovskites during the redox cycling under CH_4 reduction and under thermal reduction. Just as in the case of CH_4 reduction, once the target redox cycling temperature was reached, the perovskite samples were reduced thermally for

7 minutes. But during thermal reduction, N₂ at 20 mL/min (100 Vol%) was only allowed to flow into the TGA. Similarly, during re-oxidation of the perovskite, CO₂ at 10 mL/min (50 Vol%) along with N₂ at 10 mL/min (50 Vol%) was allowed to flow into the TGA for 15 minutes.

The TGA profiles of CM reduced thermally and using methane at 800 °C are illustrated together in Figure 50 for comparison purposes. It is evident from Figure 50 that there is a significant difference in the reduction extent of CM when CH₄ is used as a reducing agent and when only thermal energy is used.

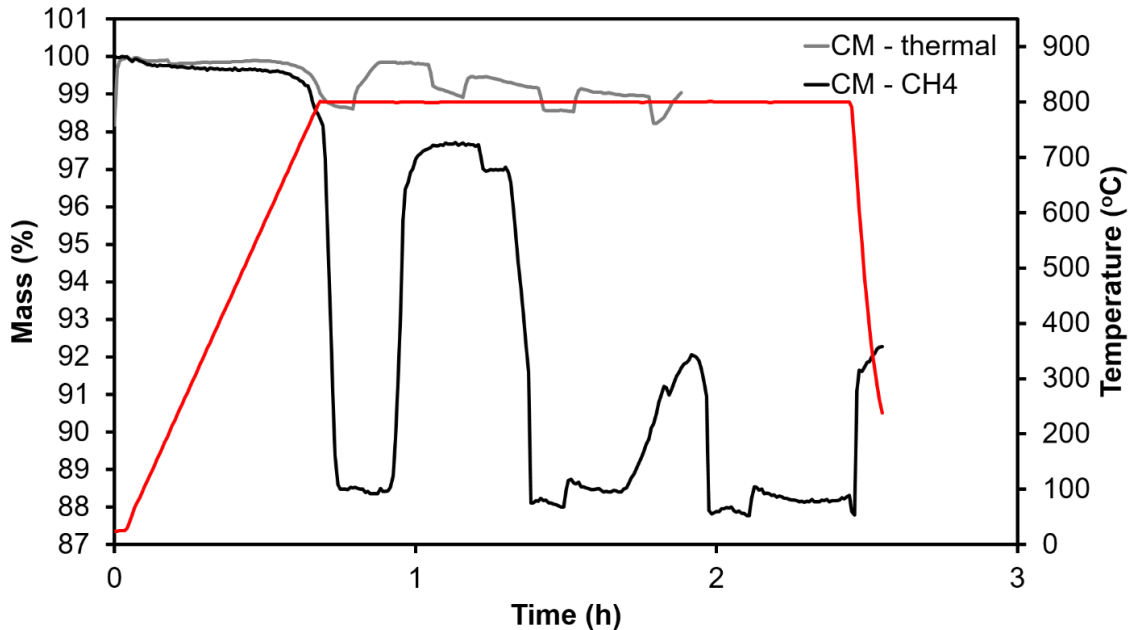


Figure 50. TGA profiles of CM reduced thermally and using CH₄ at 800 °C.

The TGA profiles of LSM reduced thermally and using CH₄ at 800 °C are displayed together in Figure 51. As in the case of CM, LSM is also reduced to a much larger extent by using CH₄ than by using thermal energy.

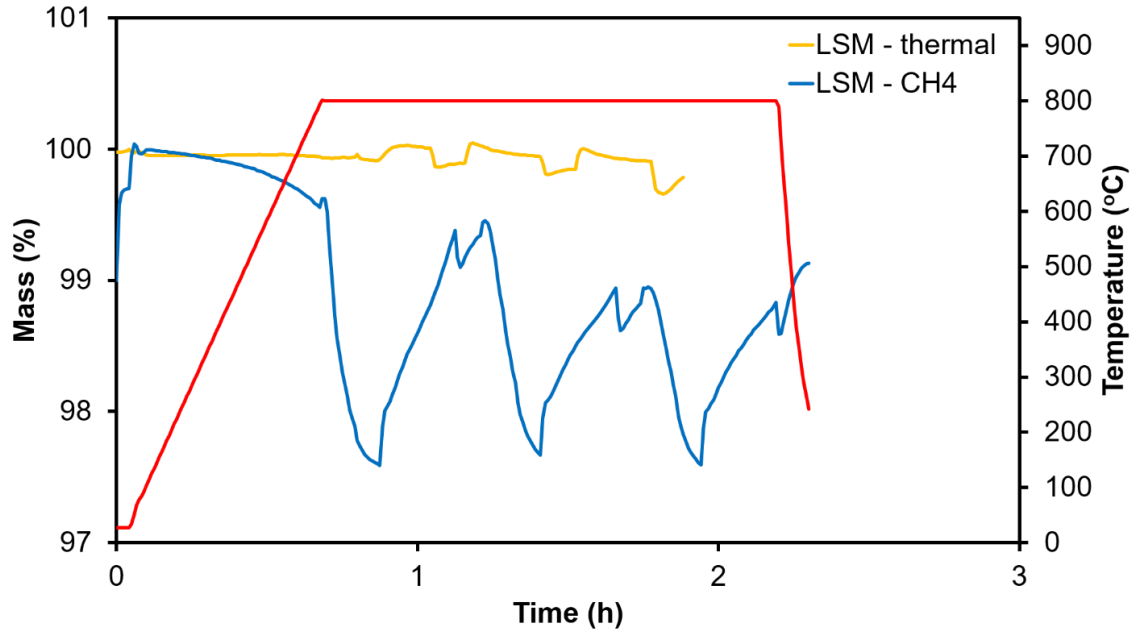


Figure 51. TGA profiles of LSM reduced thermally and using CH_4 at 800 °C.

The effect of using CH_4 versus using only thermal energy in the reduction of LSM9010 at both 800 °C and 900 °C is presented in Figure 52 and Figure 53. At both 800 and 900 °C, LSM9010 is reduced to a greater extent by using CH_4 than by using only thermal energy.

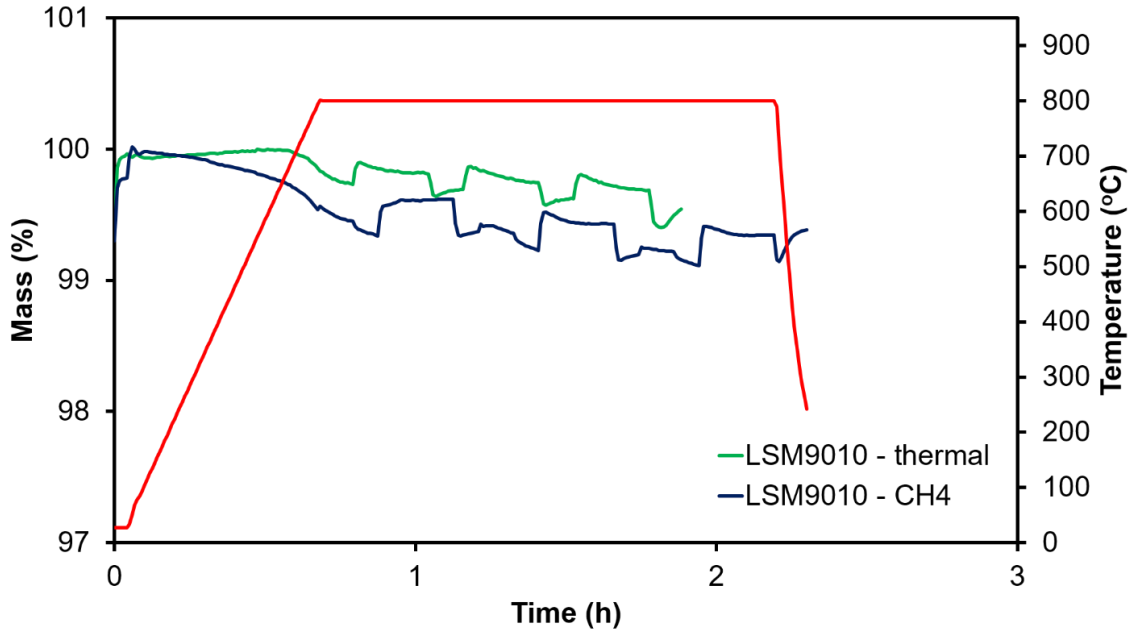


Figure 52. TGA profiles of LSM9010 reduced thermally and using CH_4 at 800 °C.

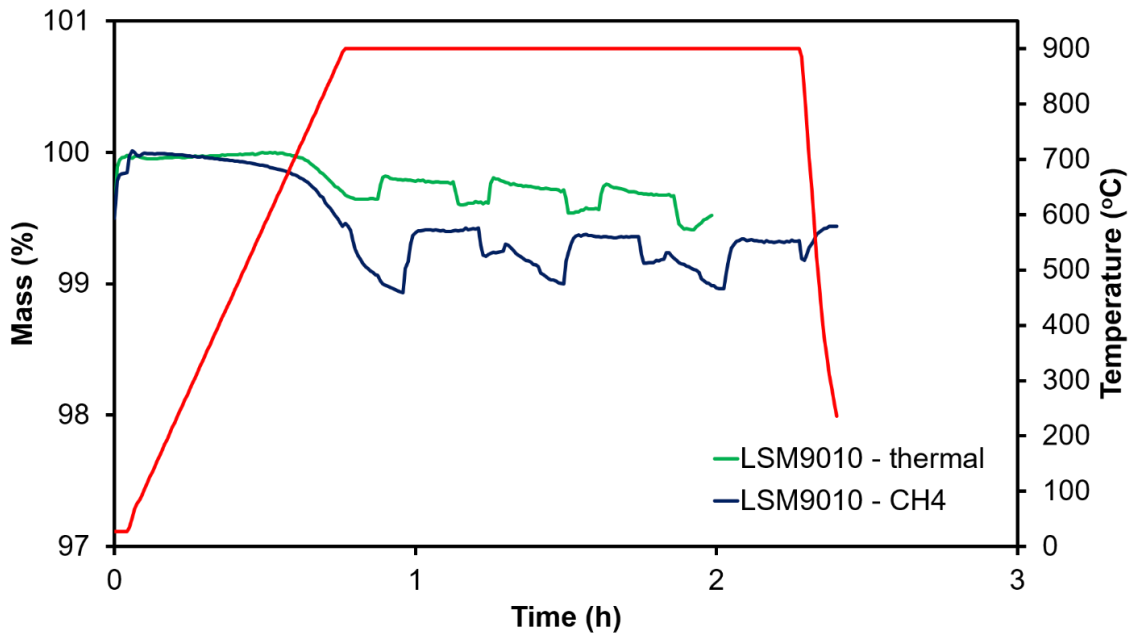


Figure 53. TGA profiles of LSM9010 reduced thermally and using CH_4 at 900 °C.

CH_4 reduces CM to a larger extent than by only thermal energy during redox cycling.

Consequently, greater amount of O_2 and CO are produced during the redox cycles when

CH₄ is used as a reducing agent than when only thermal energy is applied. For instance, in Figure 54 it can be observed that during the first redox cycle at 800 °C, 3641 μmolg⁻¹ O₂ is released from CM when CH₄ is used for reduction. Whereas, 567 μmolg⁻¹ O₂ is released when CM is reduced thermally during the first cycle at 800 °C. 1047 μmolg⁻¹ CO is produced by CM during the first redox cycle at 800 °C when only thermal energy is used. But when CH₄ is used as a reducing agent, the CO production increases to 5849 μmolg⁻¹ during the first redox cycle at 800 °C. Similarly, it is clear from Figure 54 that CM produces more O₂ and CO during the second and third redox cycles at 800 °C when CH₄ is used as a reducing agent.

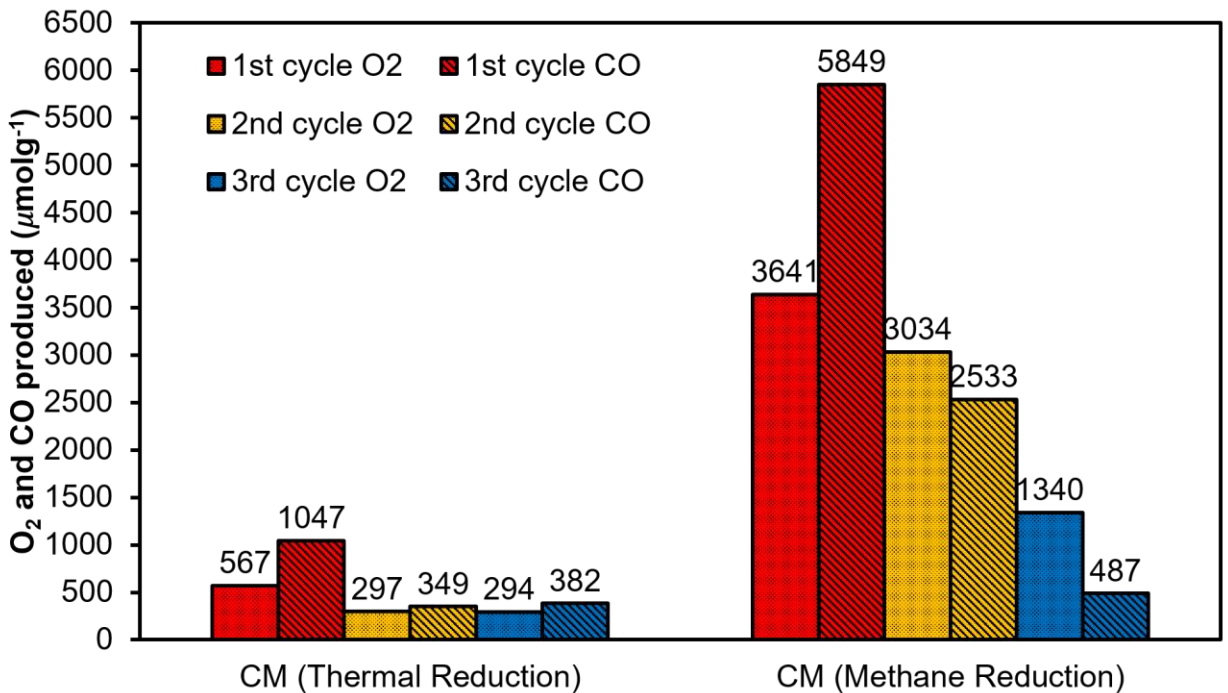


Figure 54. O₂ and CO production values for CM reduced thermally and using CH₄ during the three redox cycles at 800 °C.

At 800 °C, LSM produces more O₂ and CO during all the three redox cycles when using CH₄ for reduction than when only using thermal energy as observed in Figure 55. Redox

cycling incorporating CH₄ produces 765, 558 and 423 μmolg⁻¹ O₂ during the first, second and third cycle respectively at 800 °C in the case of LSM. Whereas 27, 53 and 75 μmolg⁻¹ O₂ is released from LSM during the first, second and third cycle respectively at 800 °C when only thermal energy is provided.

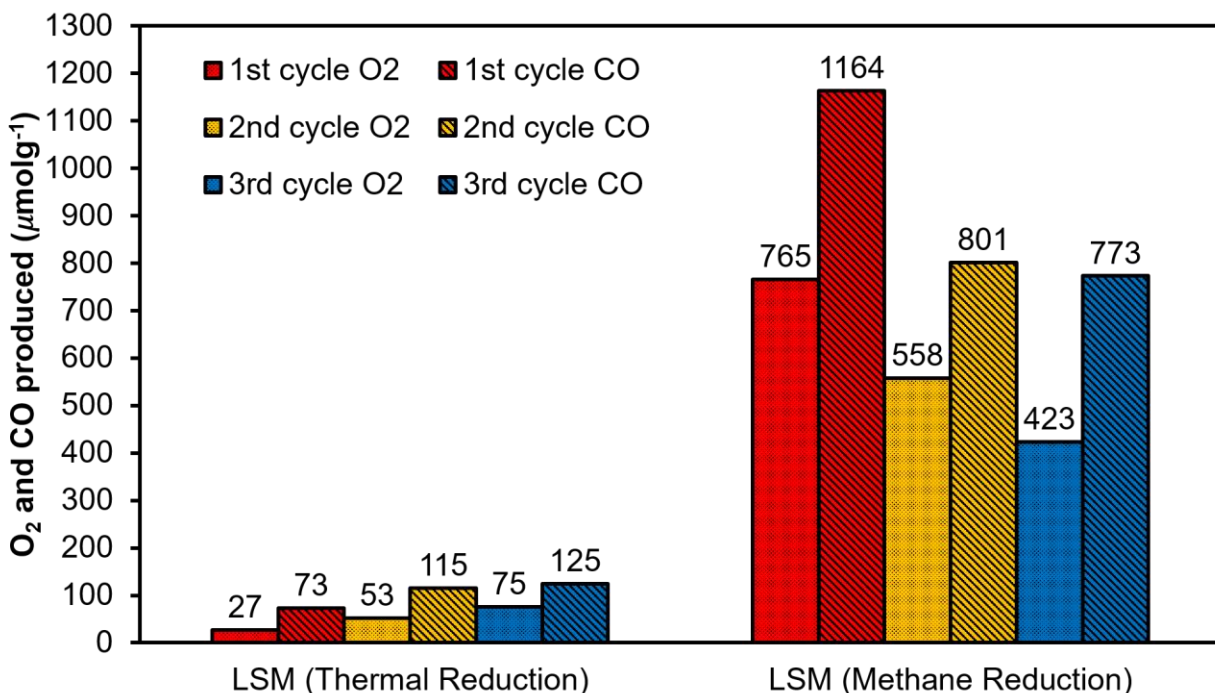


Figure 55. O₂ and CO production values for LSM reduced thermally and using CH₄ during the three redox cycles at 800 °C.

As in the case of CM and LSM, LSM9010 also produces more O₂ and CO during all the redox cycles at both 800 and 900 °C when CH₄ is used as a reducing agent than when only heat energy is provided. This phenomena can be observed in both Figure 56 and Figure 57. Thermal reduction of LSM9010 releases 84, 81 and 92 μmolg⁻¹ O₂ during the first, second and third cycle respectively at 800 °C as illustrated in Figure 56. On the other hand, CH₄ reduction of LSM9010 releases 212, 122 and 127 μmolg⁻¹ O₂ during the first, second and third cycle respectively at 800 °C. The redox cycling of LSM9010 involving CH₄, produces

176, 182 and 187 μmolg^{-1} CO during the first, second and third cycle respectively at 800 $^{\circ}\text{C}$. Whereas the redox cycling of LSM9010 involving only thermal energy, produces 105, 143 and 145 μmolg^{-1} CO during the first, second and third cycle respectively at 800 $^{\circ}\text{C}$. 153, 69 and 83 μmolg^{-1} O_2 is released during the first, second and third cycle respectively as LSM9010 undergoes thermal reduction at 900 $^{\circ}\text{C}$ (Refer to Figure 57). Likewise, 337, 134 and 129 μmolg^{-1} O_2 is released during the first, second and third cycle respectively as LSM9010 undergoes CH_4 reduction at 900 $^{\circ}\text{C}$. When CH_4 is used to reduce LSM9010, 307, 236 and 237 μmolg^{-1} CO is evolved during the first, second and third cycle respectively at 900 $^{\circ}\text{C}$. In contrast to the redox cycling involving CH_4 , the redox cycling of LSM9010 incorporating only thermal energy produces 196, 128 and 137 μmolg^{-1} CO during the first, second and third cycle respectively at 900 $^{\circ}\text{C}$.

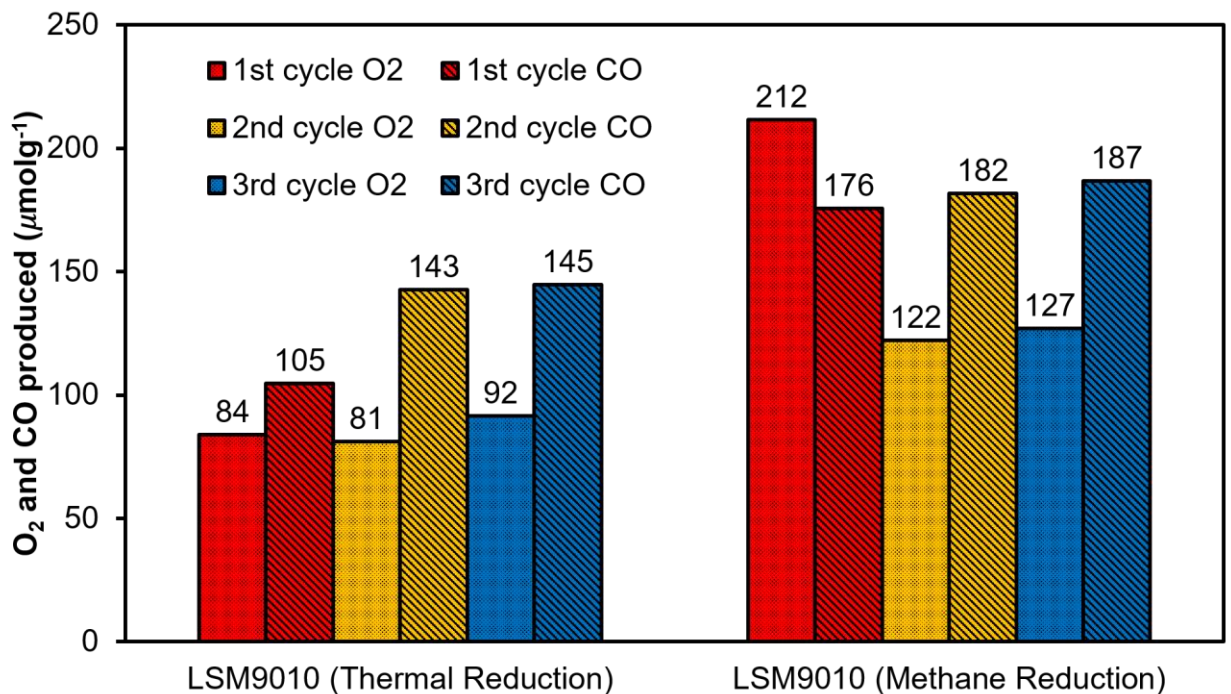


Figure 56. O_2 and CO production values for LSM9010 reduced thermally and using CH_4 during the three redox cycles at 800 $^{\circ}\text{C}$.

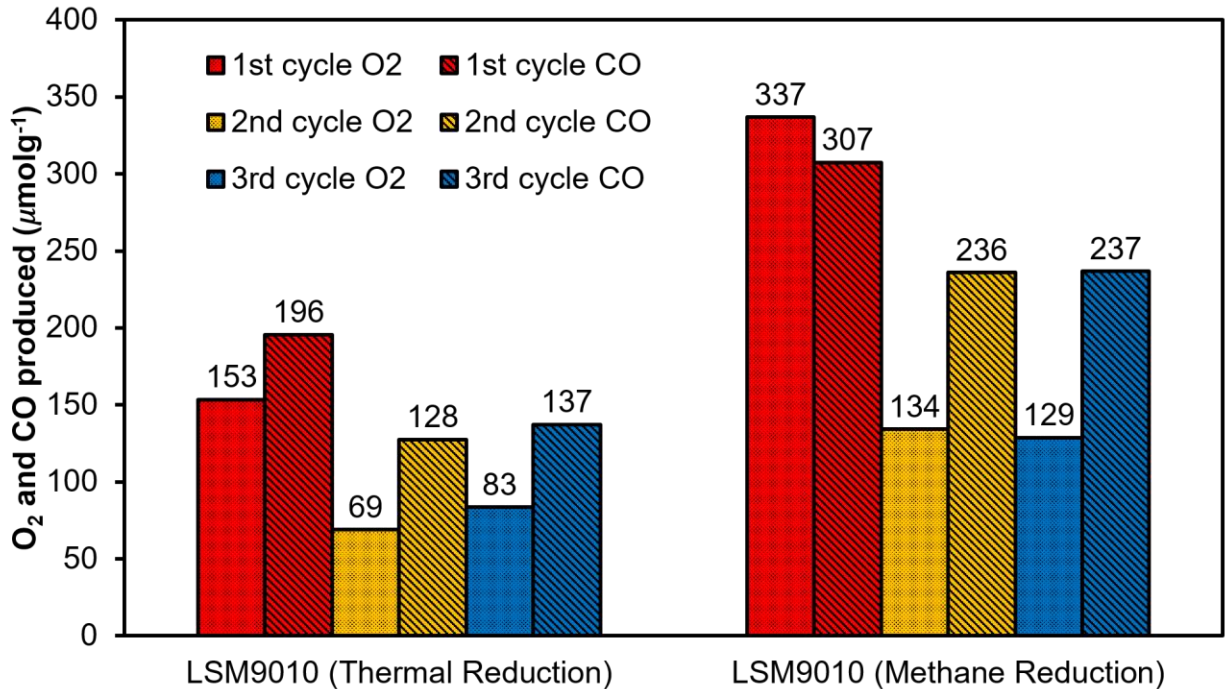


Figure 57. O₂ and CO production values for LSM9010 reduced thermally and using CH₄ during the three redox cycles at 900 °C.

In the following step, the apparent activation energy for the thermal reduction of LSM9010 was computed and compared to the apparent activation energy for the CH₄ reduction of LSM9010. In the previous section, the CH₄ reduction of LSM, LSM7525 and LSM9010 was investigated using a contracting-sphere or shrinking grain model. Therefore, the thermal reduction of LSM9010 was analysed using the same shrinking grain model. The kinetic parameters such as activation energy were evaluated for the thermal reduction of LSM9010 by using the same procedure that was applied to calculate the kinetic parameters for the CH₄ reduction of LSM, LSM7525 and LSM9010. Consequently, in the beginning the graph of $1 - (1 - X)^{\frac{1}{3}}$ versus t was plotted as illustrated in Figure 58. Then, a linear section with the maximum slope value at the very start of the reduction phase was identified in the plot of $1 - (1 - X)^{\frac{1}{3}}$ versus t as displayed in Figure 58. This linear section

corresponds to the kinetically controlled region and the maximum slope value is the true intrinsic surface reaction rate (r_0) when conversion fraction (X) is zero.

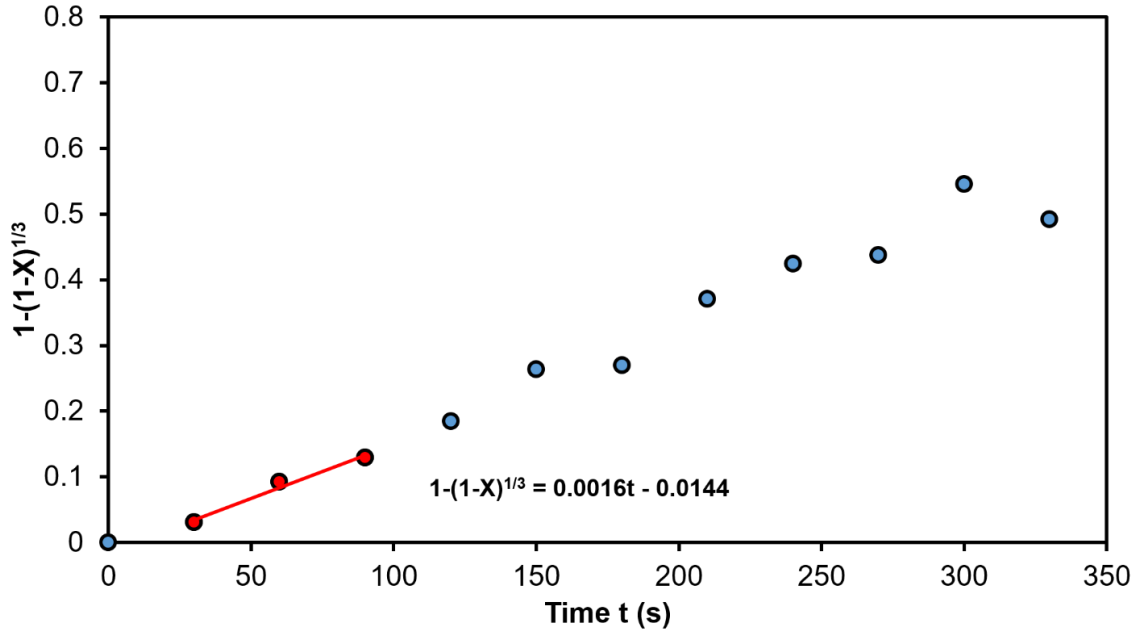


Figure 58. $1-(1-X)^{1/3}$ versus time for thermal reduction of LSM9010 at 800 °C.

Once the true intrinsic surface reaction rate (r_0) values were evaluated, the graph of $\ln(r_0)$ versus $1/T$ was plotted as shown in Figure 59. The activation energy is then calculated by multiplying the absolute value of the slope of the linear fit and the universal gas constant.

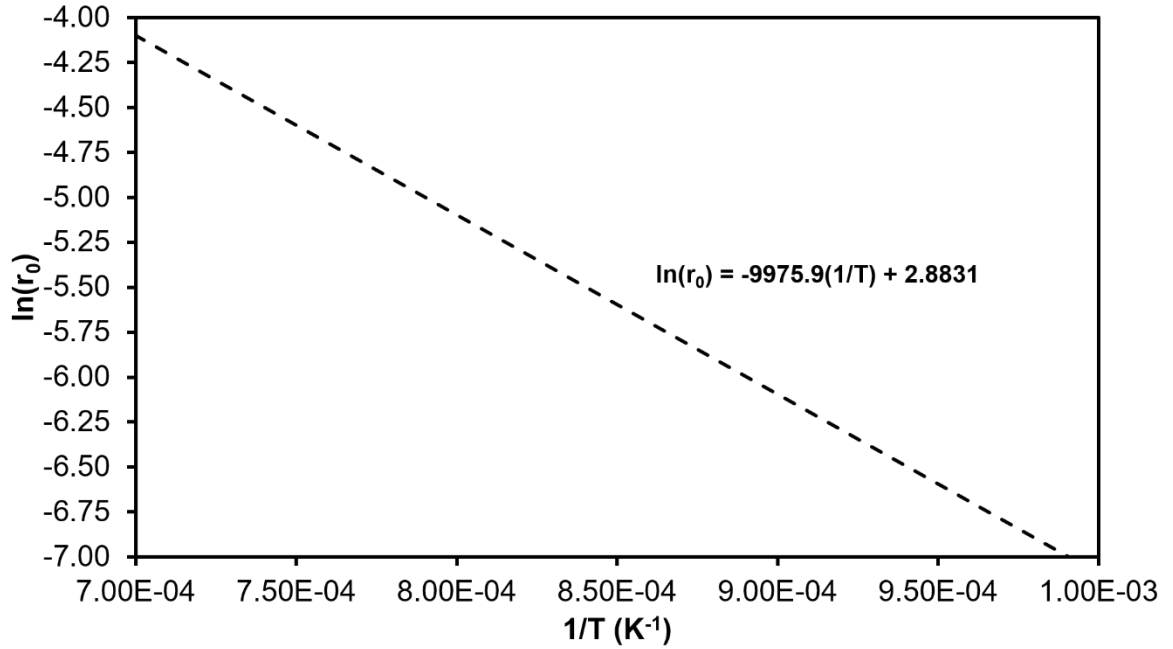


Figure 59. $\ln(r_0)$ vs $(1/T)$ for LSM9010 under thermal reduction.

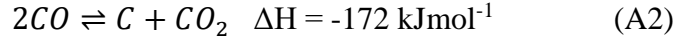
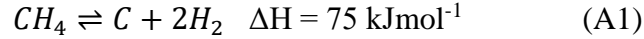
The activation energies for the thermal and CH_4 reduction of LSM9010 are listed in Table 3. The activation energy for the thermal reduction of LSM9010 is 1.5 times the activation energy for the CH_4 reduction of LSM9010. In addition to the thermal energy, reducing agents such as CH_4 further helps in the removal of oxygen from the perovskite. Therefore, the apparent energy barrier for the CH_4 reduction of LSM9010 is lower than the apparent energy barrier for the thermal reduction of LSM9010.

Table 3. Activation energy of LSM9010 during thermal and CH_4 reduction.

Sample	Synthesis Method	Reducing Agent	Activation Energy (kJ/mol)	References
LSM9010	Pechini	None	83	This study
LSM9010	Pechini	CH_4	54	This study

3.2.5. Long-term Stability Tests

One of the major concerns regarding the reduced activity of the catalyst is carbon deposition. Carbon can be deposited on the catalyst by two different reactions [92]–[94]:



Reaction A1 is the methane decomposition reaction and reaction A2 is the Boudouard reaction. For the reactions above 820 °C, only the methane decomposition reaction is responsible for carbon deposition [92]. In our study the redox cycling are performed at 700, 800 and 900 °C. Thus, for the reactions at 900 °C, carbon could be deposited by the decomposition of methane.

Studies have shown that transition metals such as Ni, Co and Fe can deposit carbon by splitting methane [95]. *Guo et al.* illustrated that partial oxidation of methane using LaNiO_3 results in the deposition of graphitic carbon [96]. Research conducted by *Alvarez-Galvan et al.* showed that methane oxidation over LaCoO_3 perovskites resulted in carbon deposition as revealed by Raman spectroscopy [93]. Similarly, oxidation of methane using $\text{LaFeO}_{3-\delta}$ and $\text{La}_x\text{Sr}_{1-x}\text{FeO}_{3-\delta}$ caused the deposition of solid carbon [94]. However, for $\text{LaAl}_{1-x}\text{Mn}_x\text{O}_3$ compounds carbon deposition was not detected during the oxidation of methane [97]. Due to the absence of Ni and Co in the perovskite samples investigated in the present study, the possibility of carbon formation from methane decomposition is greatly decreased. Nevertheless, one of the samples contain Fe.

The basicity of alkaline earth metals such as Ca and Sr inhibits the deposition of carbon from methane decomposition [98], [99]. Substitution of La with Sr or Ca increases the

basicity of the perovskite compounds. Consequently, the resistance to coke formation increases as La is substituted with Sr or Ca [100]. All the perovskite materials investigated in the present study either have Sr or Ca as the alkaline earth metal in the A –site. Therefore, carbon deposition on the surface of the investigated perovskite samples could be hindered. Moreover, long-term stability tests were performed on LSM9010, LSM7525, LSM, LSMA and LSMF to investigate the impact of carbon deposition as well as sintering and powder densification. Figure 60 shows the TGA profiles of LSM9010, LSM7525, LSM, LSMA and LSMF for 10 redox cycles at 900 °C. From Figure 60 it is evident that all the samples display stable performances after the first cycle. Similar trends were observed in section 3.4.1, 3.4.2 and 3.4.3 of this thesis when the perovskite samples underwent three redox cycles.

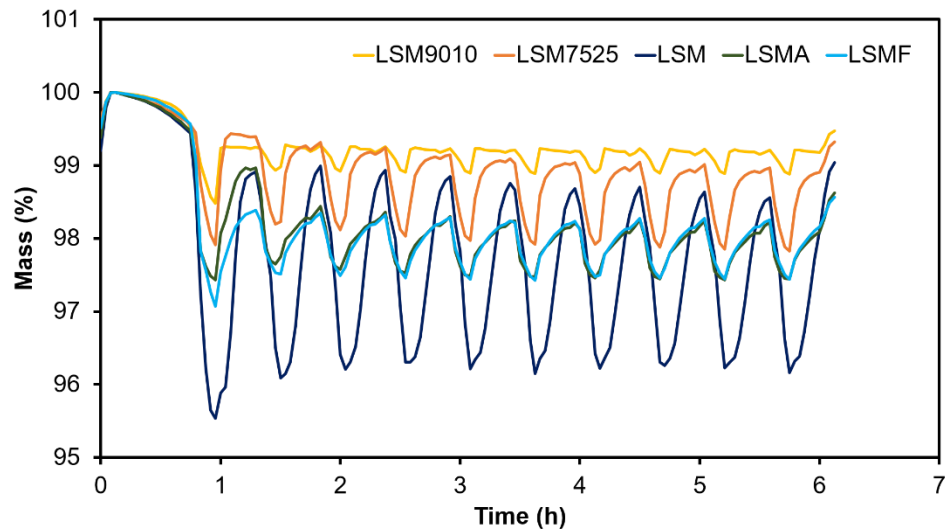


Figure 60. TGA profiles of LSM9010, LSM7525, LSM, LSMA and LSMF for 10 redox cycles at 900 °C.

From the TGA profiles illustrated in Figure 60, the O₂ and CO production values were computed. The O₂ and CO production values for the samples at 900 °C are displayed in Figure 61 and Figure 62 respectively. Both the O₂ and CO production values remain stable after the first redox cycle for all of the samples. Similar results were obtained for the tests

involving just three redox cycles. Just as in the case of the tests involving three redox cycles, the reduced performance of the perovskites after the first redox cycle observed during the long-term stability tests could be attributed to sintering and powder densification. The long-term stability tests show that the effect of sintering and powder densification is minimal after the first redox cycle. For solar thermochemical redox cycling of perovskites, there was also a reduction in the performance after the first redox cycle. However, the performance remained stable after the first cycle [30]. In addition, methane was not used during the solar thermochemical redox cycling. The consistency in the trends observed for the thermochemical redox cycling involving and not involving methane also suggest that the effect of carbon deposition could be insignificant in the present investigation.

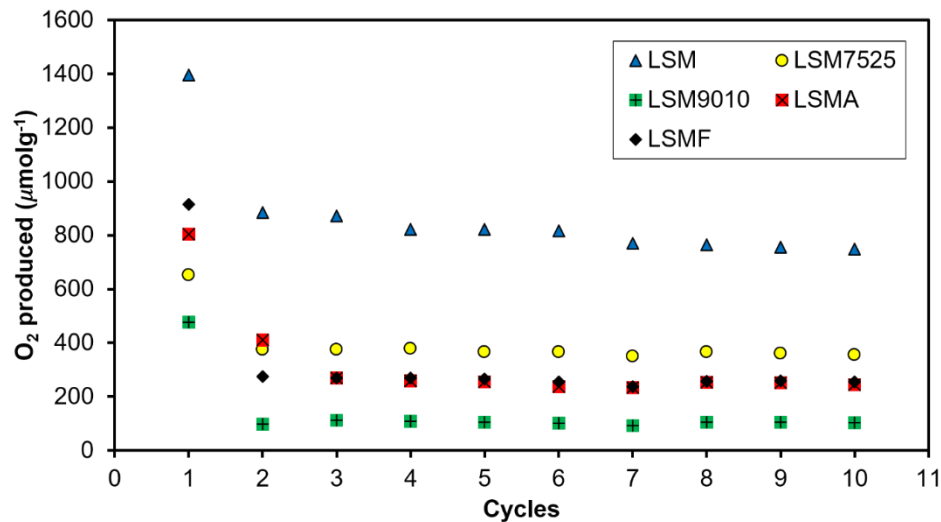


Figure 61. O₂ production values for LSM, LSM7525, LSM9010, LSMA and LSMF during the 10 redox cycles at 900 °C.

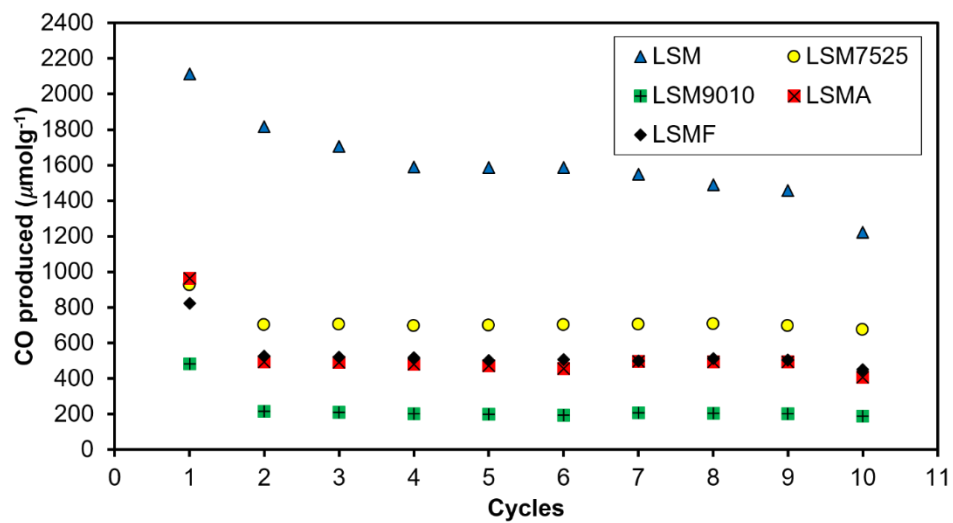


Figure 62. CO production values for LSM, LSM7525, LSM9010, LSMA and LSMF during the 10 redox cycles at 900 °C.

CHAPTER FOUR: FACTORS AFFECTING REDUCTION EXTENT AND OXYGEN NON-STOICHIOMETRY

The reduction extent (R_{ext}) of the samples were calculated using the formula:

$$R_{ext} = \frac{\Delta m_{red}}{m_s} = \frac{m_{i,red} - m_{f,red}}{m_s} \quad (11)$$

Where, Δm_{red} is the change in mass of the perovskite sample after the completion of the reduction phase, m_s is the original mass of the perovskite sample, $m_{i,red}$ is the mass of the perovskite sample at the onset of the reduction phase and $m_{f,red}$ is the mass of the perovskite sample at the completion of the reduction phase. Reduction extent is the mass of monoatomic oxygen released per unit mass of the perovskite sample.

Similarly, the oxygen non-stoichiometry (δ) was evaluated using the formula:

$$\delta = \frac{\Delta m_{red}}{m_s} \times \frac{M_s}{M_O} = \frac{m_{i,red} - m_{f,red}}{m_s} \times \frac{M_s}{M_O} \quad (12)$$

Where, M_s is the molar mass of the perovskite sample and M_O is the molar mass of monoatomic oxygen. Oxygen non-stoichiometry is the number of moles of monoatomic oxygen released per unit mole of the perovskite sample.

Various factors affecting both the reduction extent (R_{ext}) and the oxygen non-stoichiometry (δ) were investigated. This section explores different the factors such as size variance, Goldschmidt tolerance factor, A –site and B –site cationic radii, electronegativity difference between metal cations and oxygen as well as metal-oxygen bond strength.

4.1. Goldschmidt Tolerance Factor

Goldschmidt tolerance factor is often used to describe the connection between the composition, structure and properties of perovskites [57]. *Dey et al.* showed that in the family of $\text{Ln}_{0.5}\text{A}_{0.5}\text{MnO}_3$ (Ln = lanthanide, A = Sr, Ca) perovskite, the manganite with the smallest rare earth metal cation has the lowest Goldschmidt tolerance factor and releases the highest amount of O_2 per gram of catalyst [26].

Goldschmidt tolerance factor (t) for a perovskite ABO_3 is computed using the formula [55]:

$$t = \frac{r_A + r_O}{\sqrt{2}(r_B + r_O)} \quad (13)$$

Where, r_A and r_B are the A –site and B –site ionic radii respectively. r_O is the ionic radii of oxygen. For an ideal cubic perovskite structure, $r_A + r_O = \sqrt{2}(r_B + r_O)$ and $t = 1$ [54], [55]. Thus, the Goldschmidt tolerance factor measures deviation of the perovskite structure from the ideal cubic structure. According to *Johnsson et al.* for $0.89 < t < 1$, the structure of the perovskite is still cubic [55]. *Attfield* pointed out that perovskites with $0.8 < t < 1$ are usually stable [57]. A –site metals with smaller radii can lower the value of t to less than 1. For values of t in the lower section of the range $0.8 < t < 1$, the BO_6 octahedra of the perovskite structure tilts to fill up the space left out by the smaller A –site metal [55], [58]. Consequently the symmetry of the structure is lowered. GdFeO_3 with $t = 0.81$ has an orthorhombic structure [55], [57]. For $t > 1$, such as in the case of BaNiO_3 , the structure is hexagonal [55].

In the present study, the Goldschmidt tolerance factor (t) of all the investigated perovskite samples were computed. For all the samples except for LSMA and LSMA7525, the values

of t were between 0.96 and 1 as illustrated in Figure 63 and Figure 64. However, the t values of LSMA and LSMA7525 were in the close proximity of 1. Figure 63 and Figure 64 shows the plot of both the reduction extent (R_{ext}) and the final oxygen non-stoichiometry ($3-\delta$) versus the Goldschmidt tolerance factor at 800 and 900 °C respectively. At both the temperatures, the reduction extent increases as the value of t decreases from 1. Similarly, at both the temperatures the final oxygen non-stoichiometry decreases as the value of t decreases from 1. As the value of t decreases from 1, the lattice distortion increases and the Mn-O-Mn angles decreases [26], [57], [101]. The lowering of the Mn-O-Mn angles diminishes the spatial overlap of the Mn e_g and O $2p\sigma$ orbitals [101]. Thus, the ability of the perovskite to release oxygen increases as the radii of the A-site metal decreases [26].

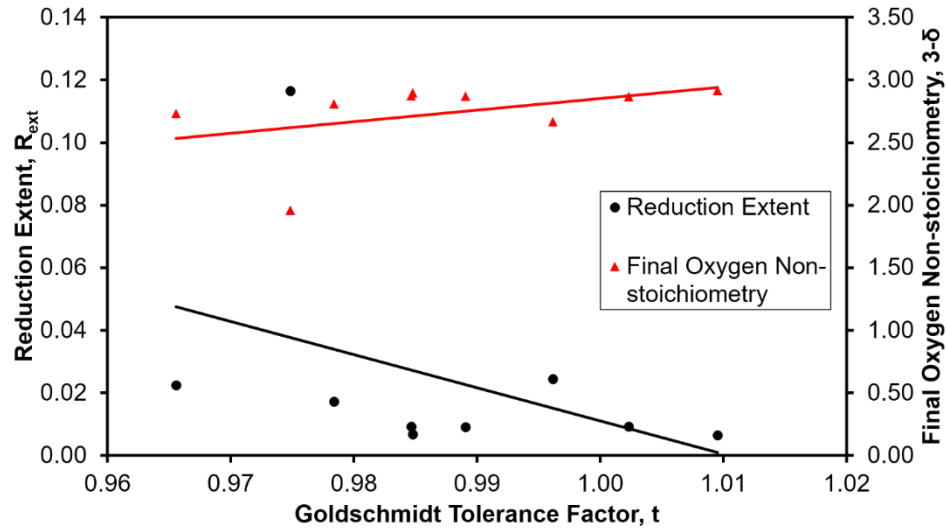


Figure 63. Reduction extent and final oxygen non-stoichiometry versus the Goldschmidt tolerance factor at 800 °C.

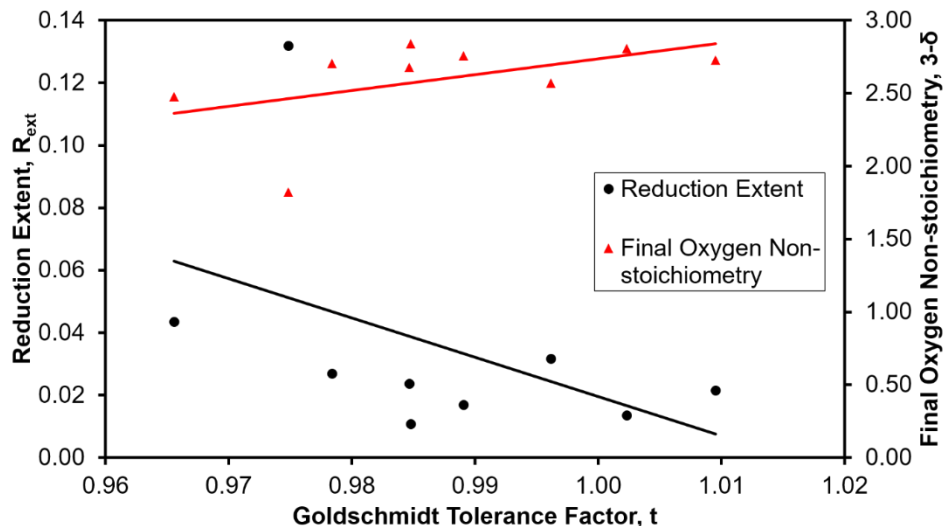


Figure 64. Reduction extent and final oxygen non-stoichiometry versus the Goldschmidt tolerance factor at 900 °C.

For some of the points in Figure 63 and Figure 64, during the computation of t the values of r_A changes as r_B remains constant. Whereas for other points when t is calculated the values

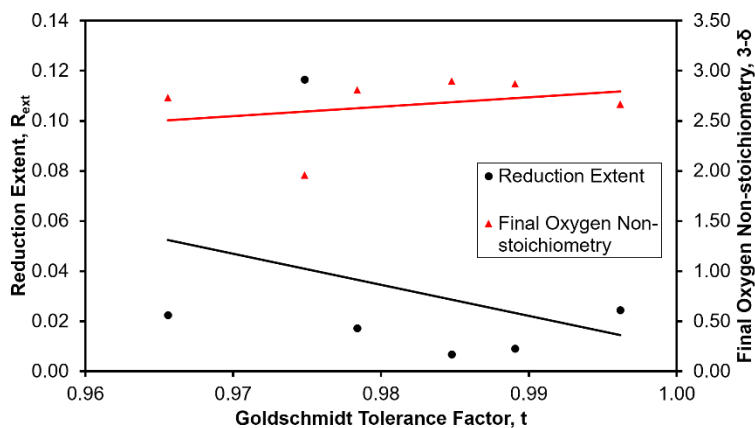


Figure 65. Reduction extent and final oxygen non-stoichiometry versus the Goldschmidt tolerance factor for samples with the same B-site composition at 800 °C.

of r_B changes but r_A remains constant. To avoid this discrepancy, in Figure 65 and Figure 66 R_{ext} and $3-\delta$ versus t are plotted for samples with the same B-site composition. Thus, for the points in Figure 65 and Figure

66, the t values are calculated keeping r_B constant while changing r_A . The trend of both the plots of R_{ext} versus t and $3-\delta$ versus t are similar to the trends observed in Figure 63 and Figure 64. At 800 °C, as the radius of the A-site cation decreases, t decreases and the

reduction extent increases while the final oxygen non-stoichiometry decreases (Figure 65). At 900 °C, as the A –site ionic radii decreases from 1, the reduction extent increases and the final oxygen non-stoichiometry decreases. The increase in reduction extent means

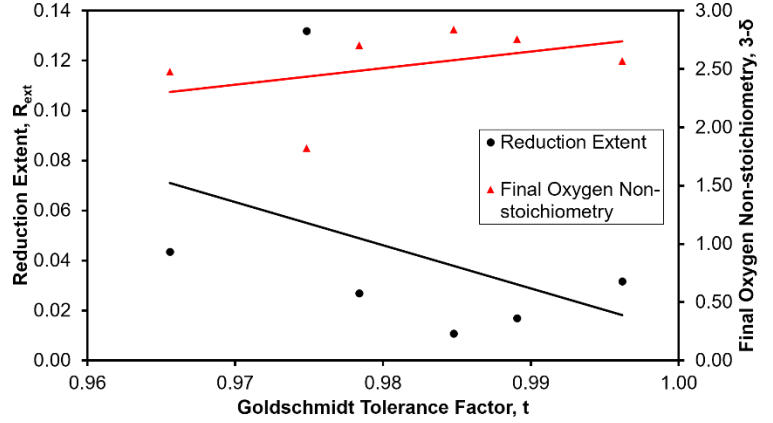


Figure 66. Reduction extent and final oxygen non-stoichiometry versus the Goldschmidt tolerance factor for samples with the same B –site composition at 900 °C.

the increase in the amount of oxygen released per gram of perovskite sample.

Similarly, R_{ext} and $3-\delta$ versus t are plotted for samples with the same A –site composition in Figure 67 and Figure 68. At both 800 and 900 °C, R_{ext} decreases and $3-\delta$ increases with an increase t .

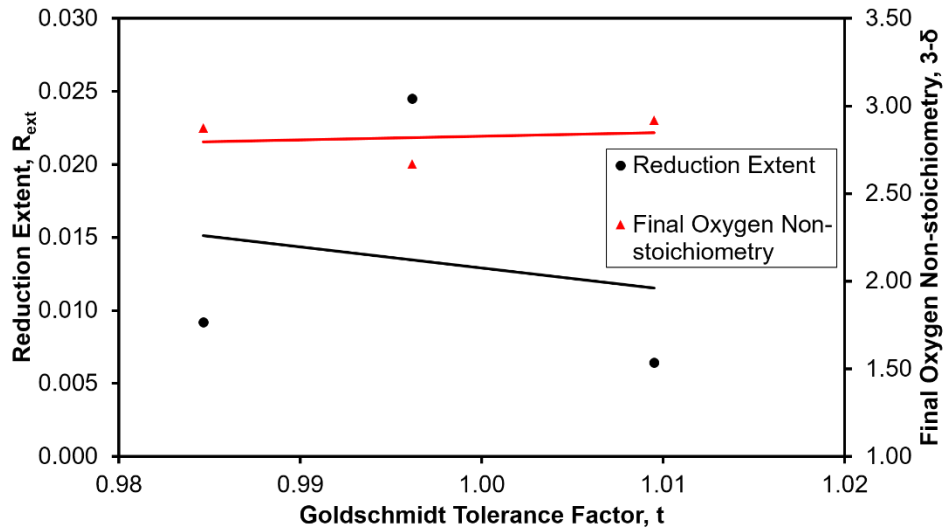


Figure 67. Reduction extent and final oxygen non-stoichiometry versus the Goldschmidt tolerance factor for samples with the same A –site composition at 800 °C.

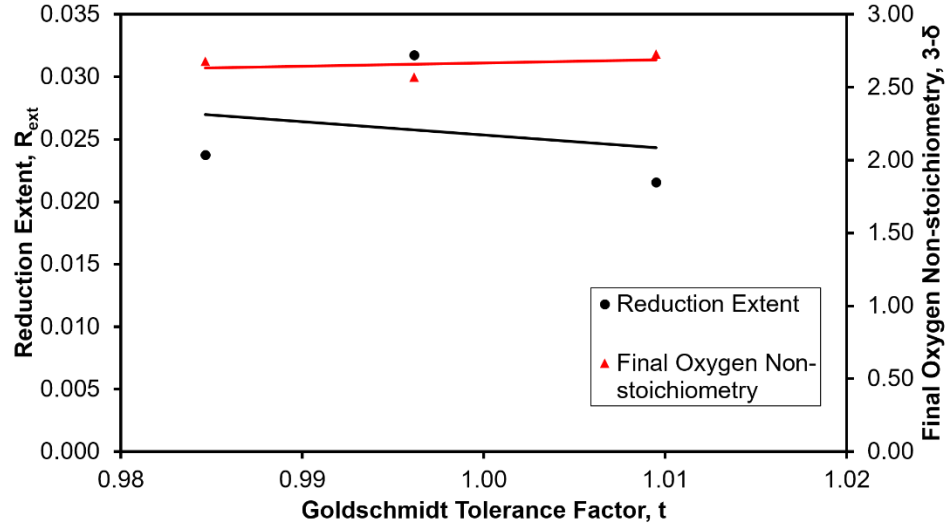


Figure 68. Reduction extent and final oxygen non-stoichiometry versus the Goldschmidt tolerance factor for samples with the same A-site composition at 900 °C.

Likewise, R_{ext} and $3-\delta$ versus t are plotted for the $\text{La}_{1-x}\text{Sr}_x\text{MnO}_3$ perovskite family with x

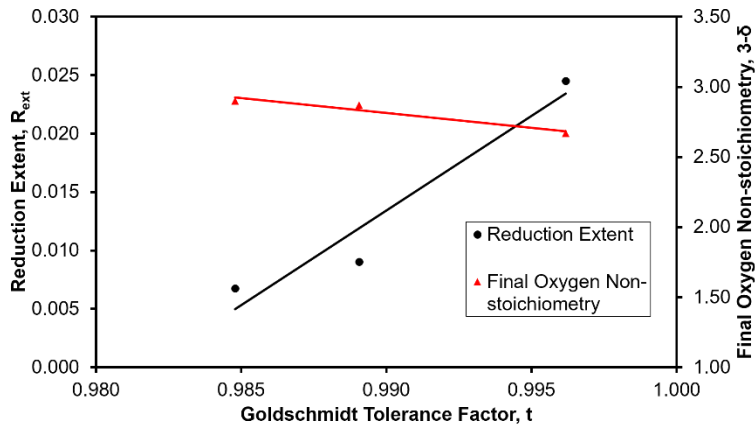


Figure 69. Reduction extent and final oxygen non-stoichiometry versus the Goldschmidt tolerance factor for LSM, LSM7525 and LSM9010 800 °C.

$x = 0.1, 0.25$ and 0.50 . In Figure 69 it shown that at 800 °C, R_{ext} increases and $3-\delta$ decreases as t approaches 1. This is in contradiction to the trend that was observed

in Figure 63, Figure 64, Figure 65, Figure 66, Figure 67 and

Figure 68.

In Figure 70 it is also observed that at 900 °C, R_{ext} increases and $3-\delta$ decreases as t approaches the value of 1.

The two parameters that are usually considered for describing the relationship between the

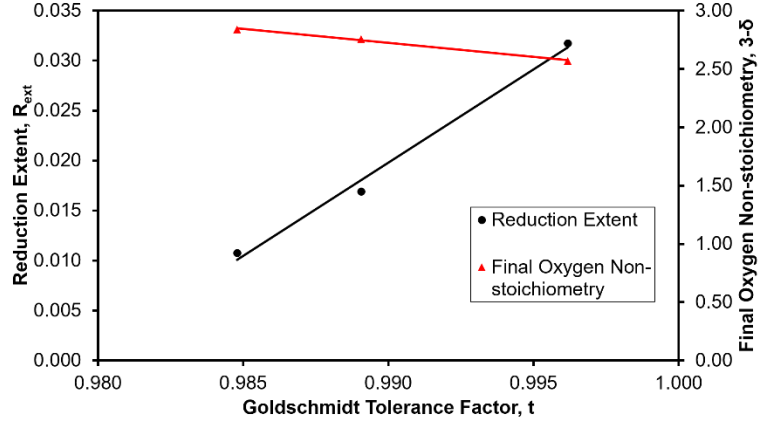


Figure 70. Reduction extent and final oxygen non-stoichiometry versus the Goldschmidt tolerance factor for LSM, LSM7525 and LSM9010 900 °C.

composition, structure and properties of perovskites are the oxidation state of the transition metal and the tolerance factor [57]. In section 3.4.1 of this thesis it was mentioned that the oxidation state of the redox active metal Mn in CM is +4. Whereas, the oxidation state of Mn in YSM, LSM and LCM is +3.5. The higher oxidation state of Mn in CM resulted in a superior reduction extent than in the case of YSM, LSM and LCM. The points that are plotted in Figure 63, Figure 64, Figure 65 and Figure 66 are associated to different perovskite samples with Mn existing in various oxidation states. Thus, in order to elucidate the impact of just the Goldschmidt tolerance factor (t) on R_{ext} and $3-\delta$, the graphs of R_{ext} and $3-\delta$ versus t values only for perovskite samples having Mn with the same oxidation states are plotted in Figure 71 and Figure 72. At 800 °C, both R_{ext} and $3-\delta$ decreases as the values of t decreases from 1 (Figure 71). The trend that is observed for R_{ext} in Figure 71 is in contradiction to the trend that was observed in Figure 63, Figure 64, Figure 65, Figure 66, Figure 67 and Figure 68. However, at 900 °C, R_{ext} increases and $3-\delta$ decreases as the values of t decreases from 1 (Figure 72). The trends observed for both R_{ext} and $3-\delta$ in Figure 72 is in agreement to the results obtained in Figure 63, Figure 64, Figure 65, Figure 66, Figure 67 and Figure 68.

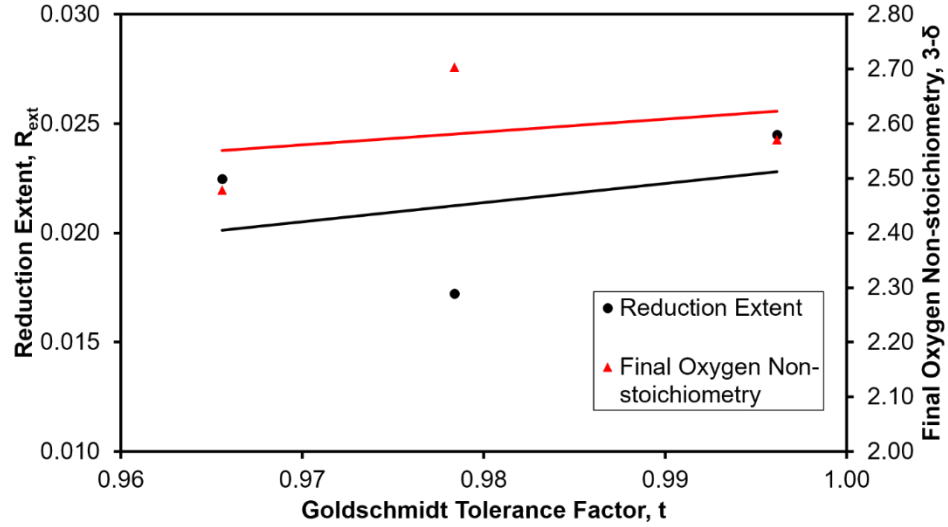


Figure 71. Reduction extent and final oxygen non-stoichiometry versus the Goldschmidt tolerance factor for samples having Mn with the same oxidation states at 800 °C.

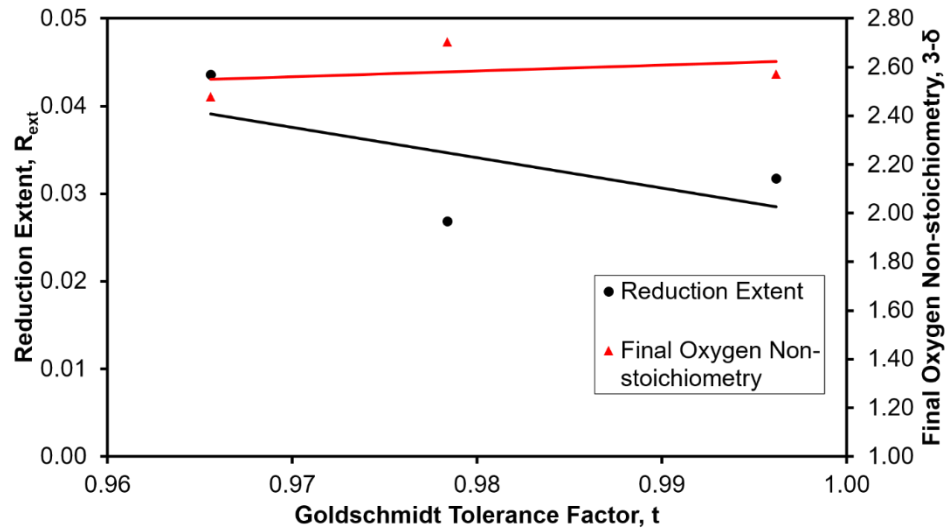


Figure 72. Reduction extent and final oxygen non-stoichiometry versus the Goldschmidt tolerance factor for samples having Mn with the same oxidation states at 900 °C.

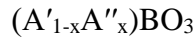
Perovskites are not completely ionic compounds and the computation of the Goldschmidt tolerance factor depends on the value of the ionic radii of the A –site metal, B –site metal and Oxygen [55]. Moreover, the values of the ionic radii depend on the coordination number of the metals and oxygen [102]. Since, the coordination number can vary

depending on the structure of the perovskite, the Goldschmidt tolerance factor calculated is only an approximation [55], [59]. In addition, it was shown in this current study that discrepancies exist in the trend of R_{ext} and $3-\delta$ as t is varied. Thus, these findings suggest that the Goldschmidt tolerance factor may not be a suitable parameter to explain the various performances of the perovskite samples investigated in this current study.

4.2. Size Variance

In section 3.4.5.1 of this thesis it was highlighted that the oxidation state of the transition metal and the tolerance factor are the two parameters that are typically used for describing the relationship between the composition, structure and properties of perovskites [57]. Research work carried out regarding manganite-based perovskites have shown that the aforementioned two parameters are insufficient to describe their properties [57]. One of the parameters that has been often overlooked in this area of research is the disorder in the structure of perovskite due to the difference in the individual A –site cationic radii [57].

The disorder in the structure of the perovskite caused by the random distribution of A –site cations with different radii is quantified using the statistical variance of the A –site cation radius distribution (σ^2) [57], [60], [61]. Perovskites with two different cations in the A –site can be represented as:



Where, A' is a trivalent lanthanide cation and A'' is a divalent alkaline earth cation. For the $(A'_{1-x}A''_x)BO_3$ perovskite, the statistical variance of the A –site cation radius distribution or the A –site cation size variance (σ^2) can be computed using the formula [57]:

$$\sigma^2 = x(1 - x)(\Delta_A)^2 \quad (14)$$

Where Δ_A is the difference between the ionic radii of the A' and A'' cations. Studies performed by *Rodriguez-Martinez et al.* have shown that both the ferromagnetic-metal-paramagnetic-insulator transition temperature and the Curie temperature of manganese-based perovskites decreases linearly with the size variance [60], [61]. Thus, in

this present study we decided to investigate the effect of the A –site cation size variance (σ^2) on the reduction extent (R_{ext}) and the final oxygen non-stoichiometry ($3-\delta$).

Initially the A –site cation size variance (σ^2) for the samples LSM, LSM7525, LSM9010, LCM and YSM was calculated using equation 15. LSM, LSM7525, LSM9010, LCM and YSM all have a trivalent lanthanide cation and divalent alkaline earth cation in the A –site as well as only Mn in the B –site. In Figure 73, R_{ext} and $3-\delta$ versus σ^2 are plotted for all the samples with only Mn in the B –site at 800 °C. Similarly in Figure 74, R_{ext} and $3-\delta$ versus σ^2 are plotted for all the samples with only Mn in the B –site at 900 °C. It is clear from both Figure 73 and Figure 74 that as σ^2 increases, R_{ext} increases and $3-\delta$ decreases. According to *Rodriguez-Martinez et al.* the structural disorder caused by the random distribution of A –site cations with different radii randomly shifts oxide ions away from their mean crystallographic positions [60]. Therefore, increase in σ^2 further displaces the oxide ions from their average crystallographic position and enhances the ability of the perovskite to release oxygen.

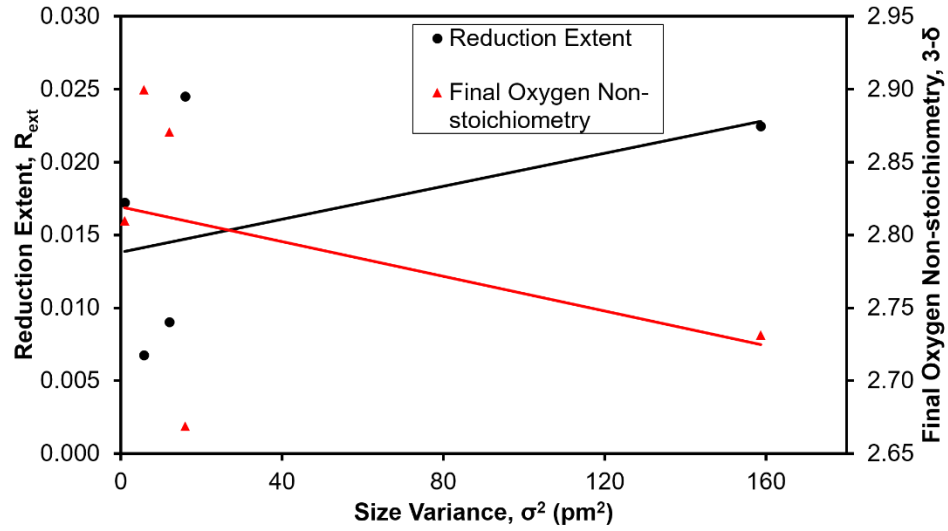


Figure 73. Reduction extent and final oxygen non-stoichiometry versus A-site cation size variance for samples having Mn in the B-site at 800 °C.

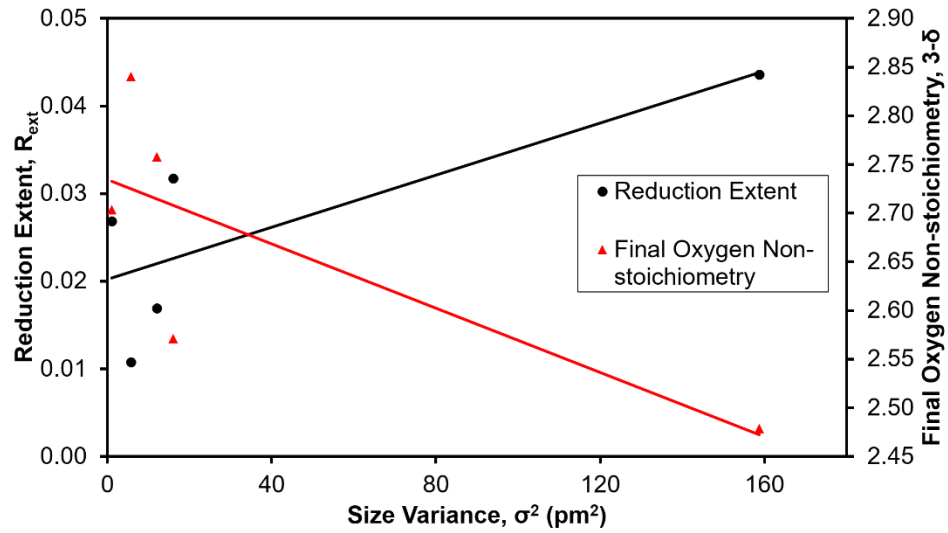


Figure 74. Reduction extent and final oxygen non-stoichiometry versus A-site cation size variance for samples having Mn in the B-site at 900 °C.

R_{ext} and $3-\delta$ versus σ^2 are plotted for the $\text{La}_{1-x}\text{Sr}_x\text{MnO}_3$ perovskite family with $x = 0.1, 0.25$ and 0.50 . According to equation 16, for the $\text{La}_{1-x}\text{Sr}_x\text{MnO}_3$ perovskite family, the A-site cation size variance (σ^2) and ultimately the structural disorder is maximum when $x = 0.5$

[57]. Thus, between LSM, LSM7525 and LMS9010, LSM has the greatest σ^2 and LSM9010 has the least σ^2 . It is evident from Figure 75 and Figure 76 that for the $\text{La}_{1-x}\text{Sr}_x\text{MnO}_3$ perovskite family, as σ^2 increases, R_{ext} increases and

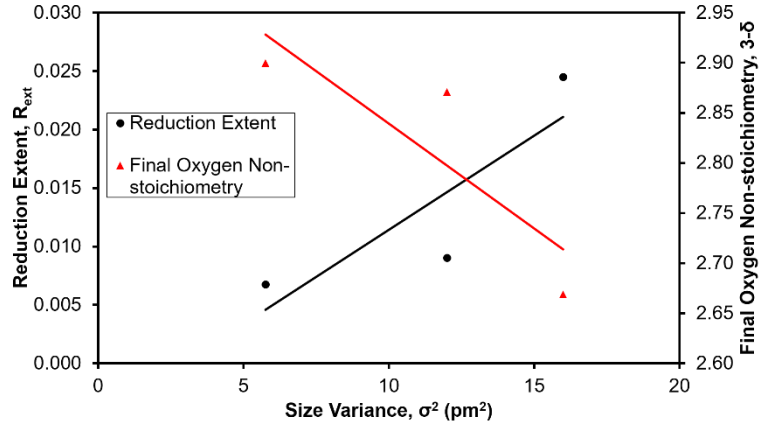


Figure 75. Reduction extent and final oxygen non-stoichiometry versus the A-site cation size variance for LSM, LSM7525 and LSM9010 at 800 °C.

$3-\delta$ decreases at both 800 and 900 °C. This is in agreement with the trends observed in

Figure 73 and Figure 74.

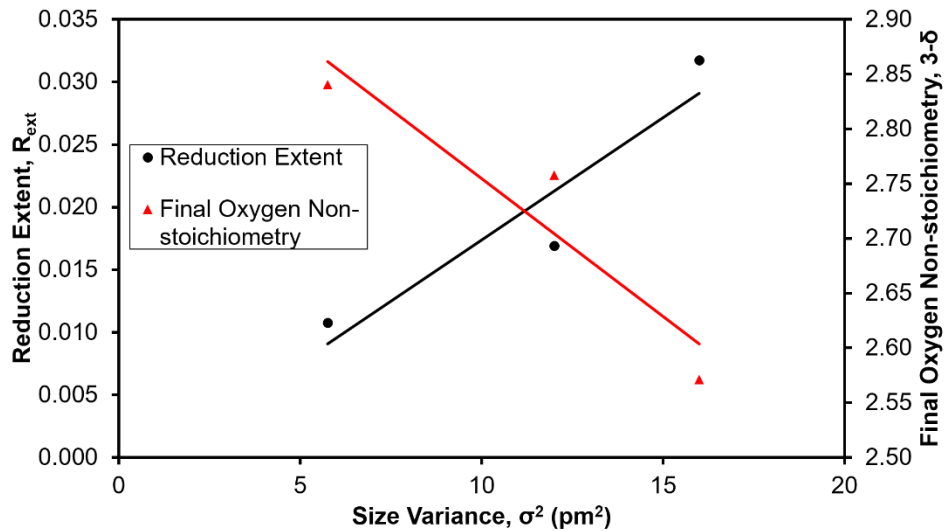


Figure 76. Reduction extent and final oxygen non-stoichiometry versus the A-site cation size variance for LSM, LSM7525 and LSM9010 at 900 °C.

Despite the fact that LSM, LSM7525, LSM9010, LCM and YSM all have Mn in the B – site, the oxidation state of Mn in LSM7525 and LSM9010 is different than that in LSM, LCM and YSM. Nevertheless, LSM, LCM and YSM have Mn in the same oxidation state. Hence a separate graph of R_{ext} and $3-\delta$ versus σ^2 are plotted only for LSM, LCM and YSM. In Figure 77, R_{ext} and $3-\delta$ versus σ^2 are plotted for LSM, LCM and YSM at 800 °C. Similarly in Figure 78, R_{ext} and $3-\delta$ versus σ^2 are plotted for LSM, LCM and YSM at 900 °C. At both 800 and 900 °C, R_{ext} increases and $3-\delta$ decreases as σ^2 increases for samples with Mn in the same oxidation state. This trend is consistent with the trends observed in Figure 73, Figure 74, Figure 75 and Figure 76. However, from Figure 77 and Figure 78, R_{ext} strongly increases and $3-\delta$ strongly decreases with increase in σ^2 at 900 °C than at 800 °C.

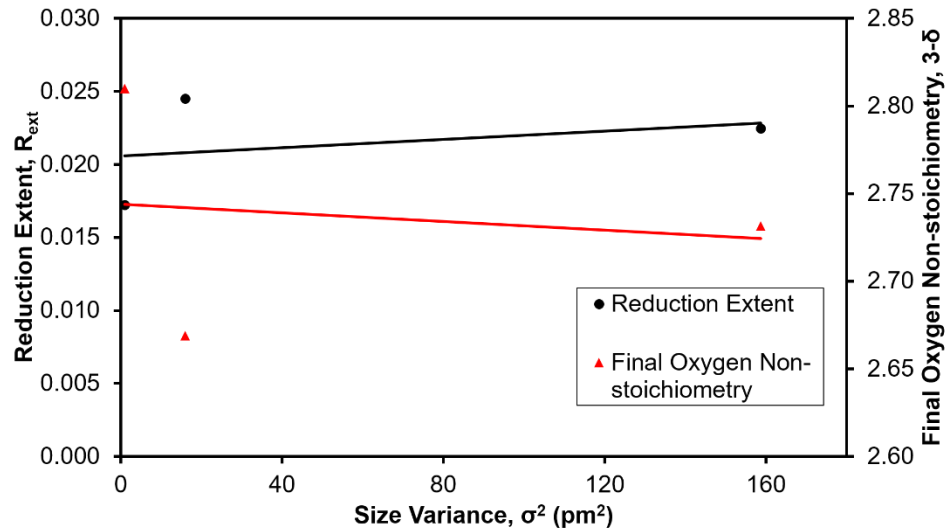


Figure 77. Reduction extent and final oxygen non-stoichiometry versus the A –site cation size variance for samples having Mn with the same oxidation state at 800 °C.

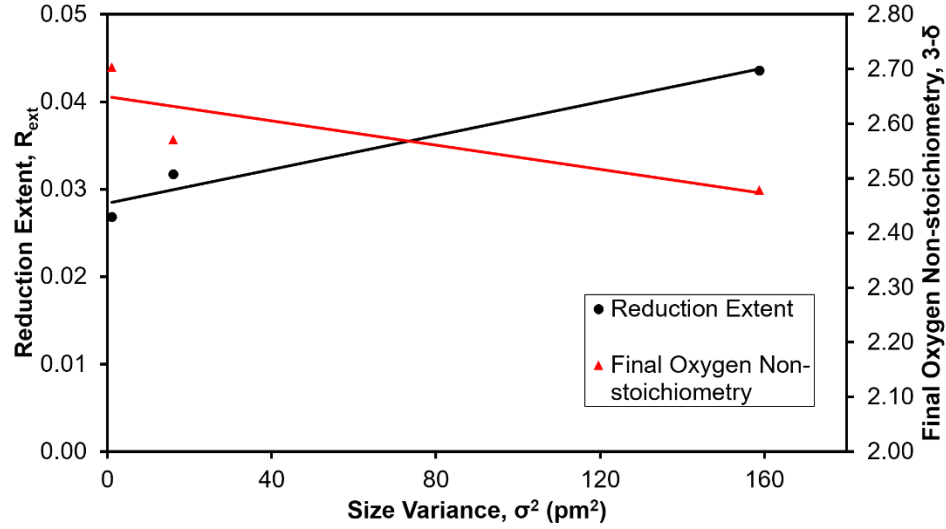


Figure 78. Reduction extent and final oxygen non-stoichiometry versus the A-site cation size variance for samples having Mn with the same oxidation state at 900 °C.

In contrast to the irregular trends observed in the plot of R_{ext} and $3-\delta$ versus t , the trends observed in the plot of R_{ext} and $3-\delta$ versus σ^2 are consistent. This could suggest that σ^2 might have a greater impact on R_{ext} and $3-\delta$ than t for the perovskite samples investigated in the current study. Also, the consistent results obtained in Figure 73, Figure 74, Figure 75, Figure 76, Figure 77 and Figure 78 further support the point that for the perovskite samples investigated, larger values of σ^2 signify greater random displacement of the oxide ions from their mean crystallographic position. Hence, the ability of the perovskites to release oxygen increases with increasing values of σ^2 .

4.3. Electronegativity Difference Between Oxygen and A and B -site Cations

The other factor considered in the present investigation that could be affecting R_{ext} and $3-\delta$ is the electronegativity difference between oxygen and the A and B –site cations. According to the definition provided by Dr. Michael Blaber “*Electronegativity is defined as the ability of an atom in a particular molecule to attract electrons to itself*” [103]. Thus, higher the metal-oxygen electronegativity difference in a perovskite oxide, the greater the ability of the oxygen atom to pull the electrons away from the metals. *Liu et al.* obtained an inverted volcano plot when the oxygen non-stoichiometry of perovskite oxides versus the electronegativity of the B –site cation was plotted [62]. Similarly, *Wang et al.* illustrated a linear relationship between the metal-oxygen electronegativity difference in lanthanum-based perovskites and the ignition temperature [63]. Therefore, in the present study the effect of metal-oxygen electronegativity difference on R_{ext} and $3-\delta$ is investigated.

Initially, for the perovskite samples with only Mn in the B –site R_{ext} and $3-\delta$ versus A –site metal and oxygen electronegativity difference is plotted. For the samples with both lanthanide cation and alkaline earth cation in the A –site, the A –site electronegativity was computed as a weighted average of the electronegativity of the lanthanide cation and alkaline earth cation. R_{ext} and $3-\delta$ versus A –site metal and oxygen electronegativity difference at 800 and 900 °C are plotted in Figure 79 and Figure 80 respectively. At both the temperatures, R_{ext} increases and $3-\delta$ decreases as the A –site metal and oxygen electronegativity difference increases.

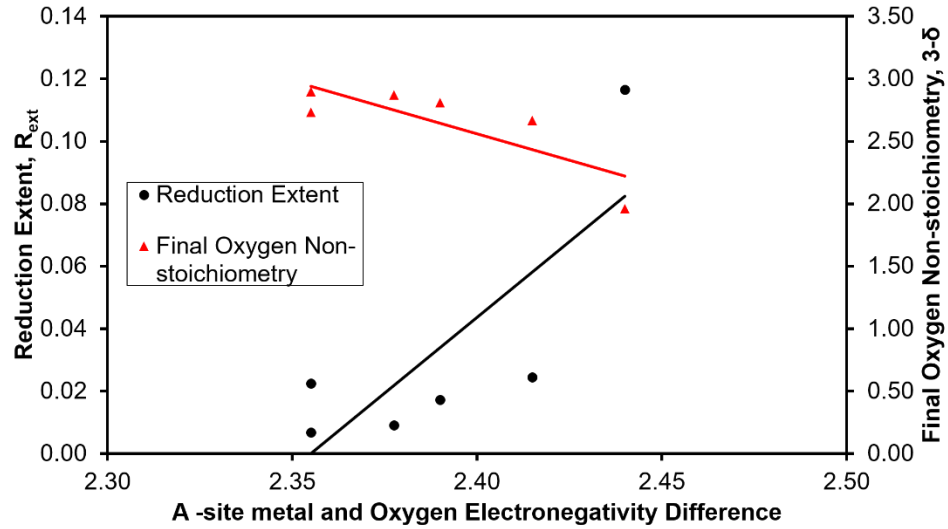


Figure 79. Reduction extent and final oxygen non-stoichiometry versus the A –site metal and oxygen electronegativity difference for samples having Mn in the B –site at 800 °C.

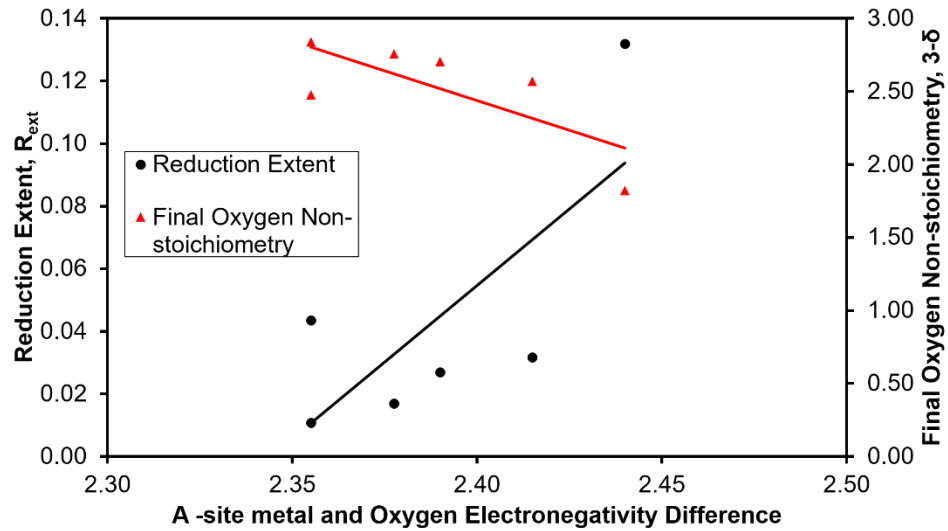


Figure 80. Reduction extent and final oxygen non-stoichiometry versus the A –site metal and oxygen electronegativity difference for samples having Mn in the B –site at 900 °C.

Similarly, R_{ext} and $3-\delta$ versus B –site metal and oxygen electronegativity difference is plotted for samples with the same A –site composition. For samples with two different cations in the B –site, the electronegativity of the B –site is calculated as the weighted

average of the two B –site cations. As illustrated in Figure 81, at 800 °C R_{ext} increases and

$3-\delta$ decreases with increase in the B –site metal and oxygen electronegativity difference.

Likewise, as shown in Figure 82, at 900 °C R_{ext} increases and $3-\delta$ decreases with increase in the B

–site metal and oxygen electronegativity difference. The

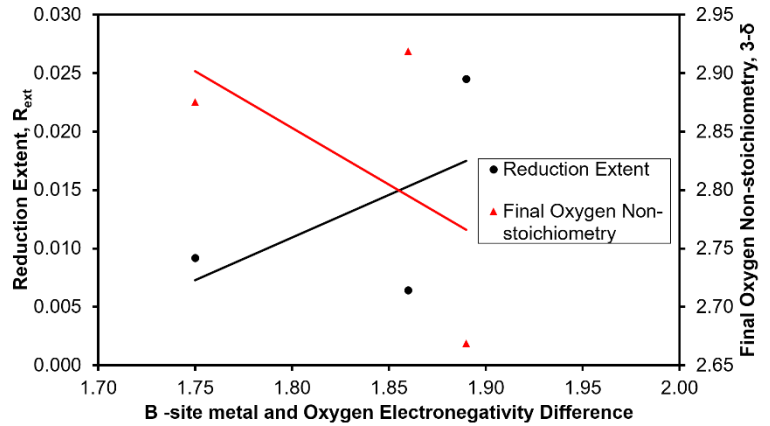


Figure 81. Reduction extent and final oxygen non-stoichiometry versus the B –site metal and oxygen electronegativity difference for samples having the same A –site composition at 800 °C.

trends observed in Figure 81 and Figure 82 coincides with the trends observed in Figure 79 and Figure 80.

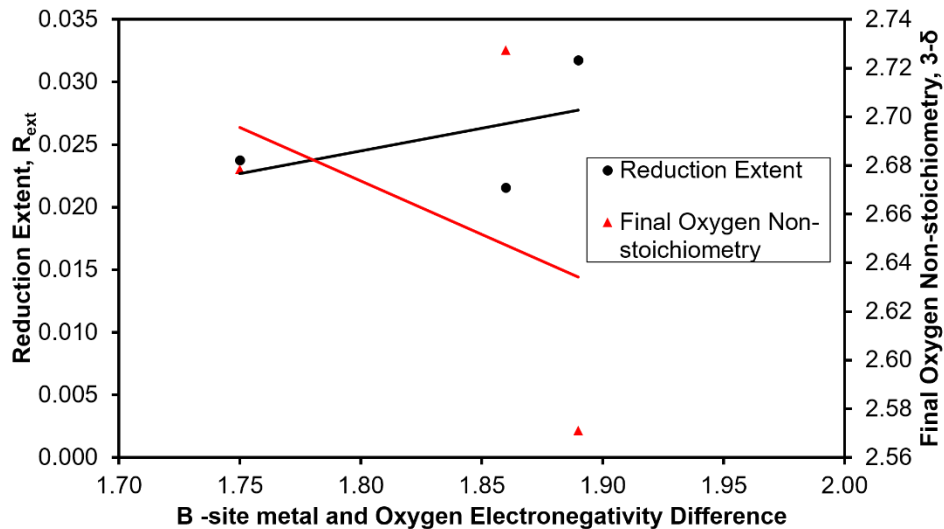


Figure 82. Reduction extent and final oxygen non-stoichiometry versus the B –site metal and oxygen electronegativity difference for samples having the same A –site composition at 900 °C.

Clear and consistent trends in the plot of R_{ext} and $3-\delta$ versus metal-oxygen electronegativity difference are observed in Figure 79, Figure 80, Figure 81 and Figure 82. However, the effect

of metal-oxygen electronegativity difference on R_{ext} and $3-\delta$ cannot be viewed in isolation. For instance, even though fluorine is more electronegative than chlorine, hydrochloric acid is more stronger than hydrofluoric acid [103], [104].

4.4. Metal-Oxygen Bond Strength

Metal-oxygen bond strength is the fourth factor considered for affecting R_{ext} and $3-\delta$. The reduction of the perovskite involves the release of oxygen from its surface [64]. Thus, the metal-oxygen bond strength or the binding energy of surface oxygen to the metals could play a vital role during the reduction of the perovskite sample. *Voorhoeve et al.*, *Murali Dhar et al.* and *Futai et al.* all showed that the catalytic activity of perovskites increased with decrease in metal-oxygen bond strength or binding energy of surface oxygen [54], [64]–[66]. Therefore, the effect of metal-oxygen bond strength or binding energy of surface oxygen on R_{ext} and $3-\delta$ is investigated in the present study.

The metal-oxygen bond strength or binding energy of surface oxygen is calculated using the formula [64]–[66]:

$$M - O = \frac{1}{c_n m} \left(\Delta H_f - m \Delta H_s - \frac{n}{2} D_o \right) \quad (15)$$

Where, $M - O$ is the metal-oxygen bond strength, ΔH_f is the enthalpy of formation for one mole of $M_m O_n$, ΔH_s is the heat of sublimation of the metal (M), D_o is the bond dissociation energy for one mole of O_2 and C_n is the coordination number of metal ions. The formula for the metal-oxygen bond strength presented in equation 15 is derived by applying Hess's law to the Born-Haber cycle [105]–[107]. The Born-Haber cycle for the computation of La-O bond strength in perovskites with La in the A –site is illustrated in Figure 83. In Figure 83, initially La and O_2 are in their standard states. Then applying the heat of sublimation (ΔH_s), La in solid state is converted into La in gaseous state. Simultaneously, heat of dissociation (D_o) is applied to break the O-O bond of the O_2 molecule. The purpose of converting La into gaseous state and breaking the O-O bond is to create a state where there

is no La-La and O-O interactions. Eventually, La in the gaseous state and isolated O atoms are allowed interact forming La_2O_3 (s). The difference in energy between $2 \text{La}_{(g)} + 3 \text{O}_{(g)}$ state and La_2O_3 (s) state is 2×12 (La – O) because La_2O_3 (s) exists within the perovskite compound and the coordination number of La within the perovskite is 12. The enthalpy of formation (ΔH_f) for one mole of La_2O_3 (s) has been reported in literature [108]. By applying Hess's law to Born-Haber cycle in Figure 83, the following is obtained:

$$\Delta H_f = 2 \times \Delta H_s + \frac{3}{2}D_O + 2 \times 12 (La - O) \quad (16)$$

By rearranging equation 16,

$$(La - O) = \frac{1}{2 \times 12} \left(\Delta H_f - 2 \times \Delta H_s - \frac{3}{2}D_O \right) \quad (17)$$

By comparing equations 15 and 17 it is clear that, equation 17 is in the form presented in equation 15.

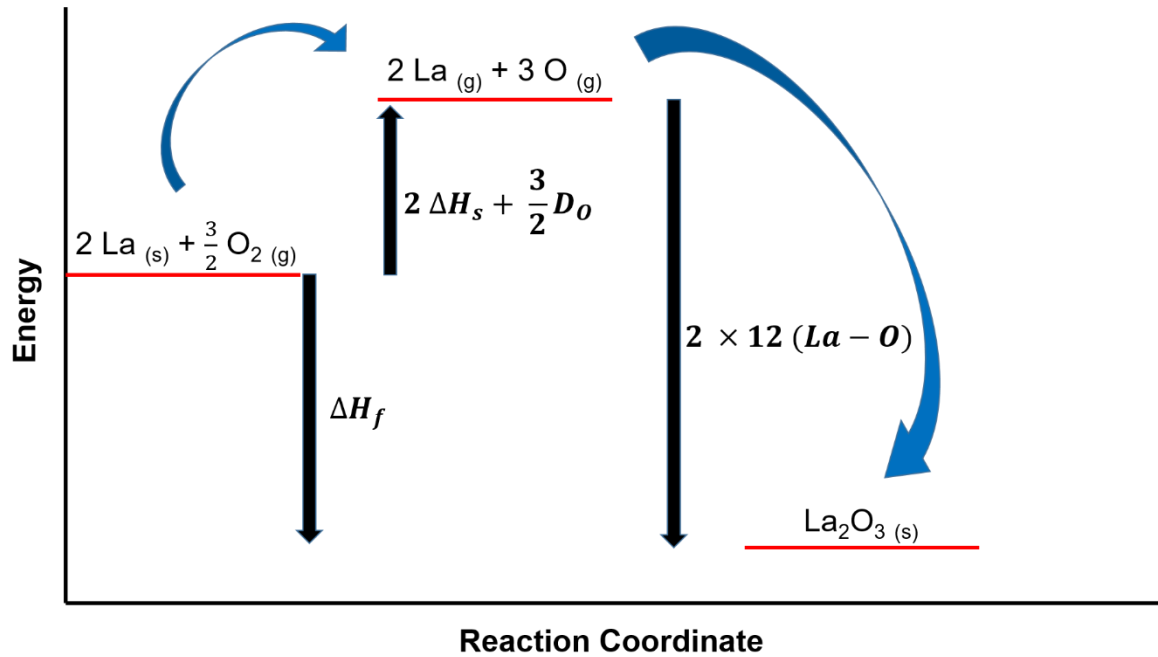


Figure 83. Born-Haber cycle for the computation of La-O bond strength in perovskite with La in the A-site.

Similarly, other metal-oxygen bond strengths were evaluated using the same procedure outlined for La-O. Initially, R_{ext} and $3-\delta$ versus A-site metal-oxygen bond strength for samples with Mn in the B-site is plotted at 800 and 900 °C in Figure 84 and Figure 85 respectively.

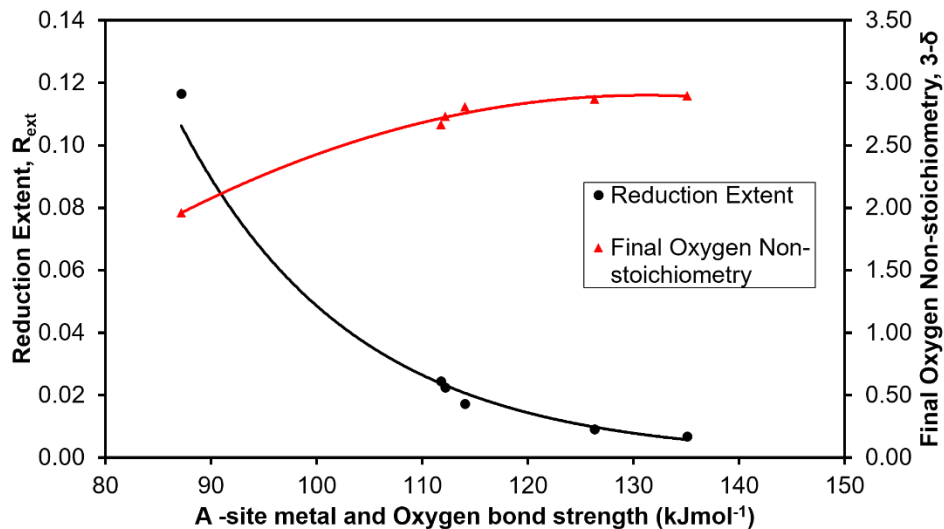


Figure 84. Reduction extent and final oxygen non-stoichiometry versus A-site metal-oxygen bond strength for samples with Mn in the B-site at 800 °C.

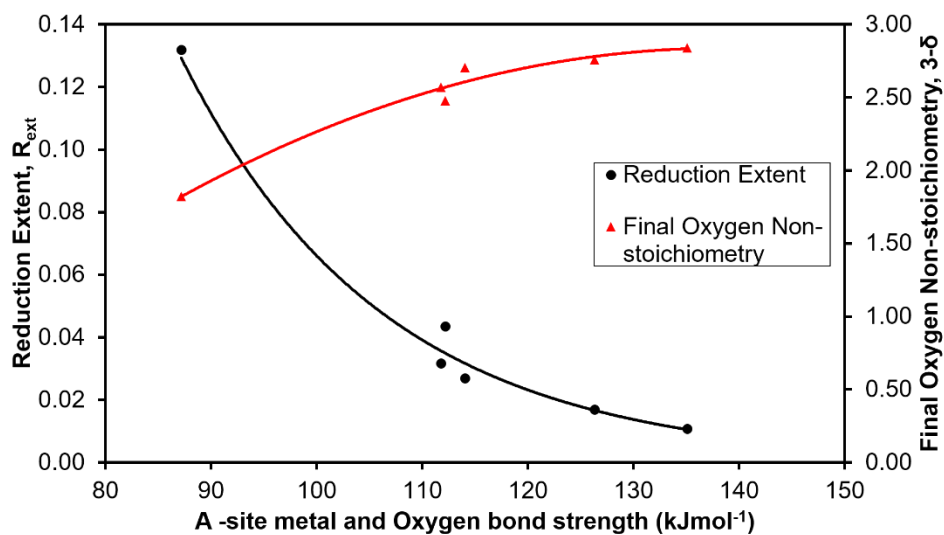


Figure 85. Reduction extent and final oxygen non-stoichiometry versus A-site metal-oxygen bond strength for samples with Mn in the B-site at 900 °C.

For perovskite samples with both lanthanide cation and alkaline earth cation in the A-site, first the lanthanide metal-oxygen and alkaline earth metal-oxygen bond strengths were separately computed. Then for the total A-site metal-oxygen bond strength a weighted

average of the lanthanide metal-oxygen and alkaline earth metal-oxygen bond strengths was evaluated. It is apparent from Figure 84 and Figure 85 that at both 800 and 900 °C, R_{ext} decreases and $3-\delta$ increases as the A –site metal-oxygen bond strength increases. In other words, for the perovskite samples investigated in this study with Mn in the B –site, the catalytic activity increases with decrease in the A –site metal-oxygen bond strength.

Likewise, R_{ext} and $3-\delta$ versus B –site metal-oxygen bond strength for samples with the same A –site composition is

plotted at 800 and 900 °C in Figure 86 and Figure 87 respectively. For the perovskite samples with two different metals in the B –site, the metal-oxygen bond strength was calculated for each of the B –site

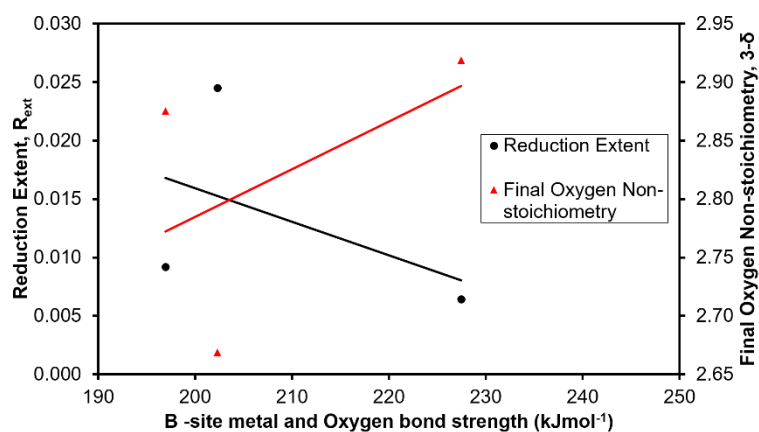


Figure 86. Reduction extent and final oxygen non-stoichiometry versus B –site metal-oxygen bond strength for samples with the same A –site composition at 800 °C.

metal separately. The total B –site metal-oxygen bond strength was then computed as the weighted average of the two B –site metal-oxygen bond strengths. At both 800 and 900 °C, R_{ext} decreases and $3-\delta$ increases as the B –site metal-oxygen bond strength increases. Thus, for the perovskite samples investigated in the present study with the same A –site composition, the catalytic activity increases with decrease in the B –site metal-oxygen bond strength.

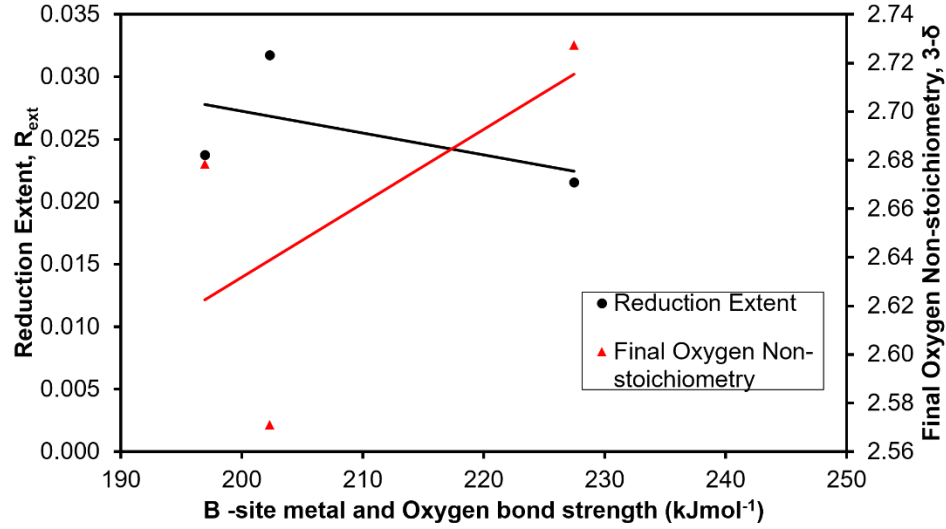


Figure 87. Reduction extent and final oxygen non-stoichiometry versus B-site metal-oxygen bond strength for samples with the same A-site composition at 900 °C.

For the $\text{La}_{1-x}\text{Sr}_x\text{MnO}_3$ perovskite family with $x = 0.1, 0.25$ and 0.50 , R_{ext} and $3-\delta$ versus A

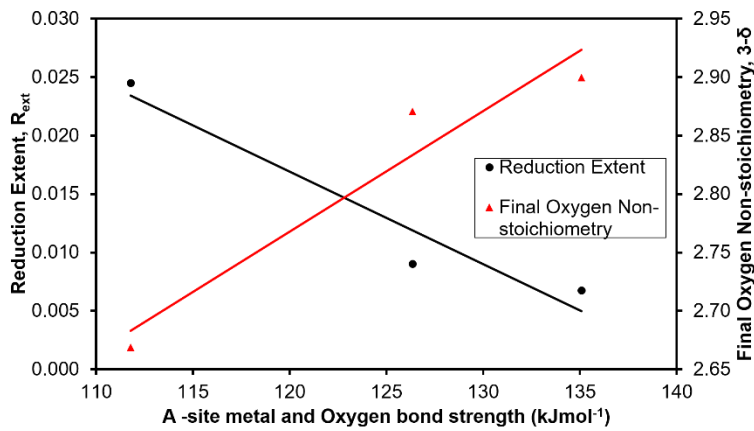


Figure 88. Reduction extent and final oxygen non-stoichiometry versus A-site metal-oxygen bond strength for LSM, LSM7525 and LSM9010 at 800 °C.

–site metal-oxygen bond strength is plotted at 800 and 900 °C in Figure 88 and Figure 89 respectively. The A-site metal-oxygen bond strength decreases with increase in strontium

content. It is evident from both Figure 88 and Figure 89 that the catalytic activity for the $\text{La}_{1-x}\text{Sr}_x\text{MnO}_3$ perovskite family increases with decrease in the metal-oxygen bond strength.

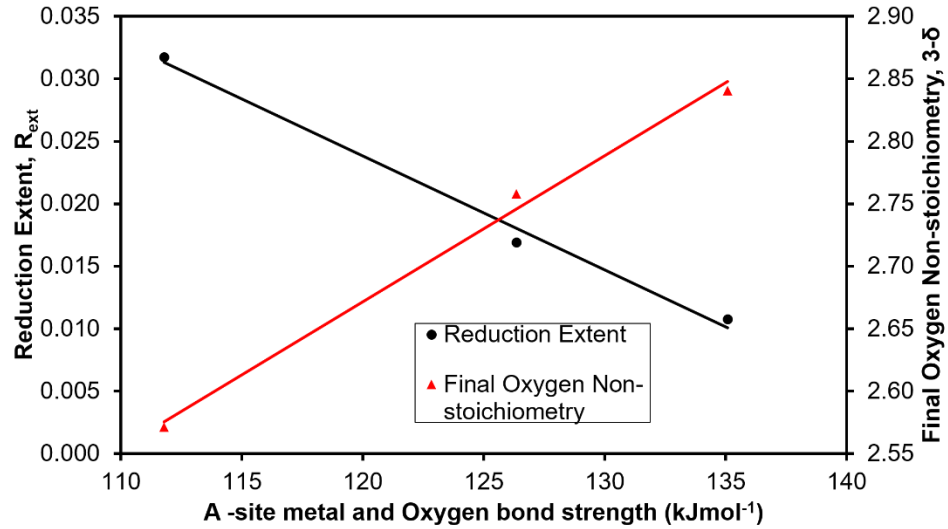


Figure 89. Reduction extent and final oxygen non-stoichiometry versus A –site metal-oxygen bond strength for LSM, LSM7525 and LSM9010 at 900 °C.

Lastly, R_{ext} and $3-\delta$ versus A –site metal-oxygen bond strength is plotted for samples having Mn with the same oxidation state in Figure 90 and Figure 91. As illustrated in Figure 90 and Figure 91, at both 800 and 900 °C, R_{ext} decreases and $3-\delta$ increases with increase in A –site metal-oxygen bond strength. The catalytic activity increases for samples having Mn with the same oxidation state as the A –site metal-oxygen bond strength decreases.

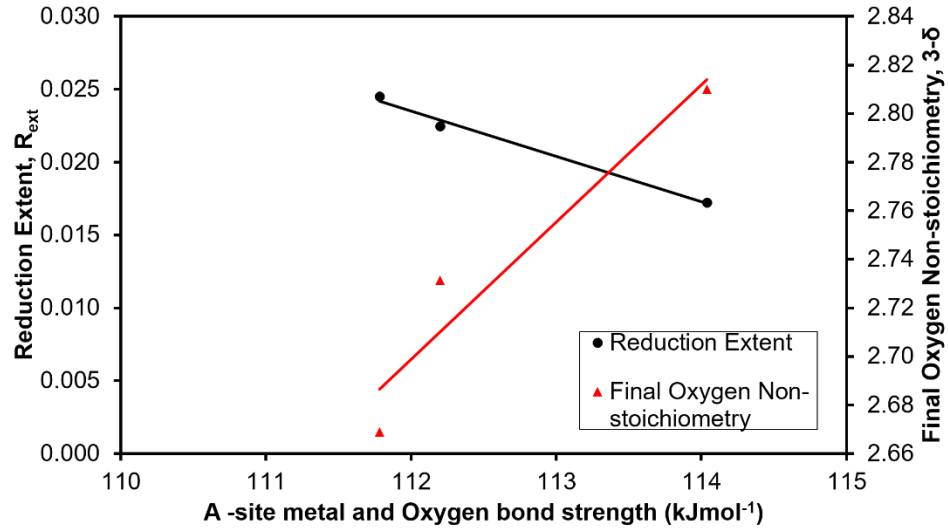


Figure 90. Reduction extent and final oxygen non-stoichiometry versus A-site metal-oxygen bond strength for the samples having Mn with the same oxidation state at 800 °C.

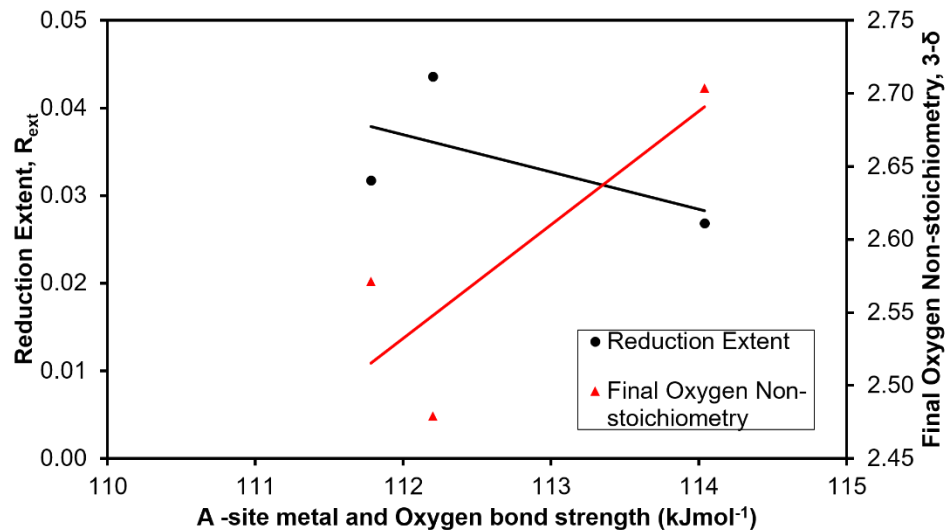


Figure 91. Reduction extent and final oxygen non-stoichiometry versus A-site metal-oxygen bond strength for the samples having Mn with the same oxidation state at 900 °C.

It can be observed from Figure 84, Figure 85, Figure 86, Figure 87, Figure 88, Figure 89, Figure 90 and Figure 91 that the trend in the plot of R_{ext} and $3-\delta$ versus metal-oxygen bond strength is clear and consistent. The metal-oxygen bond strength is one of the factors investigated

that is suitable to explain the trends in the performances of the perovskite samples studied in the present research.

CHAPTER FIVE: CONCLUSION AND RECOMMENDATIONS

5.1. Conclusion

Initially the redox performances of CM, LCM, YSM and LSM were investigated at 700, 800 and 900 °C for three cycles using a Thermogravimetric Analyzer (TGA) to evaluate the effect of A –site substitution. Methane was used as a reducing agent during the reduction of the perovskite samples and CO₂ was used as an oxidizing agent during the re-oxidation phase. Since the reduction of the perovskite samples is an endothermic process, the reduction extent increased with temperature. Out of the four samples, CM displayed the greatest reduction extent at all the temperatures followed by YSM, LSM and LCM. For instance, at 900 °C, during the first redox cycle CM, YSM, LSM and LCM produced 4122, 1362, 992 and 840 μmolg^{-1} O₂ respectively. One of the reason for CM having the greatest reduction extent is that the oxidation state of Mn in CM is +4, whereas the oxidation state of Mn in YSM, LSM and LCM is +3.5. However, the stability of CM was the poorest. At 900 °C, CM could not be re-oxidized during the first cycle. Upon inspection, the color of the CM sample turned into white or light grey from black after the redox cycles. This verified the formation of carbonates. The trend in the performance of YSM, LSM and LCM is explained by the statistical variance of the A –site cation radius distribution or the A –site cation size variance (σ^2). YSM has the largest σ^2 followed by LSM and LCM. XRD analysis after three cycles at 900 °C reveal the formation of SrCO₃ peaks in the case of YSM but the peaks are absent for LSM. All these results suggested that LSM is the best performing sample amongst CM, YSM, LSM and LCM.

The family of $\text{La}_{1-x}\text{Sr}_x\text{MnO}_3$ ($x = 0.5, 0.25, 0.10$) was further investigated to find an optimal A-site composition. N_2 physisorption results showed that LSM, LSM7525 and LSM9010 have the same BET surface area. However, SEM images show that the crystallite size decreases with increasing Sr content. The TGA results show that during the redox cycling, LSM displays the greatest activity followed by LSM7525 and LSM9010. At 900 °C, during the first redox cycle LSM, LSM7525 and LSM9010 produce 992, 529 and 337 $\mu\text{molg}^{-1} \text{O}_2$ respectively. Similarly, in the first cycle at 900 °C, LSM, LSM7525 and LSM9010 produce 1813, 857 and 307 $\mu\text{molg}^{-1} \text{CO}$ respectively. The oxidation states of Mn in LSM, LSM7525 and LSM9010 are +3.5, +3.25 and +3.10 respectively. This means that LSM has the greatest amount of Mn^{4+} species followed by LSM7525 and LSM9010. After the first redox cycle the activity decreases for LSM, LSM7525 and LSM9010. However, the activity becomes stable during the second and third cycle. XRD results after the three redox cycles did not show any carbonate or impurity peaks for all the samples. SEM images showed sintering. Sintering and powder densification could be the possible reasons for the decrease in activity after the first cycle but its effect is not significant after first redox cycle. More Sr content results in higher σ^2 , which corresponds to greater reduction extent. In addition, the intrinsic kinetic parameters such as activation energy for the reduction of LSM, LSM7525 and LSM9010 was evaluated using a shrinking grain model. LSM, LSM7525 and LSM9010 have activation energy values of 44, 49, 54 kJmol^{-1} respectively. Greater the Sr content, lower the activation energy for reduction of the perovskite sample was observed. EDS results showed that LSM has homogeneous distribution of Mn on its surface. But LSM9010 has regions on its surface that are devoid of Mn.

To study the effect of B –site substitution on the redox performance of the perovskite samples LSMA, LSMF and LSMA7525 were synthesized. Substituting the B –site with Al and Fe did not improve the activity nor the stability of the samples. The activity of LSMA, LSMF and LSMA7525 was reduced after first redox cycle but remained stable in the second and third cycle. XRD results after three redox cycles showed no new phase formation. EDS results showed regions on the surface of LSMA devoid of Mn. These regions were instead replaced by chunks of Al and Sr.

The redox cycling of the perovskite samples were also performed using only thermal energy during the reduction phase. The TGA results clearly show that by using CH₄ as a reduction agent, the perovskite samples were reduced to larger extent than when only thermal energy was used. For instance, at 900 °C, during the first redox cycle LSM9010 produced 337 μmolg⁻¹ O₂ using CH₄ and LSM9010 produced 153 μmolg⁻¹ O₂ using only thermal energy. When only thermal energy was used, the activation energy for the reduction of LSM9010 was computed to be 83 kJmol⁻¹. The activation energy for the reduction of LSM9010 was evaluated to be 54 kJmol⁻¹ when CH₄ was used as a reducing agent. The reduction of LSM at 900 °C using methane was able to produce 992 μmolg⁻¹ O₂ during the first redox cycle. According to literature, the LSM sample prepared using the same method as in this study, produces 256 μmolg⁻¹ O₂ during the first redox cycle at 1400 °C when only thermal energy is used [29].

Goldschmidt tolerance factor (*t*), A –site cation size variance (σ^2), metal-oxygen electronegativity difference and metal-oxygen bond strength are the four factors investigated in this study that could affect the reduction extent (R_{ext}) and remaining oxygen non-stoichiometry ($3-\delta$). Plots of R_{ext} and $3-\delta$ versus σ^2 and plots of R_{ext} and $3-\delta$ versus

metal-oxygen bond strength revealed strong and consistent relationship between R_{ext} , $3-\delta$ and σ^2 as well as between R_{ext} , $3-\delta$ and metal-oxygen bond strength. R_{ext} increases and $3-\delta$ decreases with increasing σ^2 . R_{ext} decreases and $3-\delta$ increases with increasing metal-oxygen bond strength. The plots of R_{ext} and $3-\delta$ versus t shows inconsistent results. The plots of R_{ext} and $3-\delta$ versus metal-oxygen electronegativity difference show consistent results as well. R_{ext} increases and $3-\delta$ decreases with increasing metal-oxygen electronegativity difference. However, metal-oxygen electronegativity difference cannot be examined in isolation as various factors can convolute the dependence of R_{ext} and $3-\delta$ on metal-oxygen electronegativity difference. For instance, even though F is more electronegative than Cl, HCl is a stronger acid than HF [103], [104].

Long-term stability tests for 10 cycles were performed on LSM, LSM7525, LSM9010, LSMA and LSMF to investigate the effect of carbon deposition, sintering and powder densification. Just as in the case of three redox cycles, the activity of the samples decreases after the first cycle but remains stable from the second to the tenth cycle. This suggests that the impact of carbon deposition, sintering and powder densification is not significant after the first cycle.

5.2. Recommendations

X-ray photoelectron spectroscopy (XPS) could be used to study the oxidation state of the redox active site Mn in the perovskite sample [25], [109]. XPS could also be used to detect carbonate formed during the redox cycling [25].

Long-term stability tests for more than 10 cycles should be performed in order to further investigate the impact of carbon deposition, sintering and powder densification of the perovskite samples. The redox cycling could be carried out in appropriate bench scale reactors. In addition, Raman spectroscopy could be used to further investigate the carbon deposition on the perovskite material [110]. Also, Fourier-Transform Infrared Spectroscopy (FTIR) could be used to detect the gases produced during redox cycling.

Additional perovskite samples with different A and B –site could be synthesized to obtain more data points for accurately evaluating the dependence of R_{ext} and $3-\delta$ on t , σ^2 , metal-oxygen bond strength and metal-oxygen electronegativity difference.

REFERENCES

- [1] “Voyager 1’s Pale Blue Dot,” 2019. [Online]. Available: <https://solarsystem.nasa.gov/resources/536/voyager-1s-pale-blue-dot/>. [Accessed: 10-Apr-2019].
- [2] L. Sweetlove, “Number of species on Earth tagged at 8.7 million,” *Nature*, Aug. 2011.
- [3] C. Mora, D. P. Tittensor, S. Adl, A. G. B. Simpson, and B. Worm, “How many species are there on earth and in the ocean?,” *PLoS Biol.*, vol. 9, no. 8, pp. 1–8, 2011.
- [4] F. Dorey, “Homo sapiens – modern humans,” 2018. [Online]. Available: <https://australianmuseum.net.au/learn/science/human-evolution/homo-sapiens-modern-humans/>. [Accessed: 10-Apr-2019].
- [5] “World population projected to reach 9.8 billion in 2050, and 11.2 billion in 2100,” 2017. [Online]. Available: <https://www.un.org/development/desa/en/news/population/world-population-prospects-2017.html>. [Accessed: 10-Apr-2019].
- [6] “Climate Literacy: The Essential Principles of Climate Science,” 2019. [Online]. Available: https://climate.nasa.gov/resources/education/pbs_modules/standards2/. [Accessed: 10-Apr-2019].
- [7] “Alan Watts – Everything is Interconnected & Inseparable,” 2015. [Online]. Available: <https://creativesystemsthinking.wordpress.com/2015/04/18/alan-watts-everything-is-interconnected-inseparable/>. [Accessed: 10-Apr-2019].
- [8] “Climate change: How do we know?,” 2019. [Online]. Available: <https://climate.nasa.gov/evidence/>. [Accessed: 11-Apr-2019].
- [9] “A blanket around the Earth,” 2019. [Online]. Available: <https://climate.nasa.gov/causes/>. [Accessed: 11-Apr-2019].
- [10] “Global Temperature,” 2019. [Online]. Available: <https://climate.nasa.gov/vital-signs/global-temperature/>. [Accessed: 11-Apr-2019].
- [11] “Sea Level,” 2019. [Online]. Available: <https://climate.nasa.gov/vital-signs/sea-level/>. [Accessed: 11-Apr-2019].
- [12] K. Kumari Rigaud *et al.*, “Groundswell: Preparing for Internal Climate Migration,” Washington, DC, 2018.
- [13] “How climate is changing,” 2019. [Online]. Available: <https://climate.nasa.gov/effects/>. [Accessed: 11-Apr-2019].

- [14] IEA, "Total Primary Energy Supply (TPES) by source," 2018. [Online]. Available: <https://www.iea.org/statistics/?country=WORLD&year=2016&category=Energy supply&indicator=TPESbySource&mode=chart&dataTable=BALANCES>. [Accessed: 11-Apr-2019].
- [15] R. Showstack, "World's Heavy Dependence on Fossil Fuels Projected to Continue," *Eos*, 18-Sep-2017.
- [16] M. Aresta, A. Dibenedetto, and A. Angelini, "The changing paradigm in CO₂ utilization," *J. CO₂ Util.*, vol. 3–4, pp. 65–73, 2013.
- [17] "Oxidation States of Organic Molecules," 2014. [Online]. Available: [https://chem.libretexts.org/Bookshelves/Organic_Chemistry/Supplemental_Modules_\(Organic_Chemistry\)/Fundamentals/Oxidation_States_of_Organic_Molecules](https://chem.libretexts.org/Bookshelves/Organic_Chemistry/Supplemental_Modules_(Organic_Chemistry)/Fundamentals/Oxidation_States_of_Organic_Molecules). [Accessed: 15-Apr-2019].
- [18] N. Saito, "The economic analysis of commercial ships with hydrogen fuel cell through case studies," *World Marit. Univ. Diss.*, vol. 618, 2018.
- [19] C. Song, "Global challenges and strategies for control, conversion and utilization of CO₂ for sustainable development involving energy, catalysis, adsorption and chemical processing," *Catal. Today*, vol. 115, no. 1–4, pp. 2–32, 2006.
- [20] E. V. Kondratenko, G. Mul, J. Baltrusaitis, G. O. Larrazábal, and J. Pérez-Ramírez, "Status and perspectives of CO₂ conversion into fuels and chemicals by catalytic, photocatalytic and electrocatalytic processes," *Energy Environ. Sci.*, vol. 6, no. 11, pp. 3112–3135, 2013.
- [21] J. R. Scheffe and A. Steinfeld, "Oxygen exchange materials for solar thermochemical splitting of H₂O and CO₂: A review," *Mater. Today*, vol. 17, no. 7, pp. 341–348, 2014.
- [22] M. Ezbiri, M. Takacs, B. Stolz, J. Lungthok, A. Steinfeld, and R. Michalsky, "Design principles of perovskites for solar-driven thermochemical splitting of CO₂," *J. Mater. Chem. A*, vol. 5, no. 29, pp. 15105–15115, 2017.
- [23] B. Bulfin, J. Vieten, C. Agrafiotis, M. Roeb, and C. Sattler, "Applications and limitations of two step metal oxide thermochemical redox cycles; A review," *J. Mater. Chem. A*, vol. 5, no. 36, pp. 18951–18966, 2017.
- [24] S. Dey and C. N. R. Rao, "Splitting of CO₂ by Manganite Perovskites to Generate CO by Solar Isothermal Redox Cycling," *ACS Energy Lett.*, vol. 1, no. 1, pp. 237–243, 2016.
- [25] M. Ezbiri, V. Becattini, M. Hoes, R. Michalsky, and A. Steinfeld, "High Redox Capacity of Al-Doped La_{1-x}Sr_xMnO_{3-Δ} Perovskites for Splitting CO₂ and H₂O at Mn-Enriched Surfaces," *ChemSusChem*, vol. 10, no. 7, pp. 1517–1525, 2017.

- [26] S. Dey, B. S. Naidu, and C. N. R. Rao, "Ln_{0.5}A_{0.5}MnO₃ (Ln=Lanthanide, A= Ca, Sr) perovskites exhibiting remarkable performance in the thermochemical generation of CO and H₂ from CO₂ and H₂O," *Chem. - A Eur. J.*, vol. 21, no. 19, pp. 7077–7081, 2015.
- [27] J. R. Scheffe, D. Weibel, and A. Steinfeld, "Lanthanum-strontium-manganese perovskites as redox materials for solar thermochemical splitting of H₂O and CO₂," *Energy and Fuels*, vol. 27, no. 8, pp. 4250–4257, 2013.
- [28] A. H. McDaniel *et al.*, "Nonstoichiometric perovskite oxides for solar thermochemical H₂ and CO production," *Energy Procedia*, vol. 49, pp. 2009–2018, 2013.
- [29] M. M. Nair and S. Abanades, "Insights into the Redox Performance of Non-stoichiometric Lanthanum Manganite Perovskites for Solar Thermochemical CO₂ Splitting," *ChemistrySelect*, vol. 1, no. 15, pp. 4449–4457, 2016.
- [30] A. Demont and S. Abanades, "High redox activity of Sr-substituted lanthanum manganite perovskites for two-step thermochemical dissociation of CO₂," *RSC Adv.*, vol. 4, pp. 54885–54891, 2014.
- [31] I. Yamada, "Novel catalytic properties of quadruple perovskites," *Sci. Technol. Adv. Mater.*, vol. 18, no. 1, pp. 541–548, 2017.
- [32] L. J. Venstrom, R. M. De Smith, Y. Hao, S. M. Haile, and J. H. Davidson, "Efficient splitting of CO₂ in an isothermal redox cycle based on ceria," *Energy and Fuels*, vol. 28, no. 4, pp. 2732–2742, 2014.
- [33] C. L. Muhich *et al.*, "Efficient Generation of H₂ by Splitting Water with an Isothermal Redox Cycle," *Science (80-.)*, vol. 341, no. 6145, pp. 540–542, Aug. 2013.
- [34] S. Dey, B. S. Naidu, A. Govindaraj, and C. N. R. Rao, "Noteworthy performance of La_{1-x}Ca_xMnO₃ perovskites in generating H₂ and CO by the thermochemical splitting of H₂O and CO₂," *Phys. Chem. Chem. Phys.*, vol. 17, no. 1, pp. 122–125, 2015.
- [35] C. Marinescu, L. Vradman, S. Tanasescu, and A. Navrotsky, "Thermochemistry of perovskites in the lanthanum-strontium-manganese-iron oxide system," *J. Solid State Chem.*, vol. 230, pp. 411–417, 2015.
- [36] K. T. C. Roseno, R. Brackmann, M. A. da Silva, and M. Schmal, "Investigation of LaCoO₃, LaFeO₃ and LaCo_{0.5}Fe_{0.5}O₃ perovskites as catalyst precursors for syngas production by partial oxidation of methane," *Int. J. Hydrogen Energy*, vol. 41, no. 40, pp. 18178–18192, 2016.
- [37] N. H. Batis, P. Delichere, and H. Batis, "Physicochemical and catalytic properties in methane combustion of La_{1-x}Ca_xMnO_{3±y} (0 ≤ x ≤ 1; -0.04 ≤ y ≤ 0.24)

- perovskite-type oxide,” *Appl. Catal. A Gen.*, vol. 282, no. 1–2, pp. 173–180, 2005.
- [38] S. Canright, “Measuring the Distance,” 2009. [Online]. Available: https://www.nasa.gov/audience/foreducators/k-4/features/F_Measuring_the_Distance_Student_Pages.html. [Accessed: 13-Apr-2019].
- [39] “The Sun and Us.” [Online]. Available: <https://history.nasa.gov/EP-177/ch3-1.html>. [Accessed: 13-Apr-2019].
- [40] B. Dunbar, “The Sun,” 2017. [Online]. Available: <https://www.nasa.gov/sun>. [Accessed: 13-Apr-2019].
- [41] “Plate Tectonics.” [Online]. Available: <https://www.nationalgeographic.com/science/earth/the-dynamic-earth/plate-tectonics/>. [Accessed: 13-Apr-2019].
- [42] R. S. Williams, Jr. and J. G. Ferrigno, Eds., “State of the Earth’s Cryosphere at the Beginning of the 21st Century: Glaciers, Global Snow Cover, Floating Ice, and Permafrost and Periglacial Environments,” in *U.S. Geological Survey Professional Paper 1386, Satellite Image Atlas of Glaciers of the World*, 2012, p. 546.
- [43] “Industrial Revolution,” *Encyclopaedia Britannica*. 2018.
- [44] C. S. Brown, “The Industrial Revolution.” [Online]. Available: <https://www.khanacademy.org/partner-content/big-history-project/acceleration/bhp-acceleration/a/the-industrial-revolution>. [Accessed: 11-Apr-2019].
- [45] IDMC and NRC, “Global Estimates 2015: People displaced by disasters,” 2015.
- [46] IEA, “Electricity Information 2018,” 2018. [Online]. Available: <https://www.iea.org/statistics/?country=WORLD&year=2016&category=Electricity&indicator=ElecGenByFuel&mode=chart&dataTable=ELECTRICITYANDHEAT>. [Accessed: 18-Apr-2019].
- [47] M. Aresta and A. Dibenedetto, “Utilisation of CO₂ as a chemical feedstock: Opportunities and challenges,” *J. Chem. Soc. Dalton Trans.*, no. 28, pp. 2975–2992, 2007.
- [48] R. B. Alley, S. Blumsack, and D. Bice, “Global Energy Consumption.” [Online]. Available: <https://www.e-education.psu.edu/earth104/node/1347>. [Accessed: 11-Apr-2019].
- [49] G. Zhao, X. Huang, X. Wang, and X. Wang, “Progress in catalyst exploration for heterogeneous CO₂ reduction and utilization: A critical review,” *J. Mater. Chem. A*, vol. 5, no. 41, pp. 21625–21649, 2017.

- [50] E. E. Barton, D. M. Rampulla, and A. B. Bocarsly, "Selective Solar-Driven Reduction of CO₂ to Methanol Using a Catalyzed," *J. Am. Chem. Soc.*, vol. 130, pp. 6342–6344, 2008.
- [51] O. Ishitani, C. Inoue, Y. Suzuki, and T. Ibusuki, "Photocatalytic reduction of carbon dioxide to methane and acetic acid by an aqueous suspension of metal-deposited TiO₂," *J. Photochem. Photobiol. A Chem.*, vol. 72, no. 3, pp. 269–271, 1993.
- [52] A. Navrotsky and D. J. Weidner, Eds., *Perovskite: A Structure of Great Interest to Geophysics and Materials Science*. Washington, D. C.: American Geophysical Union, 1989.
- [53] G. L. Lucena *et al.*, "New methodology for a faster synthesis of SrSnO₃ by the modified Pechini method," *Cerâmica*, vol. 59, no. 350, pp. 249–253, 2013.
- [54] M. A. Peña and J. L. G. Fierro, "Chemical structures and performance of perovskite oxides," *Chem. Rev.*, vol. 101, no. 7, pp. 1981–2017, 2001.
- [55] M. Johnsson and P. Lemmens, "Crystallography and Chemistry of Perovskites," *Handb. Magn. Adv. Magn. Mater.*, pp. 1–11, 2007.
- [56] F. S. Galasso, *Structure, properties and preparation of perovskite-type compounds*. Oxford; New York: Pergamon Press, 1969.
- [57] J. P. Attfield, "A Simple Approach to Lattice Effects in Conducting Perovskite-Type Oxides," *Chem. Mater.*, vol. 10, no. 11, pp. 3239–3248, 1998.
- [58] W. Travis, E. N. K. Glover, H. Bronstein, D. O. Scanlon, and R. G. Palgrave, "On the application of the tolerance factor to inorganic and hybrid halide perovskites: A revised system," *Chem. Sci.*, vol. 7, no. 7, pp. 4548–4556, 2016.
- [59] A. Navrotsky, "Thermochemistry of Perovskites," in *Perovskite: A Structure of Great Interest to Geophysics and Materials Science*, A. Navrotsky and D. J. Weidner, Eds. Washington, D. C.: American Geophysical Union, 1989, pp. 67–80.
- [60] L. M. Rodriguez-Martinez and J. P. Attfield, "Cation disorder and size effects in magnetoresistive manganese oxide perovskites," *Phys. Rev. B - Condens. Matter Mater. Phys.*, vol. 54, no. 22, pp. R15622–R15625, 1996.
- [61] L. M. Rodrmh, H. Ehrenberg, and J. P. Att, "Cation Size Variance Effects in High-Tolerance Factor Ln_{0.7}M_{0.3}MnO₃ Perovskites," vol. 25, pp. 20–25, 1999.
- [62] L. Liu, D. D. Taylor, E. E. Rodriguez, and M. R. Zachariah, "Influence of transition metal electronegativity on the oxygen storage capacity of perovskite oxides," *Chem. Commun.*, vol. 52, no. 68, pp. 10369–10372, 2016.
- [63] X. Wang, T. Wu, and M. R. Zachariah, "Doped Perovskites To Evaluate the

- Relationship between Fuel–Oxidizer Thermite Ignition and Bond Energy, Electronegativity, and Oxygen Vacancy,” *J. Phys. Chem. C*, vol. 121, no. 1, pp. 147–152, 2017.
- [64] R. J. H. Voorhoeve, J. P. Remeika, and L. E. Trimble, “Defect Chemistry and Catalysis in Oxidation and Reduction Over Perovskite-Type Oxides,” *Ann. N. Y. Acad. Sci.*, vol. 272, no. 1, pp. 3–21, 1976.
- [65] G. M. Dhar and V. Srinivasan, “Surface oxygen bond energy, and kinetics and catalysis on perovskite oxide catalysts,” *Int. J. Chem. Kinet.*, vol. 14, no. 4, pp. 435–438, 1982.
- [66] M. Futai, Y. Chen, and L. Hui, “CHARACTERIZATION OF PEROVSKITE-TYPE OXIDE CATALYSTS RECoO₃ BY TPR,” vol. 31, no. 1, pp. 47–53, 1986.
- [67] J. Miao, J. Sunarso, C. Su, W. Zhou, S. Wang, and Z. Shao, “SrCo_{1-x}Ti_xO_{3-δ} perovskites as excellent catalysts for fast degradation of water contaminants in neutral and alkaline solutions,” *Sci. Rep.*, vol. 7, no. February, pp. 1–10, 2017.
- [68] CavaLab - Solid State Chemistry Research Group, “Perovskite Structure and Derivatives,” *Princeton University*. [Online]. Available: <https://www.princeton.edu/~cavalab/tutorials/public/structures/perovskites.html>. [Accessed: 22-May-2019].
- [69] T. Ahmad, K. Ramanujachary, S. E. Lofland, and A. K. Ganguli, “Reverse micellar synthesis and properties of nanocrystalline GMR materials (LaMnO₃, La_{0.67}Sr_{0.33}MnO₃ and La_{0.67}Ca_{0.33}MnO₃): Ramifications of size considerations,” *J. Chem. Sci.*, vol. 118, no. 6, pp. 513–518, 2006.
- [70] A. A. Rabelo, M. C. de Macedo, D. M. de A. Melo, C. A. Paskocimas, A. E. Martinelli, and R. M. do Nascimento, “Synthesis and characterization of La_{1-x}Sr_xMnO_{3±δ} powders obtained by the polymeric precursor route,” *Mater. Res.*, vol. 14, no. 1, pp. 91–96, 2011.
- [71] M. E. Gálvez, R. Jacot, J. Scheffe, T. Cooper, G. Patzke, and A. Steinfeld, “Physico-chemical changes in Ca, Sr and Al-doped La-Mn-O perovskites upon thermochemical splitting of CO₂ via redox cycling,” *Phys. Chem. Chem. Phys.*, vol. 17, no. 9, pp. 6629–6634, 2015.
- [72] T. O. L. Sunde, T. Grande, and M. A. Einarsrud, “Modified pechini synthesis of oxide powders and thin films,” *Handb. Sol-Gel Sci. Technol. Process. Charact. Appl.*, vol. 0373, pp. 1089–1118, 2018.
- [73] L. Dimesso, “Pechini Processes: An Alternate Approach of the Sol–Gel Method, Preparation, Properties, and Applications,” in *Handbook of Sol-Gel Science and Technology*, Cham: Springer International Publishing, 2016, pp. 1–22.
- [74] Oils4life Limited, “Glass measuring beaker - 1000ml,” 2017. [Online]. Available:

<https://www.oils4life.co.uk/Glass-measuring-beaker-1000ml>. [Accessed: 20-Aug-2019].

- [75] H. Lee, M. Hong, S. Bae, H. Lee, E. Park, and K. Kim, "A novel approach to preparing nano-size Co_3O_4 -coated Ni powder by the Pechini method for MCFC cathodes," *J. Mater. Chem.*, vol. 13, no. 10, pp. 2626–2632, 2003.
- [76] Q. H. Wu, M. Liu, and W. Jaegermann, "X-ray photoelectron spectroscopy of $\text{La}_{0.5}\text{Sr}_{0.5}\text{MnO}_3$," *Mater. Lett.*, vol. 59, no. 12, pp. 1480–1483, 2005.
- [77] C. K. Yang, Y. Yamazaki, A. Aydin, and S. M. Haile, "Thermodynamic and kinetic assessments of strontium-doped lanthanum manganite perovskites for two-step thermochemical water splitting," *J. Mater. Chem. A*, vol. 2, no. 33, pp. 13612–13623, 2014.
- [78] T. S. Area, M. S. Characterization, and I. T. Issue, "Micromeritics' New 3Flex - Versatile High- Throughput Surface Area, Mesopore, and Micropore Surface Characterization," vol. 23, no. 1.
- [79] C. Thincert, "Application note," *Microprocess. Microsyst.*, vol. 16, no. 8, pp. 446–446, 1992.
- [80] K. Sing, "The use of nitrogen adsorption for the characterisation of porous materials," *Colloids Surfaces A Physicochem. Eng. Asp.*, vol. 187–188, pp. 3–9, 2001.
- [81] A. V. Neimark *et al.*, "Physisorption of gases, with special reference to the evaluation of surface area and pore size distribution (IUPAC Technical Report)," *Pure Appl. Chem.*, vol. 87, no. 9–10, 2015.
- [82] M. Muttakin, S. Mitra, K. Thu, K. Ito, and B. B. Saha, "Theoretical framework to evaluate minimum desorption temperature for IUPAC classified adsorption isotherms," *Int. J. Heat Mass Transf.*, vol. 122, pp. 795–805, 2018.
- [83] K. S. W. Sing and R. T. Williams, "Physisorption Hysteresis Loops and the Characterization of Nanoporous Materials," *Adsorpt. Sci. Technol.*, vol. 22, no. 10, pp. 773–782, 2005.
- [84] M. Kalwei, M. L. Occelli, J. P. Olivier, H. Eckert, and A. Auroux, "Basicity and Porosity of a Calcined Hydrotalcite-Type Material from Nitrogen Porosimetry and Adsorption Microcalorimetry Methods," *Chem. Mater.*, vol. 15, no. 22, pp. 4231–4238, 2003.
- [85] Micromeritics Instrument Corporation, "Gas Adsorption Theory," *Micromeritics Instrum. Corp.*, p. 1, 2000.
- [86] B. Cantero-tubilla, K. Sabolsky, E. M. Sabolsky, and J. W. Zondlo, "Investigation of Pretreated Switchgrass , Corn Stover , and Hardwood Fuels in Direct Carbon

Fuel Cells,” vol. 11, pp. 303–321, 2016.

- [87] C. Portet, G. Yushin, R. Mokaya, Y. Korenblit, Y. Gogotsi, and Z. Yang, “Electrical Double-Layer Capacitance of Zeolite-Templated Carbon in Organic Electrolyte,” *J. Electrochem. Soc.*, vol. 156, no. 1, p. A1, 2008.
- [88] A. Khawam and D. R. Flanagan, “Solid-state kinetic models: Basics and mathematical fundamentals,” *J. Phys. Chem. B*, vol. 110, no. 35, pp. 17315–17328, 2006.
- [89] F. J. Gotor, José, M. Criado, J. Malek, and N. Koga, “Kinetic analysis of solid-state reactions: The universality of master plots for analyzing isothermal and nonisothermal experiments,” *J. Phys. Chem. A*, vol. 104, no. 46, pp. 10777–10782, 2000.
- [90] M. Kubicek, A. H. Bork, and J. L. M. Rupp, “Perovskite oxides—a review on a versatile material class for solar-to-fuel conversion processes,” *J. Mater. Chem. A*, vol. 5, no. 24, pp. 11983–12000, 2017.
- [91] A. Demont, S. Abanades, and E. Beche, “Investigation of perovskite structures as oxygen-exchange redox materials for hydrogen production from thermochemical two-step water-splitting cycles,” *J. Phys. Chem. C*, vol. 118, no. 24, pp. 12682–12692, 2014.
- [92] H. Özdemir, M. A. Faruk Öksüzömer, and M. Ali Gürkaynak, “Preparation and characterization of Ni based catalysts for the catalytic partial oxidation of methane: Effect of support basicity on H₂/CO ratio and carbon deposition,” *Int. J. Hydrogen Energy*, vol. 35, no. 22, pp. 12147–12160, 2010.
- [93] J. M. Campos-Martin *et al.*, “Microwave-Assisted Coprecipitation Synthesis of LaCoO₃ Nanoparticles and Their Catalytic Activity for Syngas Production by Partial Oxidation of Methane,” *Front. Energy Res.*, vol. 6, no. April, pp. 1–11, 2018.
- [94] M. Rydén, A. Lyngfelt, T. Mattisson, D. Chen, A. Holmen, and E. Bjørgum, “Novel oxygen-carrier materials for chemical-looping combustion and chemical-looping reforming; La_xSr_{1-x}Fe_yCo_{1-y}O_{3-δ} perovskites and mixed-metal oxides of NiO, Fe₂O₃ and Mn₃O₄,” *Int. J. Greenh. Gas Control*, vol. 2, no. 1, pp. 21–36, 2008.
- [95] A. Wolfbeisser *et al.*, “Surface modification processes during methane decomposition on Cu-promoted Ni-ZrO₂ catalysts,” *Catal. Sci. Technol.*, vol. 5, no. 2, pp. 967–978, 2015.
- [96] C. Guo, J. Zhang, and X. Zhang, “Comparative study of LaNiO₃ and La₂NiO₄ catalysts for partial oxidation of methane,” *React. Kinet. Catal. Lett.*, vol. 95, no. 1, pp. 89–97, Oct. 2008.

- [97] S. Cimino, L. Lisi, S. De Rossi, M. Faticanti, and P. Porta, "Methane combustion and CO oxidation on LaAl_{1-x}Mn_xO₃ perovskite-type oxide solid solutions," *Appl. Catal. B Environ.*, vol. 43, no. 4, pp. 397–406, 2003.
- [98] T. Horiuchi, K. Sakuma, T. Fukui, Y. Kubo, T. Osaki, and T. Mori, "Suppression of carbon deposition in the CO₂-reforming of CH₄ by adding basic metal oxides to a Ni/Al₂O₃ catalyst," *Appl. Catal. A Gen.*, vol. 144, no. 1–2, pp. 111–120, 1996.
- [99] P. Granger, V. I. Parvulescu, S. Kaliaguine, and W. Prellier, Eds., "Steam Reforming of Alcohols from Biomass Conversion for H₂ Production," in *Perovskites and Related Mixed Oxides, Volume 1*, John Wiley & Sons, 2016, pp. 539–558.
- [100] C. Papadopoulou, H. Matralis, and X. Verykios, "Utilization of Biogas as a Renewable Carbon Source: Dry Reforming of Methane," in *Catalysis for Alternative Energy Generation*, L. Guczi and A. Erd helyi, Eds. New York, NY: Springer New York, 2012, pp. 57–128.
- [101] C. N. R. Rao *et al.*, "Influence of Cation Size on the Structural Features of Ln^{1/2}A^{1/2}MnO₃ Perovskites at Room Temperature," *Chem. Mater.*, vol. 10, no. 11, pp. 3652–3665, 2002.
- [102] J. B. Lansman, "Blockade of current through single calcium channels by trivalent lanthanide cations. Effect of ionic radius on the rates of ion entry and exit," *J. Gen. Physiol.*, vol. 95, no. 4, pp. 679–696, 2004.
- [103] M. Blaber, "Basic Concepts of Chemical Bonding - Bond Polarity and Electronegativity," 1996. [Online]. Available: <https://www.mikeblaber.org/oldwine/chm1045/notes/Bonding/Polarity/Bond05.htm>. [Accessed: 28-Mar-2019].
- [104] C. Lee, C. Sosa, M. Planas, and J. J. Novoa, "A theoretical study of the ionic dissociation of HF, HCl, and H₂S in water clusters," *J. Chem. Phys.*, vol. 104, no. 18, pp. 7081–7085, 2002.
- [105] P. Tyagi, "Thermochemistry," in *Thermochemistry*, New Delhi, India: Discovery Publishing House, 2006, pp. 1–61.
- [106] T. Lister and J. Renshaw, "Born-Haber cycles," in *Essential A2 Chemistry for OCR*, Cheltenham, United Kingdom: Nelson Thornes Ltd, 2004, pp. 71–73.
- [107] P. Fleming, "Lattice Energy and the Born-Haber Cycle," 2018. [Online]. Available: [https://chem.libretexts.org/Bookshelves/Physical_and_Theoretical_Chemistry_Textbook_Maps/Book%3A_Physical_Chemistry_\(Fleming\)/3%3A_First_Law_of_Thermodynamics/3.6%3A_Lattice_Energy_and_the_Born-Haber_Cycle](https://chem.libretexts.org/Bookshelves/Physical_and_Theoretical_Chemistry_Textbook_Maps/Book%3A_Physical_Chemistry_(Fleming)/3%3A_First_Law_of_Thermodynamics/3.6%3A_Lattice_Energy_and_the_Born-Haber_Cycle). [Accessed: 30-Mar-2019].

- [108] R. A. Robie, B. S. Hemingway, and J. R. Fisher, "Thermodynamic Properties of Minerals and Related Substances at 298.15K and 1 Bar Pressure and at Higher Temperatures," *U.S. Geol. Surv. Bull.*, vol. 1452, pp. 1–464, 1978.
- [109] J. M. Cerrato, M. F. Hochella, W. R. Knocke, A. M. Dietrich, and T. F. Cromer, "Use of XPS to Identify the Oxidation State of Mn in Solid Surfaces of Filtration Media Oxide Samples from Drinking Water Treatment Plants," *Environ. Sci. Technol.*, vol. 44, no. 15, pp. 5881–5886, Aug. 2010.
- [110] C. A. Johnson and K. M. Thomas, "Applications of Raman microprobe spectroscopy to the characterization of carbon deposits on catalysts," *Fuel*, vol. 63, no. 8, pp. 1073–1080, Aug. 1984.

APPENDICES

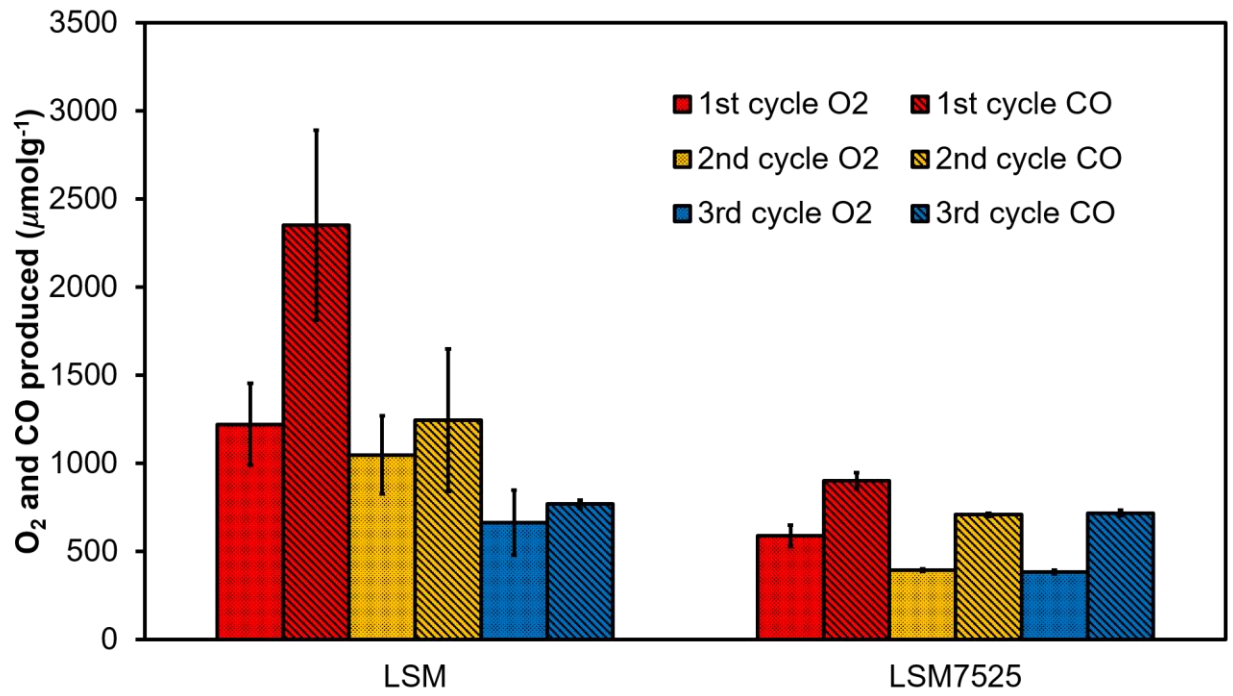


Figure 92. O₂ and CO production for LSM and LSM7525 during three redox cycles at 900 °C.